Dynamics of Bose-Einstein Condensates in Optical Lattices

KAREN ANNA CLARA BRAUN-MUNZINGER

A thesis submitted in partial fulfillment of
the requirements for the degree of
Doctor of Philosophy at the University of Oxford

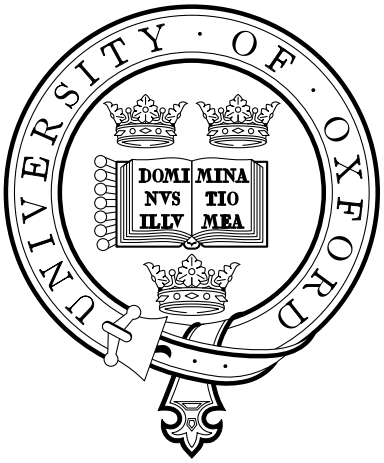

Merton College
University of Oxford
Michaelmas Term 2004

Dynamics of Bose-Einstein Condensates in Optical Lattices

Karen Anna Clara Braun-Munzinger, Merton College.

Thesis submitted for the degree of Doctor of Philosophy
at the University of Oxford, Michaelmas Term 2004.

Abstract

This thesis is concerned with the dynamics of Bose-Einstein condensates in optical lattices in the presence of an externally imposed force. We are especially interested in the response of the system as a probe of the Mott insulator - superfluid phase transition and use numerical simulations to study it.

To this end, we first discuss possible indicators of the Mott insulator and the superfluid phases. We then employ the Bose-Hubbard model in an exact numerical study of the equations of motion of bosons contained in a one-dimensional lattice.

We use these methods to study the effect of a static force across the lattice on the particles and the consequences of this dynamical evolution of the system on a number of observables.

We contrast these results from a static perturbation with the results of a time dependent excitation of the system. We also discuss possibilities for experimental indications of the phase (i.e. Mott insulator or superfluid) of the system based on our numerical results for static and time dependent excitations.

In the last part of the thesis, we study the quasi-periodical nature of the dynamical behaviour of the system under a static force. In addition to the well known Bloch oscillations, we find related, but distinct, oscillatory structures that are dependent on which phase the system is in. We discuss possible causes of these effects and present an analysis of our numerical results with a view to their experimental relevance.

Throughout this thesis, our aim has been to examine a wide range of system conditions. This has turned up novel dynamical features and suggests some future experimental possibilities.

Acknowledgements

Firstly, I would like to thank Professor Keith Burnett for his supervision, interesting discussions and emotional support. He has been an inspiration both as a scientist and as a person and I am very grateful for the privilege of having been able to spend a few years in his group.

Working with Dr Jacob Dunningham has been an absolute pleasure and I have learnt a great deal from him. Many thanks for being so patient, helpful and just all-around nice!

I have been lucky enough to meet a score of interesting people in the Clarendon laboratory: thanks to Rachel, Eleanor, Donna, Vincent, Simon C., Angharad, Zhao-Ma, Josh, Tom, David, Martin, Thorsten, Krzysztof, Thomas, Robert R., Matt, Simon G., Sam, Vicki, Mark, Robert S., Peter, Alex and Jacob for sharing tea, coffee and conversations! Heartfelt thanks also go to Robert Schumann, Dr Mark Lee and Dr Peter Kasprowicz for admirable patience in dealing with my computer emergencies and to Dr. Simon Gardiner for some highly appreciated advice.

My time in Oxford would not have been the same without my friends here and I am immensely thankful to all of you for sharing some of your life with me. I would especially like to thank Jan and Phil for being wonderful housemates and making my last year in Oxford so enjoyable. It is also a great pleasure to thank Mario and Kelley for succour and shelter in a time of great need (also known as the final thesis writing stage.) It made such a difference!

I owe a large debt of gratitude to the Rhodes trust for generously supporting me throughout my doctorate in the form of a Rhodes Scholarship. It has been a great privilege to spend this time in Oxford and I much appreciate it. I would also like to mention the Studienstiftung des deutschen Volkes and Merton College and thank them for various forms of support. Thanks also go to the Clarendon

Laboratory for the use of their facilities.

Finally, I would like to thank my family for being so supportive and understanding. I could not have done this without you.

Contents

Chapter 1

Introduction

In this introductory chapter, we shall first give a brief overview of the historical development of the theory of Bose-Einstein condensation. We then describe the route to experimental realization and briefly touch upon the many exciting aspects that can be studied with the help of Bose-Einstein condensates (BEC). Lastly, we will give an overview of the specific work presented in this thesis.

1.1 Brief introduction to BEC

1.1.1 General theory

The theory of BEC has a long history: it all began in the early days of quantum mechanics with the discovery that identical quantum mechanical particles do not, in contrast to their classical counterparts, have well-defined trajectories in phase space and are thus not individually distinguishable. Indeed, should we define a many-body wave function where mathematical labels are assigned to each particle, an exchange of these labels could lead to different physical outcomes.

In order to obtain unambiguous physical observables, certain symmetries regarding the exchange of particles had to be imposed on the many-body wave function. It turns out that there are two possible symmetries - the many-body wave function Ψ must be either symmetric or antisymmetric under the exchange of particle labels. In mathematical terms, this is equivalent to

$$\Psi(\ldots, x_i, \ldots, x_j, \ldots) = \pm\Psi(\ldots, x_j, \ldots, x_i, \ldots). \tag{1.1}$$

Symmetric exchange, i.e. invariance under particle label exchange, trivially fulfills the condition of indistinguishability. The possibility of antisymmetric exchange, however, is a direct consequence of the quantum mechanical definition of observables. All experimentally accessible variables $\mathcal{A}$ of the system can be written such that

$$\mathcal{A} = \langle \Psi | \mathcal{O} | \Psi \rangle \tag{1.2}$$

for some operator $\mathcal{O}$. Consequently, antisymmetric exchange does not change any experimentally observable variables of the system and is permissible.

Particles with symmetric wave functions are said to obey Bose-Einstein statistics and are called bosons while such with an antisymmetric wave function obey Fermi-Dirac statistics and are termed fermions.

The property of symmetry or anti-symmetry is also related to the intrinsic angular momentum of the particles by the spin statistics theorem [1]. According to this, bosons have integer spin while fermions possess half-integer spin. Strictly speaking, the spin statistics theorem applies only to elementary particles. Composites of fermions (such as atoms) with a total integer spin, however, will behave as bosons when energies are sufficiently low that their internal structures cannot be resolved. For the atoms discussed in this thesis, such low energies will always be assumed.

One consequence of the symmetry property is the marked difference between the ground state occupation of fermions and bosons. While fermions are governed by the Pauli exclusion principle that forbids sharing of the same quantum state, there is no limit on the number of bosons that can occupy a quantum state. Consequently, in equilibrium bosonic systems, the energetically lowest states tend to be multiply occupied.

This behaviour of bosons is central to the thermodynamic phase that is known as a Bose-Einstein condensate (BEC). Under the right conditions (most importantly of density and temperature), the tendency towards multiple occupation of states can lead to the macroscopic occupation of one single quantum state (most commonly the ground state) [2]. The atoms in this quantum state are then collectively called a Bose-Einstein condensate and, by definition, share all quantum properties.

For an ideal (i.e. non-interacting) gas, the calculation of the interesting thermodynamical properties is very well understood and can be found in most statistical mechanics textbooks [3]. One important result is the relation of the particle density n to the de Broglie wave length $\lambda_{dB} = \sqrt{2\pi/mk_BT}$ (m is the particle mass, k_B the Boltzmann constant and T the temperature). For a three-dimensional system, we

find that Bose-Einstein condensation, i.e. the phase transition to a BEC, occurs for $n\lambda_{dB}^3 \geq 2.612$. In other words, condensation becomes possible when the de Broglie wavelength is comparable to the particle separation or, equivalently, when there is a significant overlap of the particle de Broglie wavelengths.

In general, the introduction of interaction changes the behaviour of the many-body system. By 1947, it was shown [4] that weak interactions do not profoundly affect the nature of the BEC itself. They do, however, change observables such as the low-lying excitations and whether or not the system is a superfluid. Building on these fundamental results, BEC theory has evolved to such an extent over the following decades that a comprehensive review would at least treble the length of this thesis. More to this development can be found in the overview articles [5, 6, 7, 8], books [9, 10, 11, 12] and references therein.

1.1.2 Experimental review

Despite its early theoretical beginnings, experimental realization of a BEC was only achieved quite recently in 1995 [13]. In fact, for a long time theorists felt that the high densities and low temperatures required to fulfill the condition $n\lambda_{dB}^3 \geq 2.612$ would never be within experimental reach. Part of the problem was the need for relatively weak interactions - even when sufficient densities and temperatures were achieved in liquid helium, strong interactions meant that the resulting state was not a pure BEC [14, 15]. These experimental limitations changed drastically with the invention of the laser - and with the realization of one of its applications, the experimental technique of laser cooling. From the 1980s on, techniques for cooling and trapping of (mostly alkali) atoms grew more and more refined until success in condensing ^{87}Rb was reported by the group of Cornell and Wieman at JILA in Boulder, Colorado [13] in 1995. Their success was rapidly followed by that of several other groups who reported the observation of BEC in ^{23}Na [16], ^{7}Li [17] and in atomic hydrogen [18].

Despite the variation in the condensed elements, the broad outline of all of these experiments is rather similar. (For more detailed reviews see e.g. [19, 20]). In order for cooling to be possible, atoms need to be thermally isolated from all material walls - consequently, all trapping is done with electromagnetic fields. To avoid contamination with other chemical elements as much as possible, this trapping takes place in ultrahigh vacuum chambers. Atoms are first pre-cooled with lasers, gaining about six orders of magnitude in phase space density, and then evaporatively

cooled to condensation with another phase space density gain of about six orders of magnitude.

Laser pre-cooling is usually carried out by superimposing pairs of counter-propagating laser beams. These laser beams are slightly red-detuned below the atomic resonance with opposite circular polarisation. The detuning is chosen such that the laser opposing the atom's motion is shifted towards the resonance in the reference frame of the particle by the Doppler shift. Atoms are thus more likely to absorb a photon from the opposing laser and will, on average, be slowed down.

This technique is known as "optical molasses" and is highly effective up to the Doppler-cooling limit (usually at a velocity of a few ms^{-1}, but dependent on the type of atoms being cooled). The Doppler-cooling limit is a result of the diffusive heating that laser beams cause by the absorption and random re-emission of photons. The efficiency of cooling using optical molasses is thus determined by the strength of cooling in comparison with diffusive heating. At the point of equilibrium, optical molasses have reached the limit of their usefulness.

Optical molasses can be used in a variety of configurations, most commonly in the magneto-optical trap (MOT). Some form of confinement of the atomic cloud is usually necessary to allow the slowing force of the optical molasses to cool the atoms without them escaping immediately. The MOT has the added advantage of Zeeman shifting the atomic energy levels. The detuning of the atomic energy level to the laser beam can then be made position dependent so that the radiative force acting on the atoms is weak in the centre of the trap, but grows increasingly strong away from the centre. The cloud is then not only cooled, but also focussed into the centre.

After laser pre-cooling, atoms are typically cooled to temperatures of the order of μK, but the phase space density can still be up to six orders of magnitude smaller than that required for condensation. The next step is then evaporative cooling. This method is often compared to blowing the steam off a coffee cup and consists of removing the high-energy end of the thermal distribution from the trap. With the loss of these atoms, more than the average thermal energy per atom is lost from the trap so that, after rethermalization, the temperature in the remaining gas will be lower. In order for evaporative cooling to be efficient, the loss rate from the trap needs to be significantly slower than the rethermalization rate. Under ideal conditions, the gain in phase space density is then about six orders of magnitude at a cost of a factor of 1000 reduction in the total number of atoms.

As with the laser pre-cooling, evaporative cooling has its limitations. In addi-

tion to the 'good' elastic collisions which enable rethermalization, one finds 'bad' inelastic collisions that cause trap loss and heating. Thus, if the truncation of the thermal energy by the evaporative cooling is chosen too large, the increase in phase space density will be more than cancelled out by the decrease due to (inelastic) losses. Serendipitously, the ratio of elastic to inelastic collisions was found to be favourable for the alkali atoms chosen in the JILA and MIT experiments so that BEC could be reached with evaporative cooling. BEC in gases with less favourable collision ratios such as Cs took significantly longer to obtain [21] - despite much experimental effort, the first experimental observation was only in 2003.

1.1.3 Optical lattices

Once the techniques necessary to reach Bose-Einstein condensation were well established, more and more applications of BECs beyond the simple establishment of the condensed phase were proposed and (in some cases) carried out. After all, a BEC can be compared to a magnified view of the quantum world - the quantum properties of one atom are now shared by millions of others. Consequently, BECs are a wonderful playground for testing out fundamental theories of quantum mechanics.

Some examples from the last few years include the creation of vortices [22], the use of condensates in an atom interferometer [23] and the construction of atom lasers [24, 25, 26].

In this thesis, we shall explore the rich physics of Bose-Einstein condensates in optical lattices. Optical lattices are formed by counterpropagating laser beams that form standing waves. Atoms are then trapped at the nodes or anti-nodes of the standing wave, depending on the polarization of the laser beams, by the dipole force. We shall discuss the theoretical background to the interaction of bosons with an electromagnetic field in some more detail in Chapter 2 and now proceed to give an overview of experimental progress.

The technique used for optical lattices is very similar to optical molasses - they were developed together with the technology needed for Bose-Einstein condensation in the late 1980s and early 1990s to trap cold atoms [27, 28, 29, 30]. The initial experiments [27] focussed on exploring the diffraction of atoms by standing light waves rather than on trapping and containing them. With increasing experimental sophistication, the focus shifted to the study of atoms trapped in an optical lattice with a view to obtaining information about the dynamics of the laser-cooled atoms

through the dependence of their energy spectrum on the parameters of the optical lattice. Over the following years, techniques for detecting atom dynamics in optical lattices grew increasingly more refined [31] leading to the development of atom-optical elements [32] as well as to studies of quantum chaos [33].

At the same time, interest in the study of Josephson-effect interference was growing, fuelled by the possibility of carrying out interference experiments with coupled superfluid He(3) reservoirs [34]. The possibility of observing such phase-dependent dynamics with BECs in optical lattices attracted much theoretical interest [35, 36] and was finally verified in the Kasevich group at Yale in 1998 [37].

The exact trapping configuration for BECs in optical lattices varies from experiment to experiment, but the general strategy is as follows. A dilute vapour is first cooled to condensation as described above. With the condensate held in a magnetic trap, the optical lattice is then created by gradually ramping up the intensity of a standing wave of light. For two- and three-dimensional optical lattices, the necessary number of beams is usually created by splitting and reflection of one initial beam. For a three-dimensional lattice, the interfering standing waves then form a crystal-like structure with regular local potential minima in which atoms can be trapped. In a two-dimensional lattice, the effect of the laser waves is to divide the initial condensate into regular tube-like quasi one-dimensional condensates. A one-dimensional lattice could be used to divide the condensate into sheet-like two-dimensional condensates. In these configurations, it is thus possible not only to explore the interaction of atoms trapped in various potential minima, but also to create and study lower-dimensional condensates.

Once the possibility of BECs in optical lattices was established, a wide range of experiments followed (for a recent review see [38]).

In this thesis, we shall focus on one particular aspect of physics in optical lattices: the Mott insulator (MI) - superfluid (SF) transition, its signatures and excitational structure. In 1998, Jaksch and coworkers showed that BECs in optical lattices can be described by the Bose-Hubbard model (BHM) where the system parameters are controlled by laser light [39]. The BHM predicts a second order quantum phase transition from a Mott insulator to a superfluid phase. The central parameter of this phase transition is the dimensionless ratio g of the zero-range onsite interaction constant U (caused by repulsion) to the tunneling matrix element J. For $g = U/J << 1$, atoms are delocalized across the lattice, their kinetic energy is much larger than the potential energy deriving from interactions and they are in the superfluid phase. For $g = U/J >> 1$, in contrast, atoms are so strongly

localized that the occupation number of atoms per site is pinned at an integer value and the interaction energy is much higher than its kinetic energy. We shall discuss the definitions of both superfluidity and the Mott insulator phase in more detail in Chapter 3.

This phase transition was realized experimentally three years after the theoretical prediction in a seminal experiment by the group of Immanuel Bloch and Ted Hänsch in Munich [40]. This was followed by an explosion of theoretical and experimental interest in the specifics of the phase transition, applications of the MI states, recreation in one dimension [41] and many other aspects.

1.2 Thesis outline

In this thesis, we are primarily interested in the exploration of the dynamics of BECs in optical lattices near to the MI - SF phase transition and in the strongly interacting Mott insulator regime. In order to lay the foundation for this work, we present the theoretical framework for the Bose-Hubbard model in the second chapter. We begin with a closer look at the atom-field interaction present in an optical lattice for single particles. We then present the derivation of the BHM following the method used in [39] and discuss the possible basis states and assumptions made in that model.

In the third chapter, we look at the MI - SF phase transition in more detail. Firstly, we consider the characteristics of quantum phase transitions in general. We then review the specific points of the two phases. In the last part of this chapter we discuss possible experimental signatures of the MI - SF transition.

Chapters 4, 5 and 6 represent original research that I have carried out during the course of my doctorate.

Motivated by the beautiful experiment of Greiner *et al.* [40], the fourth chapter will be concerned with the effect of a static force on the dynamics of an optical lattice. We will present results of our numerical simulations. One of our main interests is the response of states with various degrees of reduced number fluctuations. Using an exact calculation, we find evidence for interesting excitational structures in addition to those already observed experimentally. We also study the relation between the number variance and the change in added energy as well as in the interference pattern and find that the number variance can be a very good indicator of excitations in the energy of the system.

In the fifth chapter, we study the response of bosons in a one-dimensional lattice

for a dynamic excitation as it was realized in, e.g., the group of Esslinger at the ETH [41]. We find that such excitations are indeed a very precise instrument for exploring the energy eigenvalues of the system and identify features that could possibly be of use in tracking the MI - SF phase transition.

The sixth chapter is a study of the rich oscillatory spectrum we have found for the excitation of a one-dimensional lattice by a static force. We identify the predicted Bloch oscillations and find and interpret additional oscillations that could be very useful in a study of the resonances of the system. We also find a dependence of oscillation strength on the phase of the system. As Bloch oscillations can be present even for a non-interacting, single-particle system, the relation of these oscillations to effects caused by the 'particle-like' nature of the MI phase may give interesting insights into the state of the system.

In the seventh chapter, we will give a summary of the work discussed in this thesis and discuss possibilities for future work. Details of the numerical procedures used for Chapters 4 to 6 will be set out in an appendix.

Note: we set $\hbar = 1$ throughout the thesis.

Chapter 2

Optical lattices and the Bose-Hubbard model

In this chapter, we shall explain the interaction of bosons with an electromagnetic field that is central to the trapping by optical lattices. We then discuss possibilities for basis states in an optical lattice. Finally, we derive the Bose-Hubbard model that will be central to all further work in this thesis.

2.1 Optical lattices

An optical lattice for BECs is produced by the interference of two or more laser beams. The atoms are then subject to the so-called dipole force. For an excellent introduction to this force see [42] and, slighty more specific to experimental procedures, [43]. For a two-level atom, the Hamiltonian for a standing plane wave (i.e. an interference of two laser beams) can be written as [11, 44, 45, 46, 47, 48]

$$\widehat{H} = \begin{pmatrix} E_e & 0 \\ 0 & E_g \end{pmatrix} + \frac{\hat{\mathbf{p}}^2}{2m} \begin{pmatrix} 1 & 0 \\ 0 & 1 \end{pmatrix} + 2\Omega \cos(\omega_L t) \cos(k_L x) \begin{pmatrix} 0 & 1 \\ 1 & 0 \end{pmatrix} \tag{2.1}$$

where m is the atomic mass, E_g and E_e the ground and excited electronic states of the atom and Ω the Rabi frequency between these states. ω_L and k_L are the frequency and wave vector of the standing wave. We then substitute the ansatz

$$\Psi(x,t) = \exp(-i\omega_L t)\psi_e(x,t)|e\rangle + \psi_g(x,t)|g\rangle \tag{2.2}$$

into the Schrödinger equation for the Hamiltonian (2.1). In the rotating wave approximation, one then obtains a system of coupled equations

$$i\frac{\partial\psi_e(x,t)}{\partial t} = -\delta\psi_e(x,t) + \frac{\hat{\mathbf{p}}^2}{2m}\psi_e(x,t) + \Omega\cos(k_L x)\psi_g(x,t) \tag{2.3}$$

$$i\frac{\partial\psi_g(x,t)}{\partial t} = \frac{\hat{\mathbf{p}}^2}{2m}\psi_g(x,t) + \Omega\cos(k_L x)\psi_e(x,t) \tag{2.4}$$

$$\tag{2.5}$$

where $\delta = \omega_L - (E_e - E_g)$ is called the detuning. We can gain decoupled equations by making a number of further assumptions [49]. For one, we assume that the detuning δ is much larger than the Rabi frequency Ω. We also assume that both detuning and Rabi frequency are much larger than the momentum contribution $\hat{\mathbf{p}}^2/2m$. For the purposes of this thesis, we can also make the assumption that the internal motion of the atom is instantly damped to equilibrium. As ψ_e carries the internal motion, this implies that $\partial\psi_e/\partial t = 0$.

We can then simplify the first excited state to

$$\psi_e(x,t) \approx \frac{\Omega}{\delta}\cos(k_L x)\psi_g(x,t). \tag{2.6}$$

For this simplification, the Schrödinger equation then has the more convenient form of

$$i\frac{\partial\psi_g(x,t)}{\partial t} = \left(\frac{\hat{\mathbf{p}}^2}{2m} + V_{\text{latt}}(x)\right)\psi_g(x,t) \tag{2.7}$$

where the optical lattice potential V_{latt} is equal to

$$V_{\text{latt}}(x) = V_0\cos^2(k_L x), \quad V_0 = \Omega^2/\delta. \tag{2.8}$$

2.2 Picturing a lattice - Bloch and Wannier functions

For a periodic lattice, the eigenstates of the single particle Hamiltonian derived above,

$$\widehat{H}_0 = \hat{\mathbf{p}}^2/2m + V_{\text{latt}}(x), \tag{2.9}$$

take the convenient form of Bloch states $\psi_{n\mathbf{q}}$. For this to hold, it is not even necessary for V_{latt} to take the form of Eq. (2.8). It only needs to be periodic so that for all $\mathbf{R} = n_1\mathbf{a}_1 + n_2\mathbf{a}_2 + n_3\mathbf{a}_3$ ($n_i \in \mathbb{Z}$, $\mathbf{a}_i$ are the lattice basis vectors), the

condition of $V_{\text{latt}}(\mathbf{r}) = V_{\text{latt}}(\mathbf{r}+\mathbf{R})\,\forall\,\mathbf{r} \in \mathbb{R}$ is fulfilled. Bloch states can be written in the form

$$\psi_{n\mathbf{q}}(\mathbf{r}) = u_{n\mathbf{q}}(\mathbf{r})e^{i\mathbf{q}\cdot\mathbf{r}} \tag{2.10}$$

where $u_{n\mathbf{q}}(\mathbf{r}) = u_{n\mathbf{q}}(\mathbf{r}+\mathbf{a}_i)$, i.e. they are periodic, $\mathbf{q}$ is the quasi-momentum and n the band index. It is clear from Eq. (2.10) that the Bloch states are delocalized and extend over the entire lattice. Conceptually, however, it can be easier to use localized states in order to study many-body interactions. We therefore introduce localized Wannier states $w_n(\mathbf{R}_i)$ for each site $\mathbf{R}_i$ which are defined as the Fourier transform of the Bloch eigenstates in the momentum representation. They can be found by summing over all Bloch states in one Brillouin zone:

$$w_n(\mathbf{r}-\mathbf{R}_i) \equiv \frac{1}{\sqrt{N}}\sum_{\mathbf{q}} e^{-i\mathbf{q}\cdot\mathbf{R}_i}\psi_{n\mathbf{q}}(\mathbf{r}). \tag{2.11}$$

In their most general form, Wannier states are Mathieu functions which are not trivial to solve (an introduction is given in [50]). For the purposes of the theory in this thesis, however, it has been shown [51, 52] that we can approximate these complex functions by the eigenstates of the harmonic oscillator, e.g. for the first band by the Gaussian function

$$\phi_{0+} = \frac{1}{\sqrt{\sqrt{\pi}\sigma}}\exp(-x^2/2\sigma^2) \tag{2.12}$$

where σ is dependent on the height of the potential barrier separating the sites in the optical lattice. A necessary condition for this is the single-band approximation, i.e. we assume that only the first Bloch band is populated. The approximation of using the harmonic oscillator eigenstate of Eq. (2.12) is then valid as long as $U > E_{\text{R}}/4$ where

$$E_{\text{R}} = k^2/2m \tag{2.13}$$

is the single photon recoil energy with $k = 2\pi/\lambda$ and m is the atomic mass. We will discuss these approximations and the exact form of the Wannier Gaussian function for the BHM further in Chapter 5.

2.3 The Bose-Hubbard Model

Wannier functions are also crucial to the calculation of the second quantized Hamiltonian that is central to the Bose-Hubbard model (BHM) [53, 54]. The starting

point for the derivation of the BHM Hamiltonian is usually [39, 55] the many-body field Hamiltonian in second quantization

$$\widehat{H} = \int \mathrm{d}\mathbf{r}\, \hat{\psi}^\dagger(\mathbf{r})\{\widehat{H}_0 + V_{\mathrm{ext}}(\mathbf{r})\}\hat{\psi}(\mathbf{r}) + \frac{1}{2}g \int \mathrm{d}\mathbf{r}\, \hat{\psi}^\dagger(\mathbf{r})\hat{\psi}^\dagger(\mathbf{r})\psi(\mathbf{r})\psi(\mathbf{r}) \tag{2.14}$$

A derivation of this can be found in most advanced quantum mechanics textbooks, see e.g. [56]. Here $\hat{\psi}^\dagger$ is the boson field operator, V_{ext} is an external potential in addition to V_{latt} and $g = 4\pi a_s/m$ is the interaction strength, with a_s the s-wave scattering length and m the atomic mass. $\widehat{H}_0 = \hat{\mathbf{p}}^2/2m + V_{\mathrm{latt}}(x)$ is motivated by the single-particle Hamiltonian of Eq. (2.9) derived above. We have made the assumption that both the de Broglie wavelength and the distance between lattice sites are very large compared to the range of interatomic forces. This allows us to represent the interatomic potential V_{int} in terms of the binary s-wave scattering length a_s as $V_{\mathrm{int}} = g\delta(\mathbf{r}-\mathbf{r}')$ [57]. We now expand the field operator into a Wannier basis w of the ground band

$$\hat{\psi} = \sum_i w_0(\mathbf{r} - \mathbf{R}_i)\hat{a}_i \tag{2.15}$$

and make the so-called *tight-binding approximation*, that is, we assume that the Wannier states only have significant overlap between nearest-neighbour sites. That means that we can use the scattering length description of the interaction as described by [58]. The restriction of the basis to the first band allows us to approximate the Wannier functions by the Gaussian function

$$\phi_{0+} = \frac{1}{\sqrt{\sqrt{\pi}\sigma}} \exp(-x^2/2\sigma^2) \tag{2.16}$$

of Eq. (2.12) as long as the condition $U > E_R/4$ is fulfilled [51, 52]. This condition holds for the given values of U in the relevant experiments [40, 59, 41] so that the restriction of our numerical model to $U > E_R/4$ should not limit its applicability.

Clearly, the restriction to the first band is an approximation that can (and does [60] at times) fail in experimental settings. These transitions between Bloch bands are known as Landau-Zener tunneling [61, 62]. The conditions under which Landau-Zener tunneling sets in are strongly system dependent. For the purposes of this thesis, we will focus on systems in which it does not play a significant role.

With these approximations, the Hamiltonian of Eq. (2.14) reduces to

$$\widehat{H}_{\mathrm{BHM}} \approx -J \sum_{\langle i,j \rangle} \hat{a}_i^\dagger \hat{a}_j + \sum_i \epsilon_i \hat{a}_i^\dagger \hat{a}_i + \frac{1}{2} U \sum_i \hat{a}_i^\dagger \hat{a}_i^\dagger \hat{a}_i \hat{a}_i. \tag{2.17}$$

$\langle i, j \rangle$ indicates summation over all nearest neighbours. The transitional matrix element J is defined for adjacent sites i and j as

$$J = \int \mathrm{d}\mathbf{r}\, w^*(\mathbf{r} - \mathbf{R}_i) \widehat{H}_0 w(\mathbf{r} - \mathbf{R}_j). \tag{2.18}$$

It can also be thought of as a measure of the 'hopping' of atoms between adjacent sites. The zero-range, on-site interaction strength U is defined as

$$U = 4\pi a_s \int \mathrm{d}\mathbf{r}\, |w(\mathbf{r} - \mathbf{R}_i)|^4. \tag{2.19}$$

The site-dependent local energy ϵ_i is equal to

$$\epsilon_i \equiv \int \mathrm{d}\mathbf{r}\, w_0^*(\mathbf{r} - \mathbf{R}_i) V_{\mathrm{ext}}(\mathbf{r}) w_0(\mathbf{r} - \mathbf{R}_i). \tag{2.20}$$

Chapter 3

Quantum phase transitions

In this chapter, we will briefly discuss the characteristics of phase transitions. We will then explain specific features of the MI - SF quantum phase transition. Lastly, we will use this to discuss experimental realisations of MI and SF phases and the possible indicators for tracking the point of transition.

3.1 What are quantum phase transitions?

Generally, a phase transition is the sharp change of a thermodynamic system from one phase to another. A phase in a system is a region in the parameter space of the system's thermodynamic variables in which the free energy is analytic. Equivalently, if two states of a system can be transformed into each other without abrupt changes in their thermodynamic properties, they are in the same phase. Consequently, a phase transition is characterized by a sudden change in some thermodynamic property (a typical example is a sudden change in heat capacity for a fluctuation in temperature at the solid-liquid phase transition). Classical phase transitions are usually driven by thermal fluctuations.

For a quantum phase transition, the sudden change in an observable is caused by a quantum mechanical fluctuation. Indeed, quantum systems can have fluctuations driven by, for example, the Heisenberg uncertainty principle, even at zero temperature where classical phases would be frozen to the ground state.

More formally [54], a quantum phase transition can be identified as any point for which the ground state energy becomes non-analytical. As this non-analyticity is usually the result of competition between two terms in the underlying Hamiltonian,

it can also be thought of as either an actual energy level crossing (possible in finite and infinite systems) or an avoided level crossing (only possible in the limit of an infinite system).

A system with an avoided level crossing thus only has a proper phase transition in its infinite limit. After all, when the system is finite, it does not have a point of non-analyticity. The thermodynamic phases, however, are usually still present. For finite systems, the transition between them will be gradual rather than instantaneous - we get a cross-over phase.

In this thesis we are interested in the MI - SF transition which is a so-called second order quantum phase transition. This implies that a characteristic energy scale of fluctuations above the ground state will vanish as the system approaches the non-analytical transition point.

3.2 The Mott Insulator - Superfluid phase transition

The phase transition from the Mott insulator to a superfluid is commonly [63] described by starting out from the atomic limit (where the tunneling matrix element J is very small), i.e. the MI phase. The ground state is then given by

$$|N_p, 0\rangle_{\text{Mott}} = \prod_{i=1}^{N_s} \frac{1}{\sqrt{N_p!}} (\hat{a}_i^\dagger)^{N_p} |000\ldots0\rangle \tag{3.1}$$

where N_p is the number of particles per site and N_s the number of sites. $|000\ldots0\rangle$ is the vacuum state and $|N_p, m\rangle$ is taken to mean the mth eigenstate so that $|N_p, 0\rangle$ is the ground state. We find that the MI phase is incompressible, i.e. there is an integer number of particles $N_p \,\epsilon\, \mathbb{N}$ per site. The MI - SF phase transition is then found by studying excitations of the energy ground state. In the incompressible MI phase, these excitations correspond to a finite non-zero energy, E_{G}, which is generally termed as showing an energy gap, i.e. E_{G}, or being gapped. At the MI - SF transition, $E_{\text{G}} \to 0$ which is known as the energy spectrum becoming gapless. For the MI phase, the excitations of the ground state are defined by the addition or removal of a particle with respect to a specific site i and can be written as

$$|N_p, 0; i\rangle_{\text{part}} = \frac{1}{\sqrt{N_p + 1}} \hat{a}_i^\dagger |N_p, 0\rangle_{\text{Mott}} \tag{3.2}$$

$$|N_p, 0; i\rangle_{\text{hole}} = \frac{1}{\sqrt{N_p}} \hat{a}_i |N_p, 0\rangle_{\text{Mott}}. \tag{3.3}$$

$|N_p, 0; i\rangle_{\text{part}}$ denotes the ground state with the addition of a particle at site i while $|N_p, 0; j\rangle_{\text{hole}}$ represents the ground state with the addition of a hole (i.e. removal of a particle) at site j.

For $J = 0$, their energy relative to the ground state of Eq. (3.1) is equal to

$$E_{\text{part}} = UN_p - \mu \tag{3.4}$$

$$E_{\text{hole}} = -U(N_p - 1) + \mu, \tag{3.5}$$

where U is the interaction strength as defined in Eq. (2.19) and μ is the chemical potential. Whether excitations are gapped or gapless is determined by the difference Δ between the energy gained by an added particle and lost by a hole, i.e.

$$\Delta(U, J) = |E_{\text{part}}| - |E_{\text{hole}}|. \tag{3.6}$$

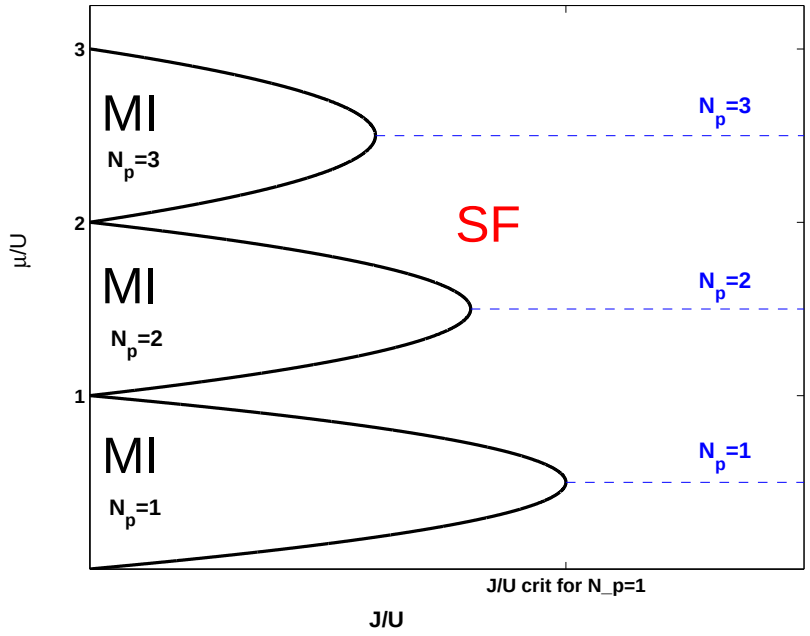

Figure 3.1: This plot illustrates the general features of the zero-temperature phase diagram for the MI - SF transition [53, 64] schematically. The dashed blue lines in the SF phase represent constant integer density $N_p = 1, 2, 3$. They touch the MI phases at the tips of the lobes at a critical value J/U which decreases with increasing density N_p.

For $J = 0$, we immediately see that $\Delta(U, J) = U$. With increasing J, $\Delta(U, J)$ decreases until, at the phase transition, the energy to remove a particle and the

energy to add a particle become degenerate so that $\Delta(U, J) = 0$ and the MI phase vanishes completely. This dependence of the transition point on energy fluctuations above the ground state shows that the MI - SF transition is a second order phase transition.

The precise location of the point for which $\Delta(U, J) = 0$, is not easy to determine and is strongly dependent on the dimensionality and total number of atoms of the system. For a one-dimensional lattice, Quantum Monte Carlo studies [65], renormalization group results [66], mean-field approximations [67, 68] and strong-coupling expansions [63] give $(U/J)_c = 3.8$ for $N_p = 1$ (N_p is the mean number of atoms per site) and $(U/J)_c = 2.2N_p$ for $N_p >> 1$. In the three-dimensional lattice [53, 69, 70, 71], the MI - SF transition occurs at $(U/J)_c = 5.8z$ (z is the number of nearest neighbours) for $N_p = 1$, and $(U/J)_c = 4N_pz$ for $N_p >> 1$. Fortunately for the applicability of results, the qualitative features of the phase transition are not dependent on the dimension even though the quantitative values such as the point of transition vary. Fig. 3.1 shows the qualitative structure of the zero-temperature phase diagram schematically. We have already seen that the MI phase is characterized by an energy gap. It is important to realize that this also implies non-compressibility. For $J << U$, one thus obtains a series of 'Mott-lobes' with fixed integer filling $N_p = 1, 2, \ldots$ The integer filling N_p depends on the chemical potential μ. One consequence of this non-compressibility is that for a state with non-integer filling, i.e. for $N_p = m + \epsilon$ where $m \in \mathbb{N}$ and $0 < \epsilon < 1$, the system cannot be in the MI phase. In other words, the ground state will be superfluid even for $J << U$.

In finite systems, one still finds the thermodynamic phases but the transition between them will be 'soft'. The characteristic sharpness of the transition (i.e. the non-analyticity of the derivative of some operator $\mathcal{O}$, $\partial\mathcal{O}/\partial x = \infty$) is lost. The geometry of the confining traps, e.g. an inhomogeneous trap, can further change the characteristics and critical values of the phase transition [72, 73].

3.2.1 Definitions of superfluidity

In the last section, we have found that the MI - SF transition can be described by the energy gap of the excitations of the ground state. Superfluidity is not just the absence of Mott insulation, however. In a situation where we already know that the transition will be between an MI phase and a SF phase, the excitation energy gap would be sufficient indication. Depending on the system characteristics,

however, there can also exist other phases such as the Bose glass phase (insulating, but gapless and compressible, usually present only for disorder) [53].

Consequently, we need to explore more specific signatures of a superfluid as well. This is not entirely trivial as there are diverse definitions for the SF phase [74, 75, 76]. Their main difference lies in the distinction between the response of the superfluid to a *static* perturbation versus a *dynamic* perturbation. The reason for these divergences is possibly caused by the fact that the concept of superfluidity can be taken to cover more than one phenomenon. As explained by Leggett in [77], there are at least two effects which can cause the phenomenon of 'frictionless flow' which was the original motivation for the concept of superfluidity. One phenomenon, the so-called Hess-Fairbank effect, is a manifestation of the equilibrium behaviour of the system while the other effect is characterized by metastability.

For the purposes of this thesis, both definitions are equivalent as we will study the MI - SF transition for $T = 0$ only. To emphasize the link between Bose-Einstein condensation and superfluidity, we will define the superfluid density as a coefficient in the effective long-wavelength action which governs phase fluctuations. We can immediately see that a condensate will always be superfluid.

An alternative definition of the superfluid density can be found by using the response of the system to moving boundaries [75, 76]. The superfluid fraction is then dependent on the kinetic energy of the superflow that is imparted by a twist of the boundary condition.

The relation between these two definitions is discussed by Roth in [76].

3.2.2 Experimental signatures of the MI - SF transition

The BHM Hamiltonian appears to be relatively simple but the physics it gives rise to is not. Specifically, it has been difficult to observe the MI - SF transition in a real system, despite much theoretical and experimental attention [40, 41, 64, 73, 76, 78, 79]. This may be partly due to the fact that the phase transition is characterized by an avoided level crossing rather than an actual level crossing. Consequently, for finite lattices, the transition will not be sharp. Mostly, though, the difficulty of experimental confirmation of the MI - SF transition is simply down to the difficulty of gaining indications of the transition from the experimentally accessible variables.

The experimental procedure used to observe the MI - SF transition utilizes the change in the momentum pattern as, for example, in the seminal experiment by Greiner *et al.* [40]. This change in the momentum distribution is tracked by

absorption imaging [20] the cloud after a given time of flight. Typically, all confining potentials (optical and magnetic) are switched off so that the cloud can drop onto a screen. Switching off the confinement not only causes the atoms to drop under the influence of gravity, it also allows the cloud to expand. The expansion of the cloud brings with it that the localized wave functions of each lattice site (assuming the tight-binding approximation) overlap and thus form an interference pattern which reveals the momentum distribution of the system. This interference pattern can then be imaged by a CCD camera when the atoms hit the screen. An example of typical experimental data for this method can be seen in Fig. 3.2.

For a shallow lattice, one finds so-called Bragg peaks in addition to the zero-momentum peak that is characteristic of a BEC in the absence of an optical lattice. These Bragg peaks first become more pronounced with increasing lattice depth and then abruptly begin to weaken and eventually vanish altogether (see Fig. 3.2).

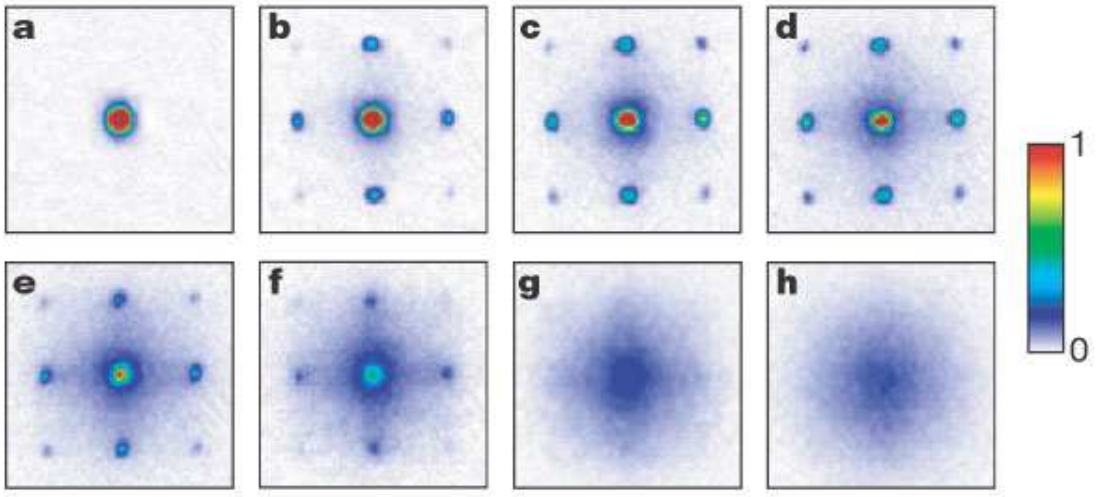

Figure 3.2: Reproduced with kind permission from Ref. [40]. It shows absorption images of multiple matter wave interference patterns which were obtained after suddenly releasing the atoms from an optical lattice potential with different potential depths V_0 after a time of flight of 15 ms. Values of V_0 were: a, $0E_R$; b, $3E_R$; c, $7E_R$; d, $10E_R$; e, $13E_R$; f, $14E_R$; g, $16E_R$; and h, $20E_R$, where E_R is the recoil energy of Eq. (2.13).

The relation of Bragg peaks to the MI - SF phase transition is not entirely straightforward. As we mentioned earlier, the interference pattern after expansion of the cloud reflects the momentum distribution across the lattice. This implies that the presence of Bragg peaks in the observed pattern is an indicator of (off diagonal) long-range coherence across the lattice. This implication is a result of the fact that the momentum distribution $n(\mathbf{k})$ for atoms confined to the lowest

band of the lattice can be expressed in terms of the exact one-particle density matrix $\rho_1(\mathbf{x}_i, \mathbf{x}_j) = \hat{a}_i^\dagger \hat{a}_j$ [64, 80],

$$n(\mathbf{k}) = n|w(\mathbf{k})|^2 \sum_{x,x'} \exp(i\mathbf{k}(\mathbf{x} - \mathbf{x}'))\rho_1(\mathbf{x}, \mathbf{x}'), \tag{3.7}$$

where $w(\mathbf{k})$ is the Fourier transform of the associated Wannier wave function. The summation is carried out for all separations $\mathbf{x}-\mathbf{x}'$ that are equal to integer multiples of the lattice basis vectors. The one-particle density matrix in turn describes coherence across the lattice. Consequently, when atoms are allowed to expand and fall freely, the resulting interference pattern shows the momentum distribution.

In the extreme limits of zero phase coherence and maximal long-range phase coherence, the interpretation of the presence or lack of Bragg peaks with regard to the MI - SF phase transition is straightforward. No phase coherence whatsoever implies a complete lack of overlap of wave functions between sites. This means that the eigenstates of the system are now Fock states, an energy gap has opened and the system is in the MI phase. At the other end of the spectrum, phase coherence across the entire lattice allows the definition of the condensate fraction n_0 through the maximal value of ρ_1 by $\lim_{|\mathbf{x}-\mathbf{x}'|\to\infty} \rho_1 = n_0/n$ (n is the total density). When the entire system has a 'common' condensate fraction, i.e. we can define a condensate that extends across the lattice, it is in the superfluid phase [81].

It has been shown [76], however, that the change of phase coherence around the MI - SF phase transition does not correspond exactly to the change in the superfluid fraction. In the MI regime, phase coherence can still extend over several lattice sites even though the long-range coherence is gone. Consequently, these off-diagonal elements in the one-particle matrix can still cause Bragg peaks to appear in the interference pattern. In other words, while Bragg peaks in the interference pattern can indicate the phase of the system for extreme conditions, they are not in themselves good observables for tracking the transition point.

In the analysis up to now, we have assumed a homogeneous system where the atom density is constant across the lattice. In experiments, however, optical lattices are usually created inside a trap due to the need for additional confinement of the atoms. This additional potential causes a variation in the atom density across the lattice so that we now have a range of critical values for $(U/J)_{\text{crit}}$ as this is dependent on the MI phase density. Even more importantly, depending on the strength of the perturbation through the additional trapping potential, the nature of the phase transition itself can change to the point where it can no longer be

characterized by global behaviour [72, 73]. (For similar results regarding the Bose-Einstein phase transition, see [82]). Instead, a pattern of SF and MI "domains" should form. The emergence of a domain of MI phase will then cause restructuring of the spatial distribution of the superfluid component which in turn will result in a fine structure of the particle momentum distribution. This fine structure, visible in the central momentum peak, may be a more useful observable to locate the point of the MI - SF transition, but has not been confirmed experimentally yet.

So far, we have focussed on evidence of superfluidity. As we discussed in the previous section, the other side of the coin, i.e. the MI phase, has more properties than simply the absence of superfluidity. Most prominently, for a homogeneous system, the MI phase is characterized by an energy gap. The existence of this gap has been verified experimentally [40, 41] by applying a (static or dynamic) force in the MI phase. After application, the system is rapidly and non-adiabatically transferred back to the SF phase. The resulting excitations are then measured by switching off all potentials, allowing the cloud to expand and measuring the resulting interference pattern. The strength of these excitations is assumed to be reflected in the full width at half maximum (FWHM) of the central interference peak. While this measure underestimates small gains in excitational energy, it gives a good picture of the qualitative features of the excitation spectrum [41]. The dependence of excitations on the applied force then shows the extent of an MI energy gap - for an example of experimental data, see Fig. 3.3.

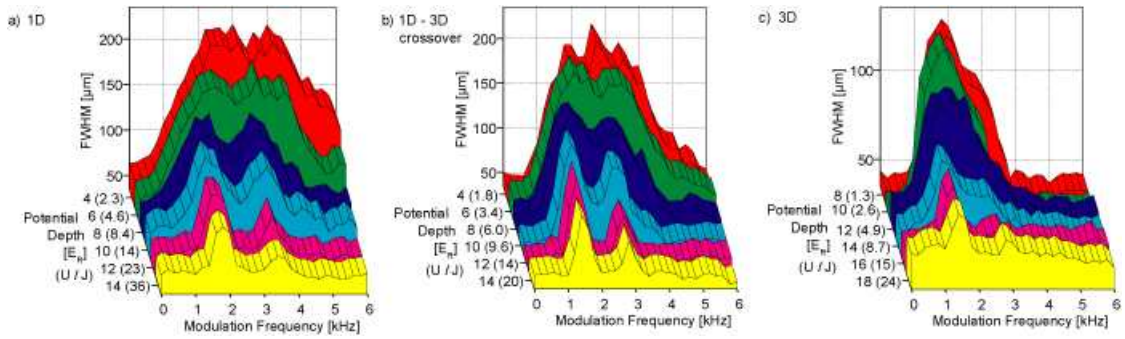

Figure 3.3: Reproduced with kind permission from Ref. [41]. The figures show the FWHM of the central interference peak for an array of gases with different dimensionalities (1D, 1D-3D crossover and 3D). Within each plot, excitation spectra are compared for different lattice potential strengths. The values for U/J in brackets were calculated using a band structure model with tight-binding approximation.

This approach has the disadvantage of disturbing the system with an additional perturbation. If the force is too high or the perturbation time too long, the energy

gap can be wiped out by heating before it can be measured. To avoid this effect, methods such as Bragg spectroscopy that use very weak perturbations have been utilized experimentally. We shall discuss the details of the experimental implementations of the energy gap measurement in the context of our results below.

In conclusion, we find that there are a range of possible indicators of the MI - SF transition. Due to the finite system size (both in experiments and in theory), a sharp transition point is not present, but it should be possible to see a gradual change between phases. So far, the experimental realizations of indicators of superfluidity are fraught with difficulties. Possible alternatives have been suggested in literature, but not yet tested experimentally. The MI phase, however, thanks possibly to its local character, can be established with more confidence.

Chapter 4

"Static" excitations

In this chapter as well as in Chapter 5 and 6, we will discuss original work carried out by the author during the course of her doctorate.

The experimental feasibility of adding a linearly varying component to the lattice potential, so-called tilting, has opened up a new way to study the MI to SF phase transition. In this chapter, we will present numerical simulations of this technique which enable us to compare the effect of such tilting on states with various degrees of reduced number fluctuations. Our focus is on the region of the phase transition where the repulsion between atoms is larger than the hopping amplitude and strong number squeezing results. This work follows the general lines we set out in [83].

4.1 Experimental interest

There are many interesting potential applications that arise from adding a static force to BECs in optical lattices. For one, there is considerable interest in the use of such systems for high precision interferometry [84, 85]. Other experiments are focussed on finding Bloch oscillations [59]. Most prominently perhaps, static excitations have been employed [40] to probe the MI - SF phase transition.

As we discussed the trapping of atoms in optical lattices in Chapter 1, we only give a brief review here. Conceptually, it is fairly simple. One first creates a condensate through laser cooling and evaporative cooling, holds the condensate in a trap and then gradually ramps up the strength of the lattice potential created by interference of laser beams. Obviously, this involves a number of experimental

challenges in order to be able to carry out these procedures with sufficient efficiency, but these have been overcome by a number of groups.

Once the lattice has been created, the question arises as how best to probe the atoms. In this chapter, we will look at the application of a static force to the lattice in this context.

A number of different probes using static forces have been used in experiments. In one of the earliest experiments [37], the optical "lattice" was positioned so that gravity caused a potential difference between sites. Other experiments [40] perturbed the lattice within a harmonic magnetic trap. A variation in the trapping field can be used to produce a gradient in the force on the atom. Moving the lattice from the centre of the trap will thus create a static force along the lattice. A third approach [59] relies on a steady acceleration caused by switching one of the lattice beams on suddenly and ramping the intensity of the other up gradually. This so-called chirping of the lattice is a very precise way of imposing a force on the atoms in the lattice.

4.2 Theory

As we discussed in Chapter 3, the MI phase is characterized by atoms being localized in the wells. The further we proceed into the MI phase, the closer the ground state is represented by a Fock state with distribution $\psi = |N_p N_p \dots N_p\rangle$ where $N_p = N_{\text{total}}/N_s$ is the number of atoms per site. As a consequence of this localization, the signature of the MI phase is more directly related to the observables that have been experimentally accessible so far than signatures of the SF phase.

In consequence, we focus on the characteristics of the MI phase and treat the encroaching features of superfluidity - present as this is a gradual transition - as perturbations of the localized atom picture. This allows us to interpret the excitations present in our system in a relatively simple number-basis picture.

As we discussed in Chapter 3, the excitations for a perfect MI phase in an infinite lattice should occur at energies of

$$\Delta(U, J) = |E_{\text{part}}| - |E_{\text{hole}}| = |UN_p - \mu| - |(-U(N_p - 1) + \mu| = U, \tag{4.1}$$

i.e. Δ is independent of the number of particles per site N_p or the chemical potential μ. The effect of the static force, of course, is to create an energy difference between sites. When this energy difference between neighbouring sites is equal to the energy

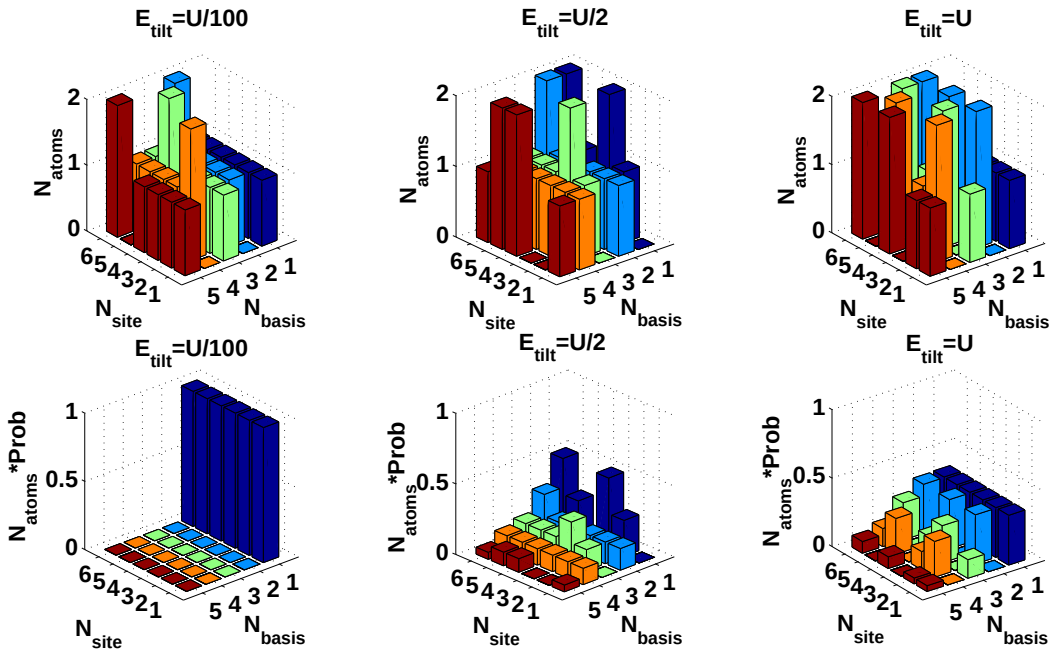

Figure 4.1: Top row: Number of atoms per site for the first five number states and $E_{\text{tilt}} = U/100$ (left), $E_{\text{tilt}} = U/2$ (middle) and $E_{\text{tilt}} = U$ (right). Bottom row: Number of atoms per site, but multiplied with the probability for the wave function to be in this state. All values are for $N_p = 1$ and $N_s = 6$.

U contained in a excitation of the ground state, we expect to find a resonance. For the infinite lattice, resonances correspond to the creation of a particle-hole pair. In the Hamiltonian, the energy difference is implemented by adding a site-dependent energy in the form of

$$\widehat{\mathcal{E}} = \sum_k \mathcal{C}_k \hat{n}_k \tag{4.2}$$

where $\hat{n}_k$ is the number operator $\hat{n}_k = \hat{a}_k^\dagger \hat{a}_k$. For $\mathcal{C}_k = kU$, the difference between adjacent sites is then just equal to U. We refer to a lattice with additional site-dependent energy of the form of Eq. (4.2) as a tilted lattice.

The location of the particle-hole pairs created by the additional term in the Hamiltonian depends on the strength of the applied force. From now on, we shall discuss the force in terms of the energy difference it creates between neighbouring sites and term it E_{tilt}. When this energy difference is equal to the particle-hole excitation energy U, we expect to find a resonant creation of particle-hole pairs from adjacent sites. As the tunneling probability depends on the overlap between sites, the nearest neighbour resonance for adjacent particle-hole pairs should be the strongest. In addition to this, we should see weaker resonances at multiples of U.

These correspond to the simultaneous creation of a number of nearest neighbour particle-hole pairs and are consequently energetically possible, but less probable. The exact relation of these 'multiple' excitations to the simple particle-hole excitation is dependent on the size of the lattice. For an infinite lattice, the probability for an n particle-hole excitation should simply be P^n where P is the probability of a single particle-hole excitation. Finite lattice size manifests itself in a further decrease of the probability for n particle-hole excitations when $n \to N_s$.

Another interesting possibility is the creation of particle-hole pairs from non-adjacent holes. The energy needed to produce one such particle-hole pair is again equal to U. The energies E_{tilt} between adjacent wells are then fractions of U. For example, a particle-hole pair created in next nearest neighbour sites should be found for $E_{\text{tilt}}=U/2$, adding up to a total energy difference of $U/2 + U/2 = U$, while larger distances are reflected in resonances at even smaller fractions of U. In general, particle-hole pairs that are n sites apart will appear for energy differences between adjacent sites that are equal to $U/(n+1)$.

In principle, a combination of simultaneous creation of multiple particle-hole pairs together with creation in non-adjacent holes could cause resonances at other fractions of U, e.g. nU/m. As these processes are much less probable than the simple resonances at nU and U/n, $n \in \mathbb{N}$, they are unlikely to be of much importance in the general resonance spectrum.

We are, of course, not able to study an infinite lattice. The particle-hole picture still works surprisingly well even for our moderately-sized lattice, however. To illustrate this, we have plotted the wave function for $U/J = 50$ and $N_p = 1$, $N_s = 6$ for various values of E_{tilt} in the number state basis in Fig. 4.1. To increase the clarity of our plots, we show the effects on the five states with the largest probability coefficients only. In the top row of plots in Fig. 4.1 we plot the number of atoms per site for these five states for a non-resonant force ($E_{\text{tilt}}=U/100$), a next nearest neighbour resonance ($E_{\text{tilt}}=U/2$) and a nearest neighbour resonance ($E_{\text{tilt}}=U$). To illustrate the occupation probability for these states, we plot the number of atoms per site multiplied by the probability of the number state in the bottom row of plots. In other words, if we plotted the five number states

$$|111111\rangle,\ |111201\rangle,\ |110211\rangle,\ |201111\rangle,\ |102111\rangle$$

in one of the bar plots on the top, the bottom plot would have the row vectors ϕ_i

$$\begin{aligned}
\phi_1 &= |\langle 111111|\psi\rangle|^2 \, |111111\rangle \\
\phi_2 &= |\langle 111201|\psi\rangle|^2 \, |111201\rangle \\
\phi_3 &= |\langle 110211|\psi\rangle|^2 \, |110211\rangle \\
\phi_4 &= |\langle 201111|\psi\rangle|^2 \, |201111\rangle \\
\phi_5 &= |\langle 102111|\psi\rangle|^2 \, |102111\rangle.
\end{aligned}$$

For the very small, off-resonance energy $E_{\text{tilt}}=U/100$, we then find the expected result for a state far into the MI phase: a very high probability (about 99 %) for the system to be in the MI ground state $|111111\rangle$. At $E_{\text{tilt}}=U/2$, we see clear signs of next nearest neighbour hopping. Four of the five most probable states show a next nearest neighbour particle-hole pair (the fifth is the $|111111\rangle$ ground state). Similarly, the righthand plots with $E_{\text{tilt}}=U$ show nearest neighbour hopping. Both for $E_{\text{tilt}}=U$ and $E_{\text{tilt}}=U/2$, we find that the probability of the ground state is far lower than the 99 % of $E_{\text{tilt}}=U/100$. In other words, the excitation of the system is high. We find that a plot of the mean value of the number variance for $U/J = 50$ and time period $\tau = 0$ – $\tau = 10/J$, as in Fig. 4.2, also shows these resonances (both fractional and integer) clearly.

Due to the finite size of the lattice and $J \neq 0$, we find that our results show excitations at additional values for U/J even for squeezed configurations, as is visible in Fig. 4.2. In order to support the assumption that these additional excitations describe real physics and are not down to numerical error, we also plot some of the transition probability matrix elements $\mathcal{M}_{n,1}$ for the applied force. These matrix elements are defined as

$$\mathcal{M}_{i,j} = \langle \psi_i | \widehat{\mathcal{E}} | \psi_j \rangle. \tag{4.3}$$

i.e., they represent the probability of the perturbation by the energy operator $\widehat{\mathcal{E}}$ coupling eigenstate i with eigenstate j. $\widehat{\mathcal{E}} = \sum_i \mathcal{C}_i \hat{n}_i$ is the energy operator we defined in Eq. (4.2). In Fig. 4.2, we show the matrix elements for the transition probability from the ground state to excited states, $\mathcal{M}_{n,1}$, where n designates the nth excited state. We find that the matrix elements are in good agreement with the location and width of the main peak. We will see that the slightly broader tail of the main resonance at $E_{\text{tilt}} = U$ is caused by Bloch oscillations.

As might be expected, excitations closer to the phase transition are less easy

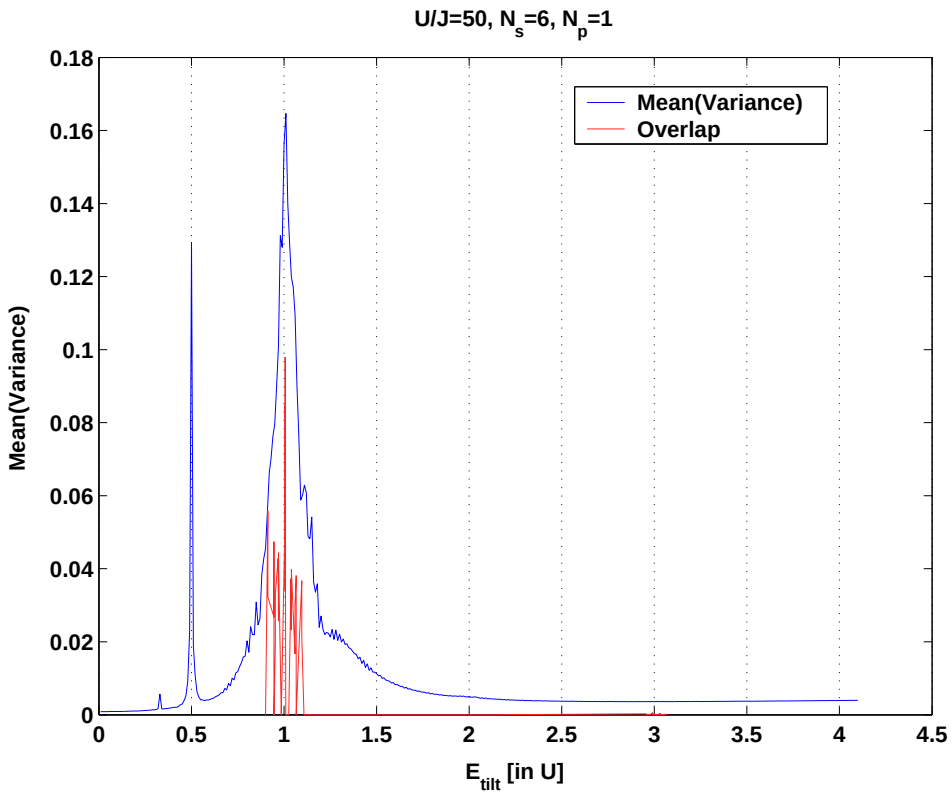

Figure 4.2: The blue line shows the mean value of the number variance. The average is carried out over the perturbation period from $\tau = 0/J$ to $\tau = 10/J$. The red lines show the matrix elements $\mathcal{M}_{n,1}$ for overlap with the ground state. Values are for $U/J = 50$ and $N_s = 6$, $N_p = 1$.

to understand in a particle-based picture. After all, the SF phase is characterized by the delocalization of atoms across the entire lattice. Close to the phase transition, therefore, the wave function should be spread out over the number state basis. For delocalized particles, our formalism of particle-hole excitations does not give an accurate description of the physics as particles cannot be thought of as localized to a well. Consequently, a description of excitations in terms of particles hopping from one well to another does not make sense. In other words, a lack of excitations understandable in a particle-hole formalism indicates closeness to the phase transition between the localized MI phase and the delocalized SF phase. A study of the matrix elements $\mathcal{M}_{n,1}$, $\mathcal{M}_{n,2}$, $\mathcal{M}_{n,3}$ and $\mathcal{M}_{n,4}$ for such a transition state ($U/J = 1$), as plotted in Fig. 4.3, shows good agreement between the excitation spectrum and overlap. In other words, even when excitations cannot be understood in the particle-hole picture, there still is a correspondence between the overlap matrix elements of the static system and the excitations found in our

simulations.

It should be noted that transition states show a significantly larger number of non-zero matrix elements than those in the MI phase. This can be understood through the behaviour of the energy gap E_{G}. As E_{G} vanishes with the approaching phase transition, the difference between eigenstate energies grows smaller as well by definition. This means both that more states are populated and that the range of states i and j, for which some given E_{tilt} has a non-zero matrix element grows larger.

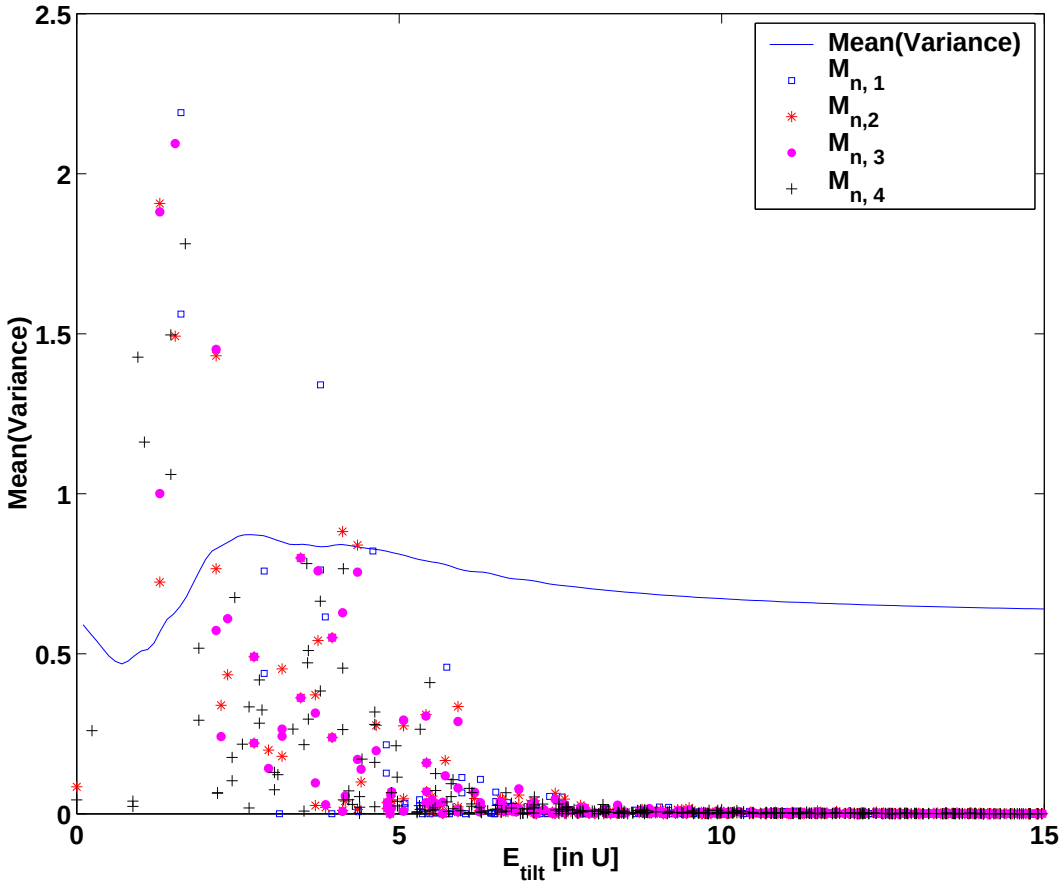

Figure 4.3: The blue line is the mean of the number variance for $t = 0$ - $t = 10/J$ and $U/J = 1$, $N_s = 6$, $N_p = 1$. The additional elements show the location and strength of some of the overlap matrix elements $\mathcal{M}$. Blue diamonds: $\mathcal{M}_{n,1}$, red star: $\mathcal{M}_{n,2}$, magenta dot: $\mathcal{M}_{n,3}$, black +: $\mathcal{M}_{n,4}$.

In the superfluid regime, e.g. at $U/J = 0.001$, the excitation process lacks distinctive features. Due to the delocalization across the lattice, there is no gap to overcome in order to add energy to the lattice. Consequently, the perturbation strength simply varies smoothly with the strength of the applied force. In Fig. 4.4, we show the dynamics of the number variance over time for the SF phase and

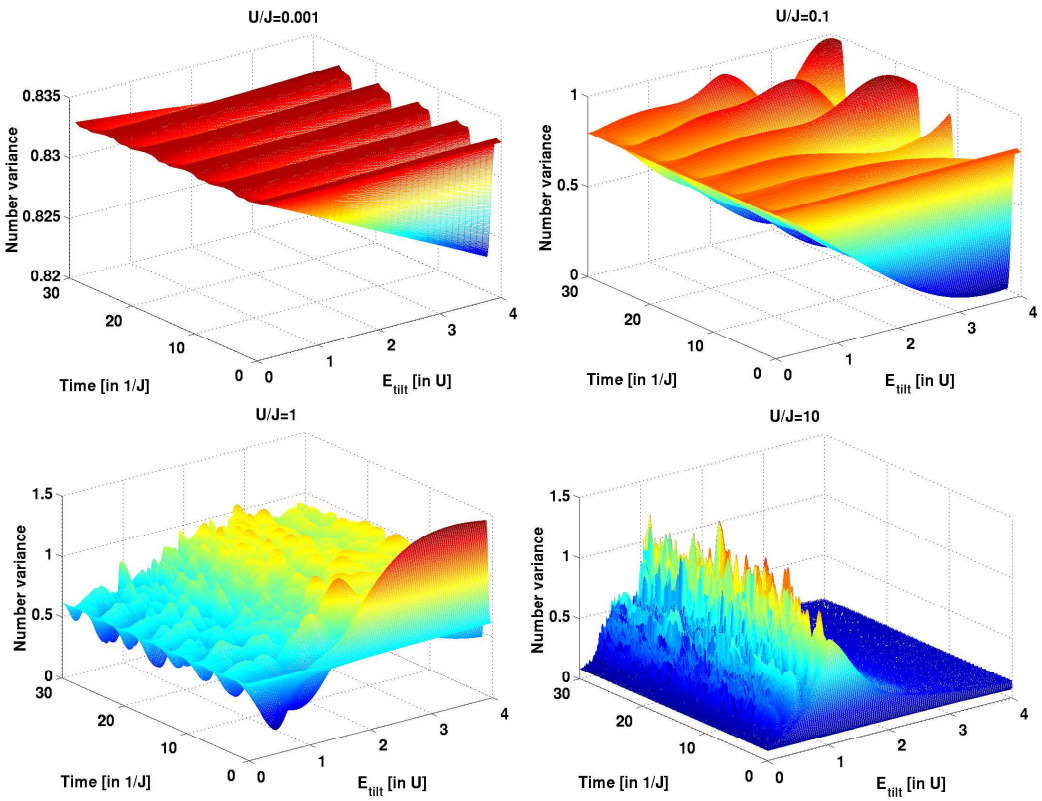

Figure 4.4: Top row: SF phase ($U/J = 0.001$, left plot) and transition phase ($U/J = 0.1$, right plot), bottom row: transition phase ($U/J = 1$, left plot), MI phase ($U/J = 10$, right plot). All values are for $N_s = 6$ and $N_p = 1$.

transitional states. The oscillatory structures visible in that figure are caused by a combination of Bloch oscillations and oscillations at the tunneling frequency, both of which will be discussed further in Chapter 6. Below, we will argue that the number variance dynamics provide a useful tracker of the phase transition due to its local nature.

4.3 Numerical setup

For all calculations in this chapter, we use the Bose-Hubbard model, as described on page 12, with an added energy term shown in Eq. (4.2) where the Hamiltonian is equal to

$$\widehat{H}_{\mathrm{BHM,\,add}} = -J \sum_{\langle i,j \rangle} \hat{a}_i^\dagger \hat{a}_j + \sum_i \mathcal{C}_i \hat{a}_i^\dagger \hat{a}_i + \frac{1}{2} U \sum_i \hat{a}_i^\dagger \hat{a}_i^\dagger \hat{a}_i \hat{a}_i. \tag{4.4}$$

The notation $\langle\rangle$ denotes summation about all nearest neighbours. As we are especially interested in the region of the phase transition, we chose to use an exact approach based on the full Hamiltonian to study the dynamical development of the system. This limits our studies in size and number of atoms and we consider modestly-sized lattices with between four and eight sites and mean atom numbers N_p of up to three atoms per site. The exact approach does, however, allow us to study developments right at the phase transition, which would not be possible for mean field theories based on the Bogoliubov or Gross Pitaevskii approach.

Experiments that demonstrate the SF to MI transition typically involve many more lattice sites than this [40, 41, 85, 86]. By considering the evolution of what we expect to be locally determined quantities such as the number variance, we are, however, able to minimize the effects of finite size on our results. This, in turn, allows us to gain some insight into the behaviour of larger lattices than we are able to treat numerically. When comparing results for different numbers of lattice sites, we find that they show remarkably similar behaviour, encouraging us in our use of the number variance as an indicator of lattice response. Due to the qualitative similarity of the zero-temperature phase diagram for one, two and three dimensions [53, 64] we also believe that, while we use a one-dimensional system for numerical simplicity, the general features of our results can be applied to higher-dimensional systems.

We study our system by solving the coupled equations of motion for the components of the wave functions in the number state basis using a fifth order Runge-Kutta approximation [87]. The initial states for the simulations are the eigenstates of the Hamiltonian given in Eq. (4.4) for different values of U/J. We obtain these eigenstates by exact diagonalization of the Hamiltonian. The eigenstates are then probed by tilting the lattice in our simulations. This tilting is implemented by adding a linearly varying component $\widehat{\mathcal{E}}$ (Eq. (4.2)) to the on-site energy E_j. Further details of the numerical approach will be set out in Appendix A.

There are a number of observables that we can use to track the effect of excitations. Primarily, we will study the number variance $\mathcal{V}$, defined as

$$\mathcal{V} = \langle(\hat{n}_i)^2\rangle - \langle\hat{n}_i\rangle^2, \tag{4.5}$$

where $\hat{n}_i$ is the number operator for site i and $\langle\rangle$ denotes the expectation value. Why use the number variance? As discussed in Chapter 3, excitations in the MI phase are usually measured experimentally (e.g. in [86]) via changes in the interference patterns observed in the distribution of atoms released from the lattice. Excitations

caused by tilting the lattice show up in the increased width of the main interference peaks found when the system is taken back into the SF phase [86]. In other words, these excitations are observed through changes induced in the phase coherence across the lattice.

For single wells, number fluctuations $\mathcal{V}$ and the phase coherence ϕ across the well are related by the uncertainty relation

$$\sqrt{\mathcal{V}}\delta\phi \geq 1 \tag{4.6}$$

which states that the simultaneous measurement of number and phase is limited in precision.

There is no such relation between the number fluctuations of one well and the phase coherence across the lattice. That becomes immediately obvious by considering that it is theoretically possible to count all the atoms in one well without destroying the phase coherence between the other lattice sites.

A reasonable assumption to make, however, is that a decay of the 'local' phase coherence at each lattice site will cause the decay of the 'global' phase coherence across the lattice at some point. Consequently, a change in number fluctuations should be reflected in the interference pattern in some form and vice versa.

In the extreme limits (i.e. for a lattice with infinite barrier height or an absent lattice), the relation between the two observables is simple. Deep in the insulator state there is no phase coherence so that $\delta\phi >> 0$ and correspondingly zero number variance. For a superfluid, the number variance is large while the phase across the whole system is well defined - $\delta\phi \approx 0$.

We are, of course, interested in what happens in the transition region. While the use of number variance in the theory of BEC and the relationship between phase coherence and number variance has been discussed for some cases [88, 86, 89], a simple relation between the two has not been found. Quite to the contrary, it has been shown [76] that such quantitative measures as the fringe visibility of the interference pattern have no immediate relation to the fluctuations in the number variance.

We should note that the number variance is also an experimentally accessible quantity. It directly affects the collapse and revival times of the relative phase between sites [86, 88, 89, 90, 91, 92]. It also plays a role in the three-body loss rate: the three-body correlation function G_3^i is strongly dependent on the number variance [93]. We can also think of the number variance in terms of so-called

number squeezing. The MI phase states with vanishing number fluctuations are then number squeezed.

Consequently, the dynamics of the number variance are of theoretical and experimental interest in their own right. At the same time, they can also serve as an indication of what might be expected to happen in the interference pattern.

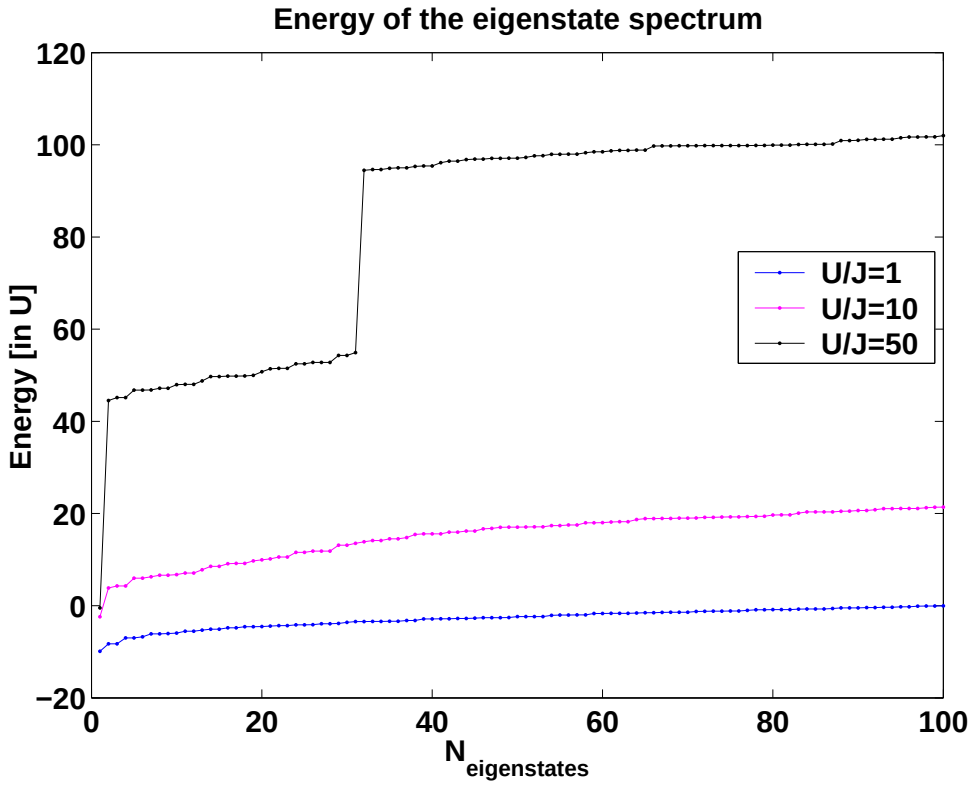

Figure 4.5: In this plot we show the energy for the first 100 eigenstates for $U/J = 1$, 10, and 50 (bottom to top) and $N_s = 6$ and $N_p = 1$.

Using the ground state of the Hamiltonian (calculated by exact diagonalization) as the inital state allows us to study the change in E_{G} directly as we can calculate the energy eigenspectrum. As we discussed earlier, the phase transition will not be sharp in a lattice of finite size. For the MI - SF transition in a finite lattice, this translates into a gradual onset of the energy gap. We find a similar effect for the energy eigenspectrum of our simulations. In Fig 4.5, we plot some exemplary energy eigenvalues for a number of values of U/J that are studied in our simulations: for the transition region ($U/J = 1$), we see indeed that no gap is observable. As expected, states further into the Mott insulator regime ($U/J = 10$ and $U/J = 50$) show a definite gap, even though the bands are still broadened.

4.4 Results

We study the dynamical evolution of the BHM Hamiltonian for a number of reasons. Firstly, we want to explore the excitational structure around and beyond the phase transition. Secondly, we want to investigate the use of the energy gap as an indicator of the phase transition. In order to do that, we shall compare the use of number variance to other observables, such as the added energy and change in the interference pattern, to gain an idea of how useful the various observables might be.

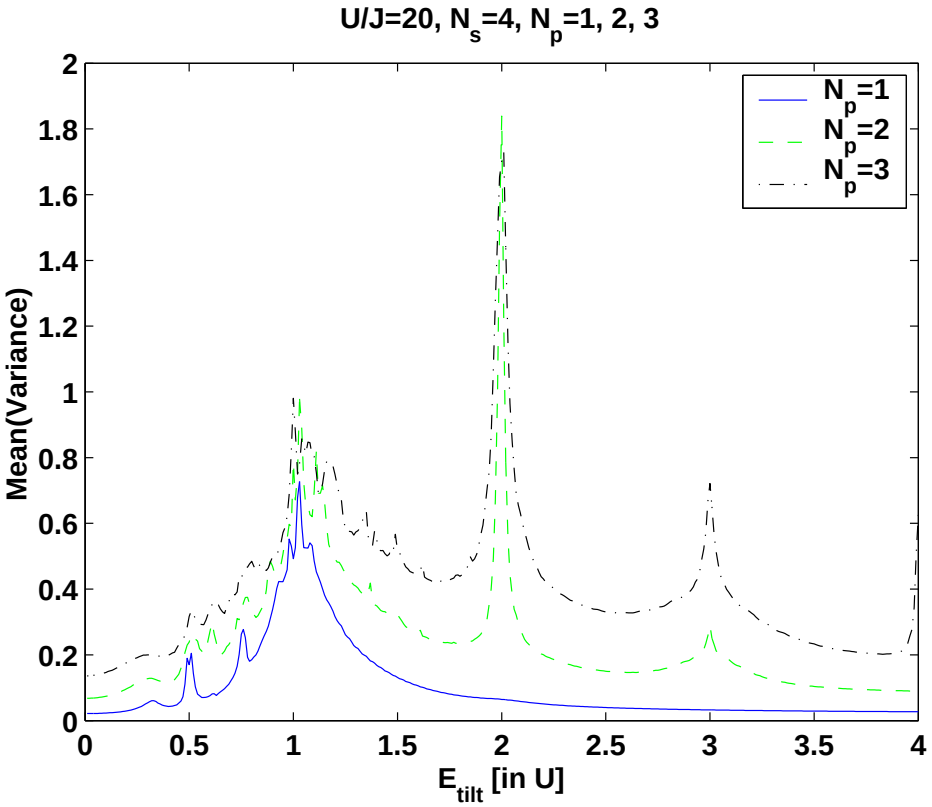

Figure 4.6: Excitation pattern for $\tau_{\text{perturb}} = 2/J$, U=10, J=1, $N_s = 4$ and $N_p = 1, 2$ and 3 (bottom to top). The mean variance (y-axis) is dimensionless.

To these ends, we use states with a range of different degrees of number squeezing as the initial states in our simulations and apply a tilt for a time τ_{perturb}. We then determine the number variance $\mathcal{V}$, the added energy $\mathcal{E}$ and interference patterns for the resulting wave function of atoms in the lattice. We shall first discuss our results for number variance at some length and then explore the relation to the other observables.

We find that even for rather small lattices the location of peaks is in good agreement with those corresponding to particle-hole pairs expected for an infinite lattice. Fig. 4.6, for example, shows excitations for filling factors of one, two and three for four lattice sites. All these graphs show one-particle-hole excitations at $E_{\text{tilt}} \approx U$ and $E_{\text{tilt}} \approx U/2$. For $N_p \geq 2$, two, three and even four-particle-hole excitations appear.

It is interesting to note that the qualitative features are still present for non-integer filling. As is shown in Fig. 4.7, non-integer filling results in a more prominent continuous spectrum, as might be expected in a system with defects. However, we still see distinct Mott insulator peaks, albeit with somewhat greater widths.

Non-integer filling is of interest because the phase diagram for the infinite lattice (see Fig. 3.1) predicts that non-integer density should lead to a superfluid ground state as the density in the MI phase is pinned to integer values. Finding that the particle-hole excitations are still clearly visible is a good indicator that the 'soft' phase transition does have different features to those in an infinite lattice. In other words, the crucial property of non-compressibility is no longer present even though the excitation spectrum shows clear signs of a distinct energy gap. A similar effect has been noted for optical lattices in inhomogenous traps [72].

We now turn to the dependence of excitations on the number of lattice sites for a range of four to eight lattice sites. For more than five lattice sites and $U/J \geq 20$, the changes in the results as a function of lattice size become modest (see Fig. 4.8).

Even for the smaller configurations, i.e. four and five sites, the important features look qualitatively the same. This leads us to be reasonably confident of the relevance of the principal features of our calculations for the larger systems studied in laboratories. In studies of the convergence towards the thermodynamic limit of the mean momentum [94] in lattices, it was found that good convergence had set in for 12 lattice sites, provided the evolution time remained shorter than the tunneling time. Even eight lattice sites already showed good agreement. We study a local variable that should be less dependent on the size of the lattice than the mean momentum. In other words, the results of [94] appear to confirm our conclusion that we can consider dynamics in the MI phase as, at the very least, a good indicator for possible effects in larger lattices.

We have found that the number variance corresponds well to the expected particle-hole excitational structure. But how does it correspond to other observables? We can compare the number variance to the added energy E_{add} which we

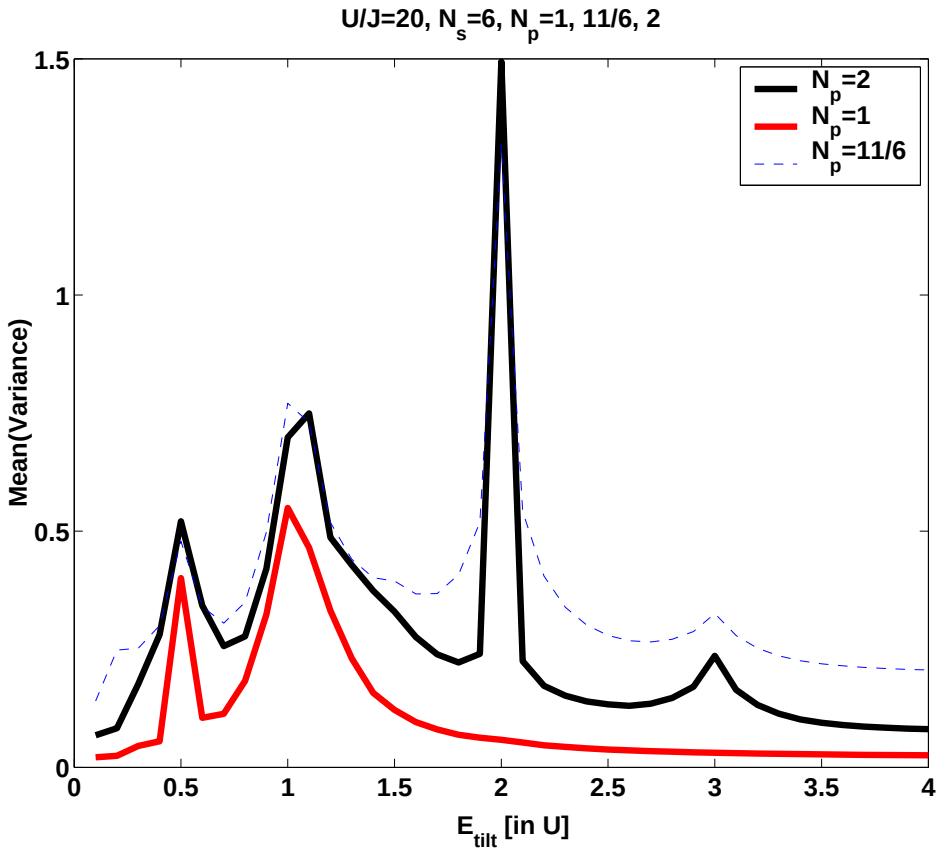

Figure 4.7: The thick lines show the mean of the number variance for integer filling (black $N_p = 2$, red $N_p = 1$), while the thin blue broken line shows results for $N_p = 11/6$. For all N_p, the mean value is taken over a perturbation period $\tau_{\text{perturb}} = 5/J$ and for values $U/J = 20$ and $N_s = 6$. The mean variance (y-axis) is dimensionless.

calculated by the expection value

$$E_{\text{add}} = \langle \psi(t) | H_{\text{BHM},0} | \psi(t) \rangle \tag{4.7}$$

where $\psi(t)$ is the wave function at time t and $H_{\text{BHM},0}$ is the BHM Hamiltonian for a non-tilted lattice. E_{add} is a global variable so we would expect agreement between $\mathcal{V}$ and E_{add} to be best for a system characterised by local quantities (i.e. the Mott insulator), while a superfluid might show greater differences.

Encouragingly, we find that even for a moderately squeezed system, i.e. for $U/J = 2$ shown in Fig. 4.9, the number variance mirrors the pattern of the added energy rather well. For more squeezed systems, the agreement is almost exact, as can be seen in Fig. 4.10 and in Fig. 4.11 for mean values.

One interesting feature to note is an additional fractional peak in the added

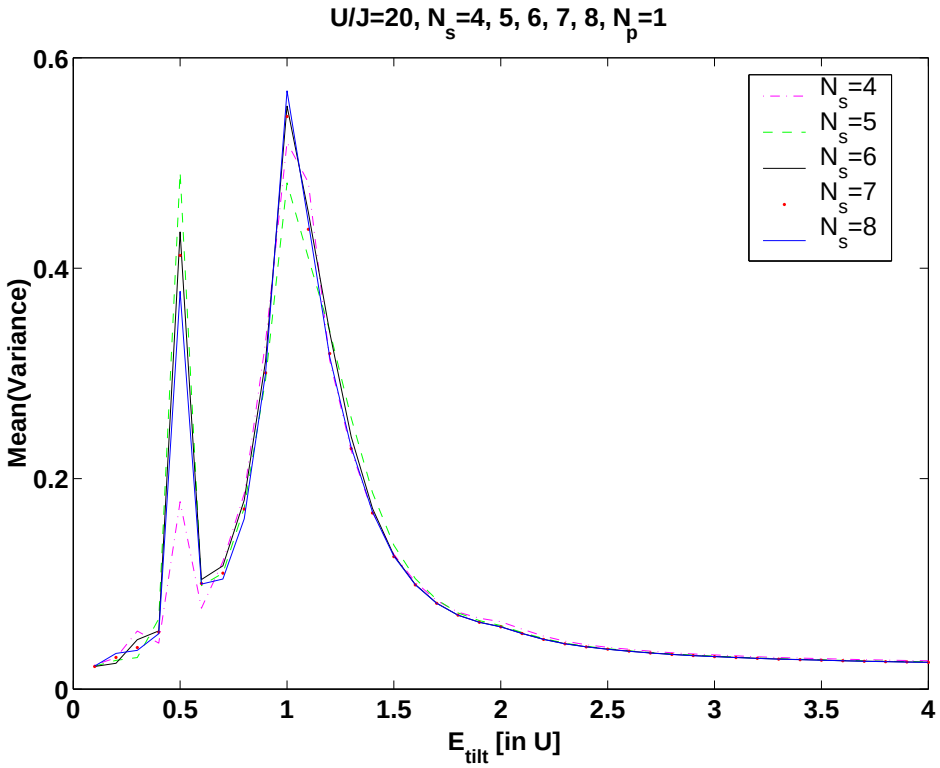

Figure 4.8: This plot shows the mean variance taken for t=0 - $7/J$ for $U/J = 20$, $N_s = 4, 5, 6, 7$ and 8 and $N_p = 1$. The mean variance (y-axis) is dimensionless.

energy plots for $U/J = 50$ in Fig. 4.10 and Fig. 4.11. Here, fractional peaks are visible not only, as expected from the simple model, at $E_{\text{tilt}} = U/3$ or even $E_{\text{tilt}} = U/4$, but also at $E_{\text{tilt}} = U/5$. This peak is not visible in the number variance plots, however.

In the simple infinite lattice picture, this excitation can be understood as a particle-hole excitation that is divided by four sites in between the particle site and the hole site. A look at the number state basis for a wavefunction produced by E_{tilt} confirms this relation: Fig. 4.12 shows quite clearly that the wave function after excitation is almost entirely a Fock state with $|011112\rangle$. This neatly illustrates the dangers of local variables: if they are only read out in specific points of the system, such as a site in the middle of the lattice, interesting effects involving different sites could be missed.

In this case, we have studied the number variance for states towards the middle of the chain to avoid end effects. Due to the limited size of our model, a fractional resonance at $E_{\text{tilt}} = U/5$ only shows up in the ends of the chain. The interference pattern and energy, on the other hand, which are global variables that are calculated

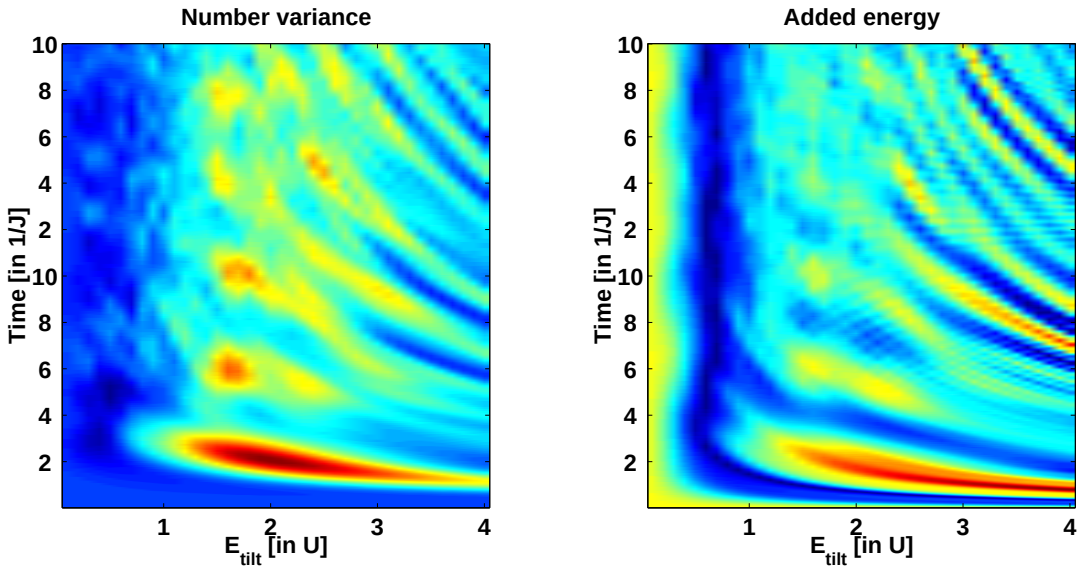

Figure 4.9: Left plot: contour plot of the number variance over time, right plot: contour plot of the added energy over time. Both are for $U/J = 2$ and $N_s = 6$, $N_p = 1$.

for the whole system, both show this effect. The relative strength of this excitation compared to other effects is an effect of the limited size of the systems.

There are a number of conclusions to draw from this. For one, studying the dynamics of the number variance gives us a very good idea of the change in energy - but only up to the point where the dynamic processes reach the size of the system. This is neither surprising nor worrying. Firstly, these dynamic processes only play a very minor role in the total excitation spectrum and do not provide any new information safe that we can extend possible excitations from hopping over four states to hopping over five. Secondly, the very fact that the number variance is a local quantity and thus, for highly squeezed systems, is sensitive to system conditions might offer possibilities for use in an experimental context. After all, theorists are currently predicting that bosons in optical lattices will - under the right circumstances - form domains rather than exist in one common phase for the entire system. A comparison of the excitational response of the number variance to that of a global variable such as the interference pattern could then possibly be an indicator of the size of these domains.

Due to numerical constraints, a comparison of dynamics of the number variance with the interference pattern could not be carried out in as great a detail as the comparison with the added energy. We shall discuss numerical results for a number of interesting cases that suggest good agreement betwen the conjugate variables

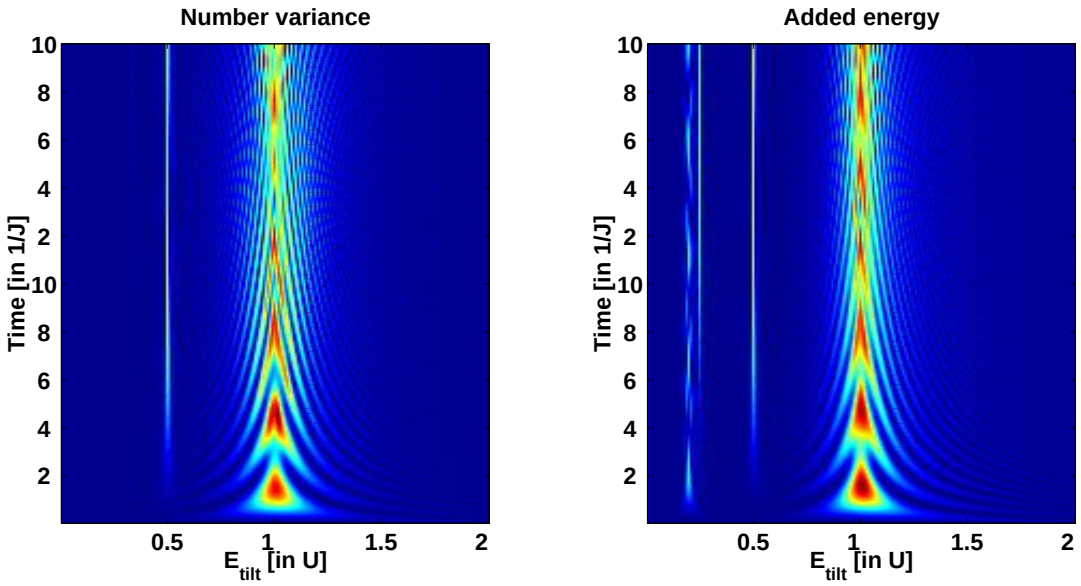

Figure 4.10: Left plot: contour plot of the number variance over time, right plot: contour plot of the added energy over time. Both are for $U/J = 50$ and $N_s = 6$, $N_p = 1$.

with respect to the main excitations.

We calculate the interference pattern as described in [80, 95] and Eq. (3.7) by

$$n(k) = \frac{1}{N_s} \sum_{\langle i,j \rangle} \exp(i\Delta\phi) \hat{a}_i^\dagger \hat{a}_j \tag{4.8}$$

where N_s is the number of sites and $\Delta\phi$ is equal to the phase difference between sites. The summation index i, j runs over all lattice sites.

In experiments, a change in interference pattern is usually quantified by taking the full width at half maximum (FWHM) of the main interference peak. For a small lattice such as ours, this is a rather imprecise measure as the main peak is less pronounced and the small changes are likely to be of the order of numerical uncertainty. Fig. 4.13 illustrates this difficulty: we have plotted the development of the interference pattern over time for a relatively squeezed state ($U/J = 50$) for a very small perturbation ($E_{\text{tilt}} = U/10$) and a strong perturbation ($E_{\text{tilt}} = U$). While the small perturbation produces the expected result - oscillation, but no sizable deviance from the initial pattern, the change in interference pattern for the resonant excitation is drastic, but hard to quantify as the peak and the point at which to take the FWHM are difficult to locate. For the purposes of this chapter, however, we are interested not so much in the precise nature of the relationship

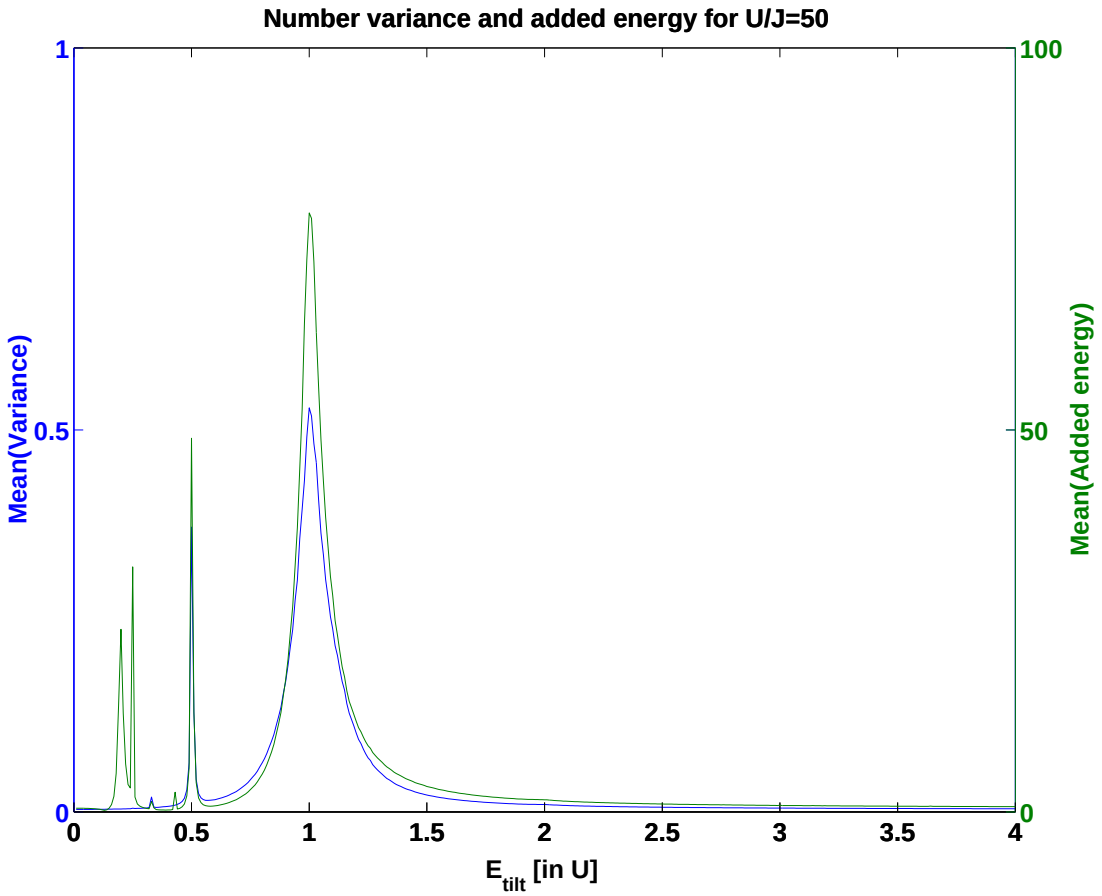

Figure 4.11: This plot shows mean values of the number variance (blue) and the added energy (green) taken for $U/J = 50$ and $N_s = 6$, $N_p = 1$ over the time period $\tau = 0 - \tau = 10/J$.

between the number variance and the interference pattern (after all, we already know that there is no one-to-one correspondence), but in the qualitative signatures of particle-hole excitations for the interference pattern. Consequently, the exact details of how to quantify change in the interference pattern are not of too much importance.

We therefore choose to plot the loss in height of the central momentum peak. This has the advantage of being simple to consistently measure for any pattern and can be used as a simple measure of the disturbance of the interference pattern by the exciting force. We find a very good correlation between excitations in the number variance (short: Var) and interference pattern (short: Int) even for relatively superfluid systems (Fig. 4.14, middle plot and right plot). As might be expected, the correspondence grows increasingly worse with the importance of long-range coherence (Fig. 4.14, left plot). Again, the gradual transition is visible in the

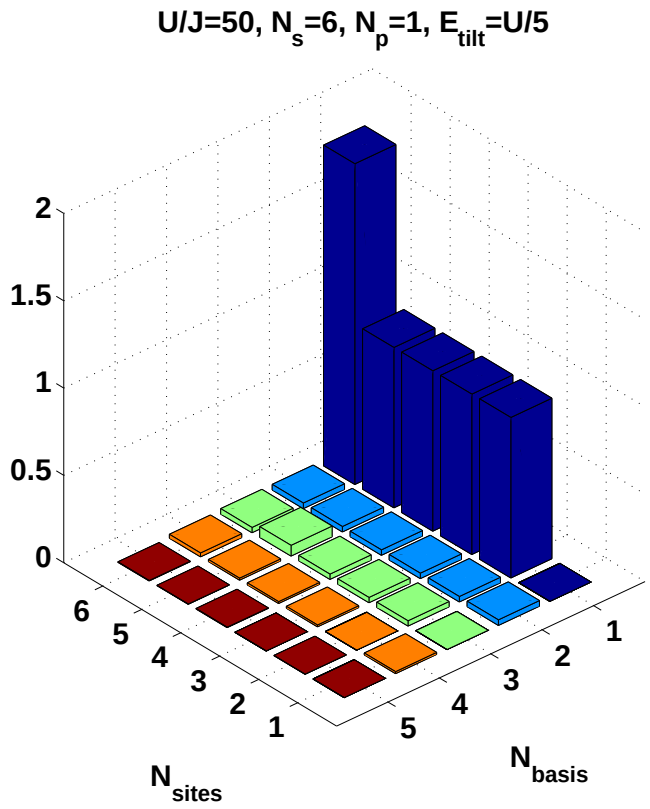

Figure 4.12: Analogous to Fig. 4.1, this plot shows the number of atoms per site multiplied with the state probability for $E_{\text{tilt}} = U/5$ and the initial conditions $U/J = 50$, $N_s = 6$ and $N_p = 1$.

excitational structure beyond the particle-hole excitations and smooth superfluid increase.

4.5 Summary

We have presented a range of simulations of atoms in an optical lattice in the region of a quantum phase transition. We have shown that the change in atom number variance is a good indicator of excitations produced by tilting the lattice potential. Moreover, we have seen that the main features of the excitation spectrum are only weakly dependent on the size of the lattice and confirm the origin of resonances seen in recent experiments [40, 41]. In addition, we observe higher order effects in the response that fit very well into the picture of excitations at multiples of the energy gap U in an infinite lattice. Our results also indicate that non-integer filling does not obscure the Mott insulator peaks in the response of the lattice. This implies that the change in atom number variance could be a useful probe even in

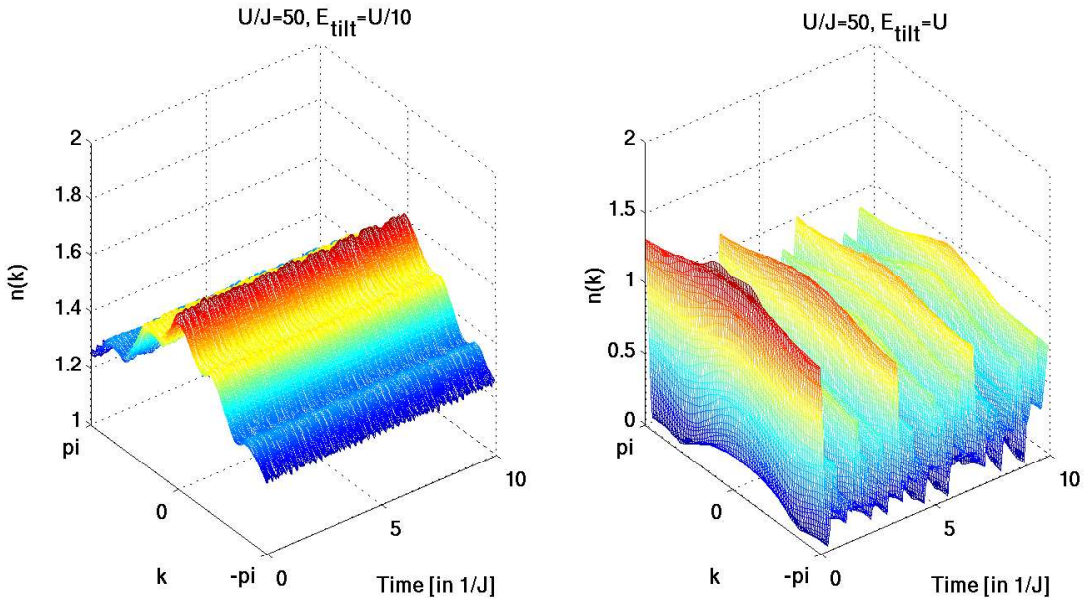

Figure 4.13: We have calculated the interference pattern as in Eq. (4.8) for $\Delta\phi = 1$. These plots show the development of the resulting $n(k)$ momentum distribution over time. The left plot shows the effect of a small perturbation ($E_{\rm tilt} = U/10$) while the right plot shows the momentum pattern for a resonant energy $E_{\rm tilt} = U$. All calculations are for $U/J = 50$, $N_s = 6$ and $N_p = 1$.

non-ideal systems, such as lattices with defects. It could also be a useful probe of phases that go beyond a pure MI phase or SF phase, but rather incorporate elements of both in a patterned structure.

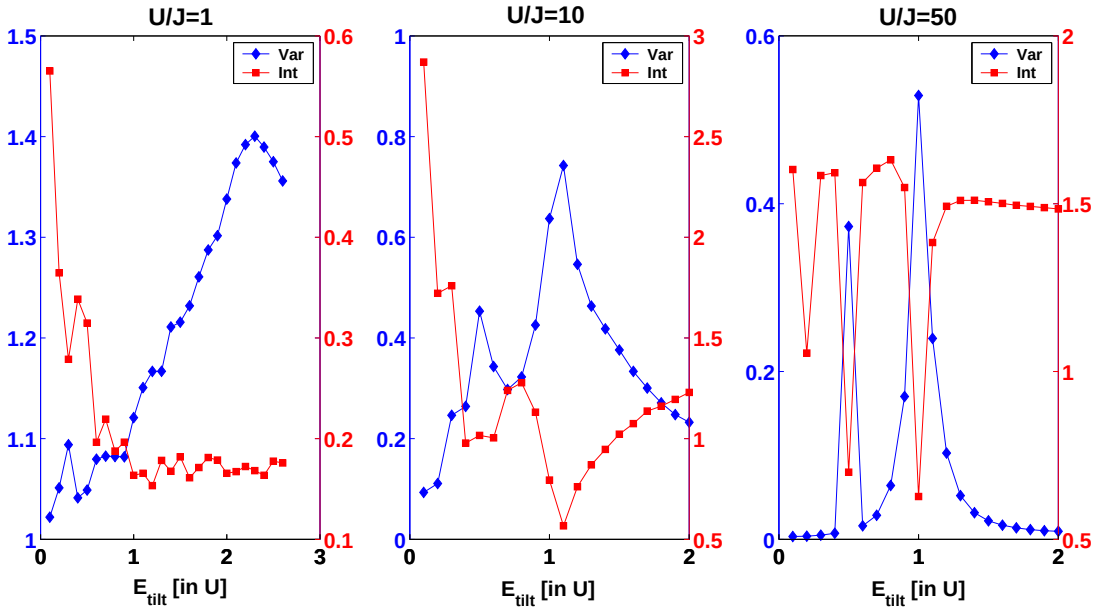

Figure 4.14: In these plots, we compare the mean value of number variance over time with the mean height of the main interference peak. Blue diamonds: number variance, red squares: height of interference peak. All values are calculated for $N_s = 6$ and $N_p = 1$.

Chapter 5

Time-dependent excitations

While the application of a static force as in Chapter 4 has proved to be extremely successful experimentally, it has a number of disadvantages. Most importantly, the magnitude of force needed for experimentally distinguishable signals can cause heating and thus destroy the very system it was intended to probe. A static force will also cause Bloch oscillations which, even though interesting in their own right, can make an analysis of the response of the system to excitations difficult.

One alternative approach is to use time-dependent excitations. In this chapter, we will discuss a specific experimental realization of this, Bragg spectroscopy, and its advantages. We will give a brief overview of the use of dynamical excitations and explain our numerical implementation of this method. Finally, we will set out the results of our numerics and discuss some possible consequences for experimental work.

5.1 Experiments

One of the interesting aspects of bosons in optical lattices is that they bridge the borderline between quantum optics and condensed matter physics. Experimentalists and theorists alike have transferred a wide range of techniques from both sub-fields to this system. The technique that we are interested in here, Bragg spectroscopy, has a very long history in condensed matter physics. It makes use of Bragg scattering, a process that was first demonstrated in 1912 by W.H. Bragg [96] for x-rays in crystals. He found that wave vectors are scattered when the Bragg

condition

$$n\lambda = 2d\sin\theta \tag{5.1}$$

is fulfilled. λ is the wavelength of the incoming wave, d the distance between lattice planes and θ the angle of incidence. It was later [97, 98] established that Bragg scattering is also applicable for particle de Broglie waves.

Bragg scattering of atoms off a standing light wave was first demonstrated in 1988 [99]. Experimentalists quickly realized the usefulness of this technique and it was used in a variety of experimental settings, ranging from manipulation of atomic samples in atom interferometers [100] to coupling out of Bose-Einstein condensates [101]. The term 'Bragg spectroscopy' was coined in 1997 by Berman *et al* in [102] in analogy to Raman spectroscopy. The authors show that a system where atoms are Bragg scattered by counterpropagating light waves with different frequencies can be reduced to that found for pump-probe spectroscopy of two or multilevel systems. In pump-probe spectroscopy, the system is excited by a so-called pump beam and then probed by a second beam called the probe beam. The momentum transfer $\mathbf{q}$ and energy transfer $2\pi\nu$ are then given by $|\mathbf{q}| = 2Nk\sin(\theta/2)$ and $\nu = N\Delta\nu$ where θ is the angle between the two beams with wave vector k and frequency difference $\Delta\nu$.

Experimental evidence of Bragg spectroscopy was soon found by Stenger *et al* [103] for a trapped condensate. The method was then applied to atoms in an optical lattice in 2004 [41]. In contrast to the static force we discussed in Chapter 4, Bragg spectroscopy is not very susceptible to Zener tunneling or other heating effects. The Bragg scattering scheme can be implemented by modulating the lattice potential with a sinusoidal amplitude modulation $A_{\mathrm{mod}}\sin(2\pi\nu t)$ in a one-dimensional optical lattice. With this modulation, two sidebands with frequencies $\pm\nu$ relative to the lattice laser frequency are added to the system. These then define the energy $2\pi\nu$ of the excitation. If this excitation energy $2\pi\nu$ corresponds to a resonance of the system, photons are absorbed and energy is transferred. The location of the resonances are found by subsequently ramping down the lattice potentials linearly, allowing atoms to rethermalize at a relatively shallow depth. All potentials (including the magnetic trap) are then suddenly switched off and the resulting matter wave interference pattern is detected by absorption imaging after ballistic expansion. As discussed briefly in Chapter 3, the full width at half maximum (FWHM) of the central momentum peak is taken as a measure of the introduced energy.

5.2 Numerical implementation

For our numerical model, we follow the design of a recent experiment [41] as described in the last section and add a sinusoidal modulation to the lattice potential of the Bose-Hubbard Hamiltonian (Eq. (2.14)). The new lattice potential V_{lattice} is then equal to

$$V_{\text{latt}} = V_0 \sin^2(kx)(1 + \mathcal{F}\sin(\omega t))$$

where $k = \frac{2\pi}{\lambda}$ is the lattice wave vector for a standing wave with wavelength λ and $\mathcal{F}$ is a dimensionless constant governing the strength of the perturbation.

Rather than keep the explicit space dependence of the second quantized Hamiltonian of Eq. (2.14), it is far more convenient numerically and conceptually to simplify it to the well-known BHM Hamiltonian, albeit with time dependent coefficients U and J.

As in Chapter 2 we once again assume that we can restrict the model to dynamics in the lowest band. We also make the assumption that the tight-binding approximation is valid.

The shape of the Wannier functions

$$\phi_{0+} = \frac{1}{\sqrt{\sqrt{\pi}\sigma}} \exp(-x^2/2\sigma^2) \tag{5.2}$$

then depends on the potential height since σ is determined by $V_{\text{latt}}(t)$. Following a method first proposed by Baym and Pethick [104], we calculate σ by minimizing the energy functional

$$E[\phi] = \frac{\hbar^2}{2m}\int \mathrm{d}x \left|\frac{\mathrm{d}\phi(x)}{\mathrm{d}x}\right|^2 + \int \mathrm{d}x\, V_{\text{latt}}(x,t)|\phi(x)|^2 + \frac{1}{2}g\int \mathrm{d}x\, |\phi(x)|^4 \tag{5.3}$$

for the given lattice potential. For $V_{\text{latt}} = V_0 \sin^2(kx)(1 + \mathcal{F}\sin(\omega t)$, the equation for σ is then equal to

$$(1+\mathcal{F})V_0 \sin(\omega t) N k^2 \sigma^4 \exp(-k^2\sigma^2) - \frac{N}{2m} - \sqrt{\frac{\pi}{2}}\frac{aN^2}{m}\sigma = 0. \tag{5.4}$$

Due to the exponential term, a closed solution to this is not easy to find. As we assume that the tight-binding approximation holds, however, it seems instructive to gain a simpler variational estimate by approximating the lattice potential by the harmonic form $V = \frac{1}{2}m\Omega^2 x^2$ where $\Omega = \sqrt{\frac{V_0(1+\mathcal{F})\sin(\omega t)k^2}{m}}$. In the tight-binding approximation, there is little overlap between sites. For the Gaussian function

ϕ_{0+}, localized mainly in the centre of the trap, the trapping potential is then well approximated by a harmonic trap. This approximation gives us the simpler form of

$$\sigma_{\text{int}}^4 = \left(\frac{1}{m\Omega}\right)^2 + \frac{4\pi a\sigma_{\text{int}}}{m\sqrt{2\pi}m\Omega^2}, \tag{5.5}$$

as shown, for example, in [52]. This approximation allows us to calculate explicit values for σ, using experimental parameters. It does not, however, give a single-valued function for the development of σ over time which would be significantly more convenient numerically. A first estimate of such a single-valued function can be found by neglecting the interaction energy in the energy functional $E[\phi]$ so that (5.3) changes to

$$E[\phi] = \frac{1}{2m}\int \mathrm{d}x \left|\frac{\mathrm{d}\phi(x)}{\mathrm{d}x}\right|^2 + \int \mathrm{d}x\, \frac{1}{2}m\omega^2 x^2|\phi(x)|^2. \tag{5.6}$$

It is then trivially easy to find σ :

$$\sigma_{\text{non-int}} = \sqrt{\frac{1}{m\Omega}} = \left(\frac{1}{mV_0k^2(1+\mathcal{F}\sin(\omega t))}\right)^{\frac{1}{4}} \tag{5.7}$$

where $\Omega = \sqrt{\frac{V_0\sin(\omega t)k^2}{m}}$. This is the well-known length scale for the ground state in a harmonic trap with potential $\frac{1}{2}m\Omega^2x^2$. We find that, for the parameters used in our system, $\sigma_{\text{non-int}}$ is a very good approximation of σ_{int}. Fig. 5.1 shows some exemplary values of $\sigma_{\text{non-int}}$ and σ_{int}.

The BHM constants J and U consist of integrals over Wannier functions, i.e. from Eqs. (2.18) and (2.19):

$$J = \int \mathrm{d}\mathbf{r}\, w^*(\mathbf{r}-\mathbf{R}_i)\widehat{H}_0 w(\mathbf{r}-\mathbf{R}_j) \tag{5.8}$$

$$U = 4\pi a_s \int \mathrm{d}\mathbf{r}\, |w(\mathbf{r}-\mathbf{R}_i)|^4 \tag{5.9}$$

where $\widehat{H}_0 = \hat{\mathbf{p}}^2/2m + V_{\text{latt}}(x,t)$ is the single particle Hamiltonian (2.9).

Carrying out the integration in Eq. (5.9) results in

$$U = 2\sqrt{\pi}a/\sigma \tag{5.10}$$

and

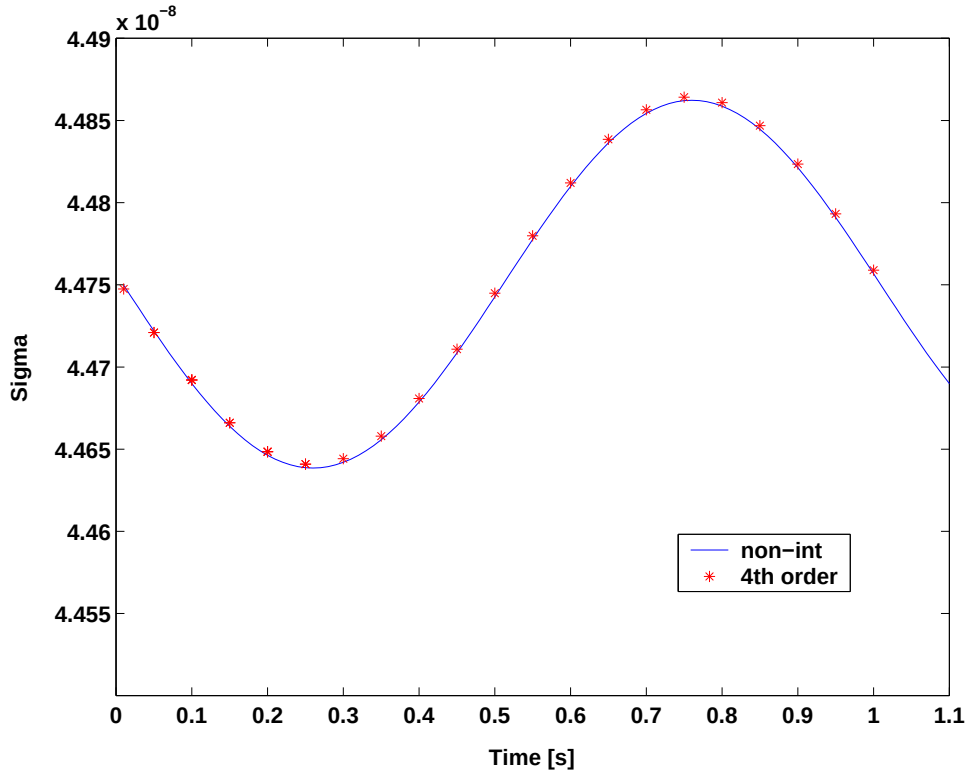

Figure 5.1: The blue line shows $\sigma_{\text{non-int}}$ (Eq. 5.7) while the red stars are calculated by the fourth order equation Eq. (5.5). System parameters are $V_R = 20E_R$ and $\mathcal{F}$=0.1.

$$J = \exp\left(-\frac{1}{4\sigma^2}\left(\frac{\pi}{k}\right)^2\right) \times \left[V_0(1+\mathcal{F}\sin(\omega t))(\frac{1}{2}+\exp(-k^2\sigma^2))\frac{1}{4m\sigma^2} - \frac{1}{2m\sigma^4}\left(\frac{\pi}{2k}\right)^2\right]. \tag{5.11}$$

After substitution of $\sigma_{\text{non-int}}$, J and U are equal to

$$U = 4\pi a\sqrt{\sqrt{mV_0(1+\mathcal{F}\sin(\omega t))}k} \tag{5.12}$$

$$J = \exp\left(-\frac{1}{4}\frac{\sqrt{mV_0(1+\mathcal{F}\sin(\omega t)}\pi^2}{k}\right)\left[\frac{V_0(1+\mathcal{F}\sin(\omega t))}{2} + V_0(1+\mathcal{F}\sin(\omega t))\exp\left(-\frac{k}{\sqrt{mV_0(1+\mathcal{F}\sin(\omega t))}}\right) + \frac{k}{4m}\sqrt{mV_0(1+\mathcal{F}\sin(\omega t))} - V_0(1+\mathcal{F}\sin(\omega t))\frac{\pi^2}{8}\right]. \tag{5.13}$$

A simple way of thinking about the effect of lattice height on J and U is by assuming that the overlap of wave functions between sites is so weak that it has, roughly, a linear dependence on the barrier height. In that case, a sine wave perturbation of V_0 translates into

$$J_{\text{perturb}} = J_0 \exp(-\mathcal{F} \sin(\omega t)) \tag{5.14}$$

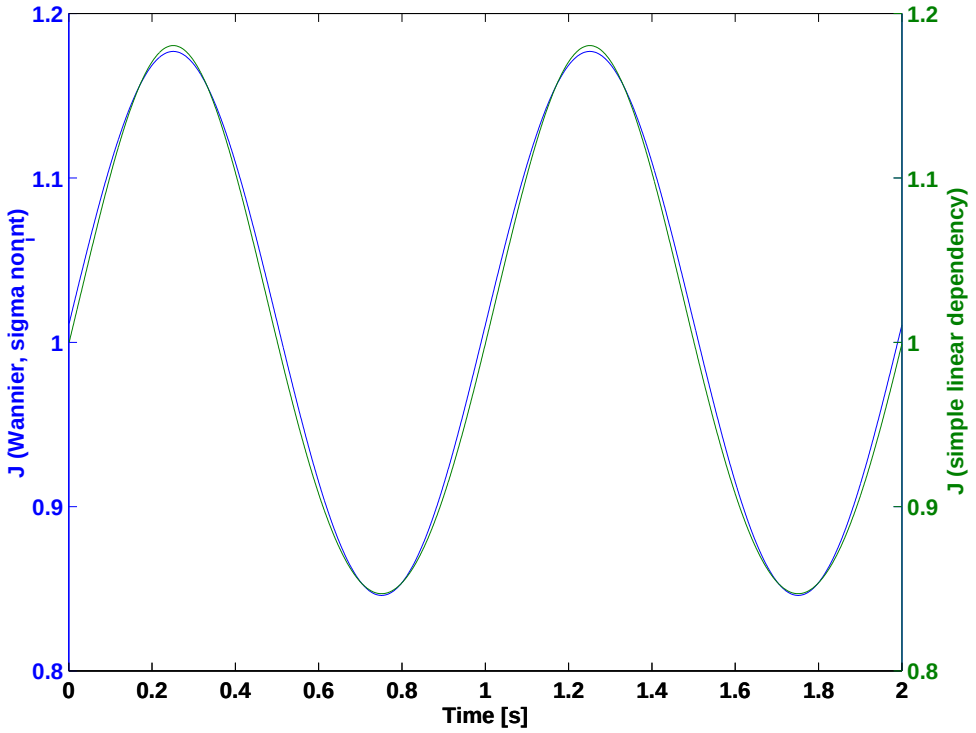

Figure 5.2: The blue line shows $J(\sigma_{\text{non-int}})$ and no interactions while the green line shows $J_{\text{perturb}} = J_0 \exp(-\mathcal{F} \sin(\omega t))$.

For the small perturbations used in experiments, we find that this very rough picture already produces results that are surprisingly similar to the more involved calculations discussed earlier. Fig. 5.2 shows both the change in J when calculating it with Wannier functions according to Eq. (5.12) and a simple sine wave perturbation as in Eq. (5.14).

The simple sine wave perturbation in Eq. (5.14) is essentially equivalent to the tight-binding approximation we made earlier. Consequently, we take the correspondence of the two perturbations of Fig. 5.2 as an indication that the assumptions we made in order to gain the time dependency we found for both J and U, are in good agreement with the system parameters.

5.3 Theory of excitations

The dynamics and excitation structure of the BHM has been the subject of much theoretical attention [105, 106, 107, 108, 109, 110, 111]. The simplest excitations are 'particle-like': as we discussed in Chapter 4, for an infinite lattice and a strongly interacting system, we can understand most effects by approximating the eigenstates with Fock states. More complex, however, are the collective excitations which can take the shape of breathing modes or dipole modes, for example. The precise form of these excitations is highly dependent on various system parameters and phase space can be chaotic.

Our interest lies mainly with the 'particle-like' excitations as we would like to use dynamic excitations to explore the energy gap of the Mott insulator as well as the phase transition. In order to ensure that we mainly excite these 'particle-like' states, we will compare the energy eigenstates of the static system with the results of the perturbation. We assume that agreement between the energy eigenspectrum of the static system and the resonance frequencies of the perturbed system indicates that it is reasonable to use the static system to understand the excitation processes.

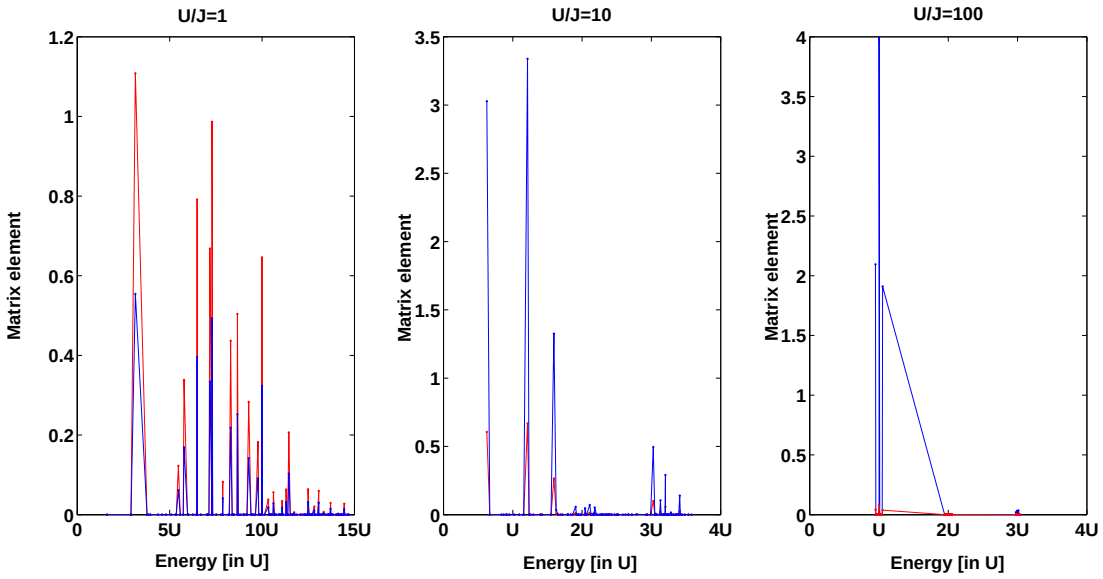

Figure 5.3: Red: $\mathcal{M}_U$, blue: $\mathcal{M}_J$. Values are calculated for $N_s = 6, N_p = 1$ and $U/J = 1$ (left), $U/J = 10$ (middle) and $U/J = 100$ (right).

Making the assumption that the system stays reasonably close to the static system, which resonances do we expect? In order to understand the effect of modulating J and U, we look at the matrix elements $\mathcal{M}$ of the overlap between the

initial wave function $|\psi\rangle$ (calculated by exact diagonalization of the Hamiltonian) and the perturbed wave function $|\psi\rangle_{\rm pert}$, i.e.

$$\mathcal{M}_{\rm J} = \langle\psi|J_{\rm mod}(t)\sum \hat{a}_i^\dagger \hat{a}_j|\psi\rangle, \quad \mathcal{M}_{\rm U} = \langle\psi|U_{\rm mod}(t)\sum \hat{a}_i^{\dagger 2}\hat{a}_i^2|\psi\rangle. \tag{5.15}$$

where $J_{\rm mod}(t)$ and $U_{\rm mod}(t)$ are the time dependent variables of the BHM Hamiltonian.

We find that only a small number of the possible eigenstates show matrix elements significantly larger than 0 (see Fig. 5.4 for a comparison of the range of eigenstates with the location of non-zero matrix elements.)

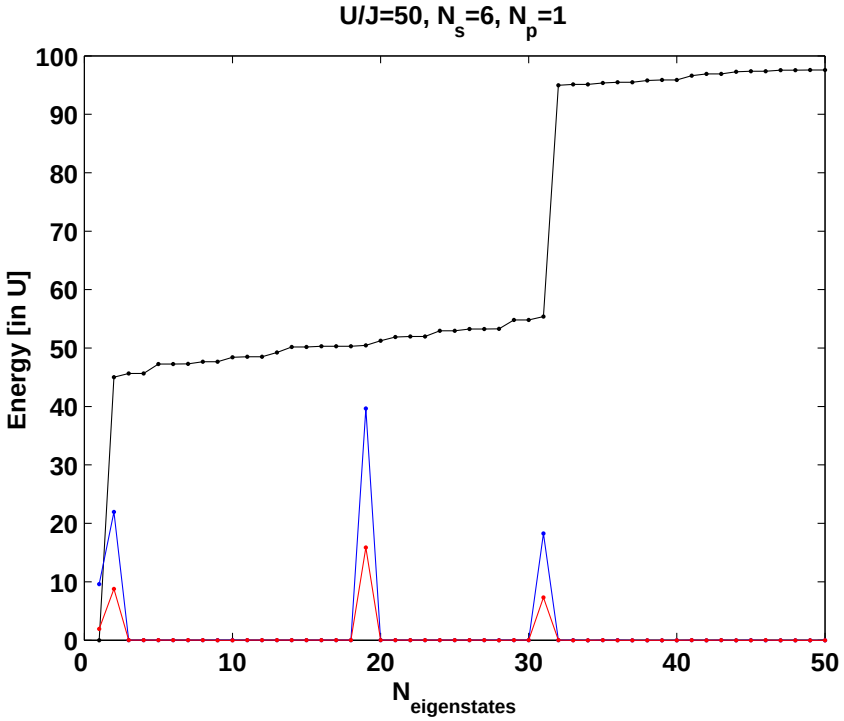

Figure 5.4: Red: $\mathcal{M}_U$, blue: $\mathcal{M}_J$. The black line shows the energy spectrum of the static Hamiltonian for $U/J = 50$, $N_s = 6$ and $N_p = 1$.

This may be a result of the symmetries of the system. Let us first consider the straightforward case of two atoms in two wells. The eigenstates of the system are then, in the number state basis, equal to

$$|\psi\rangle_1 = \mathcal{C}_1|11\rangle - \mathcal{C}_2(|02\rangle + |20\rangle) \tag{5.16}$$

$$|\psi\rangle_2 = \mathcal{D}_1|11\rangle + \mathcal{D}_2(|02\rangle + |20\rangle) \tag{5.17}$$

$$|\psi\rangle_3 = (|02\rangle - |20\rangle)/\sqrt{2} \tag{5.18}$$

where $|\psi\rangle_1$ is the ground state and $|\psi\rangle_3$ the state with the highest energy eigenvalue. $\mathcal{C}_{1,2}$ and $\mathcal{D}_{1,2}$ are dependent on the ratio U/J. Applying the perturbed Hamiltonian to the ground state then produces the new states

$$|\psi\rangle_{1,U} = U\sum \hat{a}_i^{\dagger 2}\hat{a}_i^2|\psi\rangle_1 = -2\mathcal{C}_2(|02\rangle + |20\rangle) \quad (5.19)$$

$$|\psi\rangle_{1,J} = J\sum \hat{a}_i^{\dagger}\hat{a}_j|\psi\rangle_1 = \sqrt{2}\mathcal{C}_1(|02\rangle + |20\rangle) - 2\mathcal{C}_2|11\rangle \quad (5.20)$$

It is then clear that the matrix elements $\mathcal{M}^U_{3,1} = \langle\psi_3|\psi\rangle_{1,U}$ and $\mathcal{M}^J_{3,1} = \langle\psi_3|\psi\rangle_{1,J}$ vanish due to the anti-symmetry of $|\psi\rangle_3$.

Obviously, larger lattices (and specifically those used in the simulations) have a much larger basis. Due to the high degree of translational symmetry, permutations of Fock states always have the same probability coefficient in the eigenstates. For example, all number states with N_p+1 atoms in one site, N_p-1 atoms in a second and N_p atoms in all other sites will have the same probability p. The amplitude $\mathcal{C}$ for each individual state can then only be equal to $\pm\sqrt{p}$. As both the interaction perturbation $U_{\mathrm{mod}}(t)\sum \hat{a}_i^{\dagger 2}\hat{a}_i^2$ and and the coupling perturbation $J_{\mathrm{mod}}(t)\sum \hat{a}_i^{\dagger}\hat{a}_j$ are symmetric operators, the overlap between eigenstates then depends on the ratio of positive $\mathcal{C}$ to negative $\mathcal{C}$. Further details of the physics of the overlap matrix elements will be the subject of future work (see also Chapter 7).

For experimental configurations, we expect the energy bands to be significantly more narrow so that overlap for single eigenstates is indistinguishable and we see a smooth curve over the band instead.

5.4 Results

There are a number of different effects we want to explore in this section. Firstly, due to the different dependencies of the hopping J and the interaction U on the perturbation strength $\mathcal{F}$, the response of the system to the perturbation will, in general, not just scale linearly.

Fortunately, for the weak perturbation strengths that we are interested in, both U and J are roughly linearly dependent on $\mathcal{F}$ as can be seen in Fig. 5.5. The relation of U to J, however, is not constant. This changing importance of $\mathcal{M}_U$ and $\mathcal{M}_J$ is illustrated in Fig. 5.3 - with growing squeezing, $\mathcal{M}_J$ is increasingly stronger than $\mathcal{M}_U$. This is a direct result of the ground state distribution in the number state basis. Roughly speaking, the probability for the system to be in the $|111\ldots1\rangle$ Fock state determines the strength of $\mathcal{M}_J$, while the matrix element $\mathcal{M}_U$

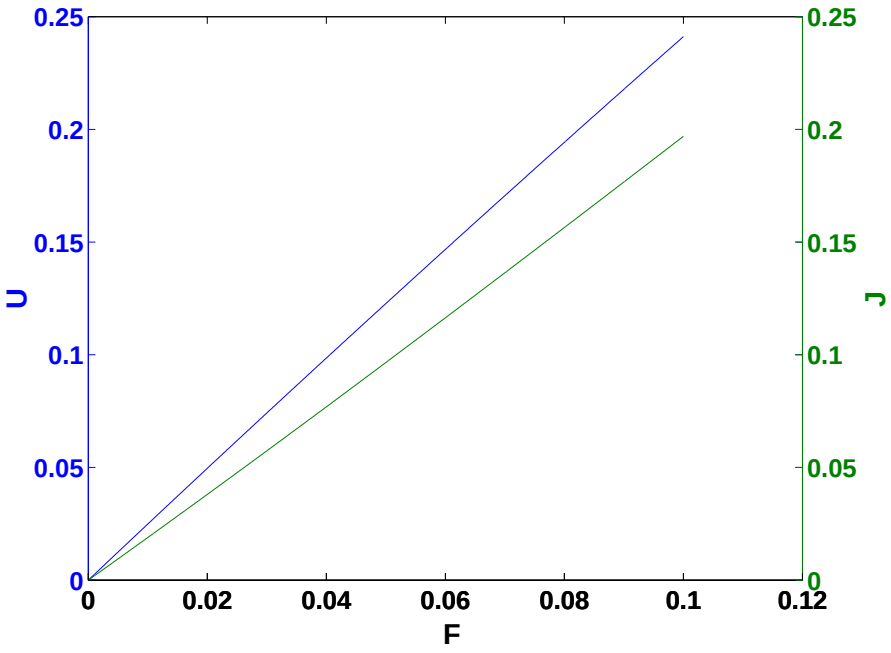

Figure 5.5: This plot shows the maximum value of perturbation (i.e. $\max(U_{\mathrm{mod}}(t))$ and $\max(J_{\mathrm{mod}}(t))$) for $J_0 = 1$ (green) and $U_0 = 10$ (blue) for $\mathcal{F} = 0.0001$ to 0.1.

is dependent on the probability of states with dipole elements, e.g. $|1 \ldots 0112 \ldots 1\rangle$. Consequently, while the location of excitations should be fairly independent of the strength of the perturbation, the relative strength of peaks should vary.

A comparison of the results for $\mathcal{F} = 0.001$ and 0.1 (see Fig. 5.6 for a detailed view and Fig. 5.7 for an overview) shows that, despite the large difference in perturbation strength, results show good agreement in the location of excitations. We do find that stronger perturbations produce a greater number of visible peaks, but this is due to the variation of the relative height of the peaks (see the detail in Fig. 5.6 for an example).

This agreement of scaling is important for a number of reasons. For one, the independence of location from the perturbation strength indicates that these excitations are indeed resonant effects coupling specific states rather than static heating effects. It also is a good indicator that the approximations made in the numerical model in the calculation of the time dependence of U and J do not detract from the fundamental objective of studying the system with a Bragg spectroscopy approach.

Another benchmark of the numerical model is the agreement of the matrix elements $\mathcal{M}_{U,J}$ for the static Hamiltonian (Eq. (5.15)) with the results of our

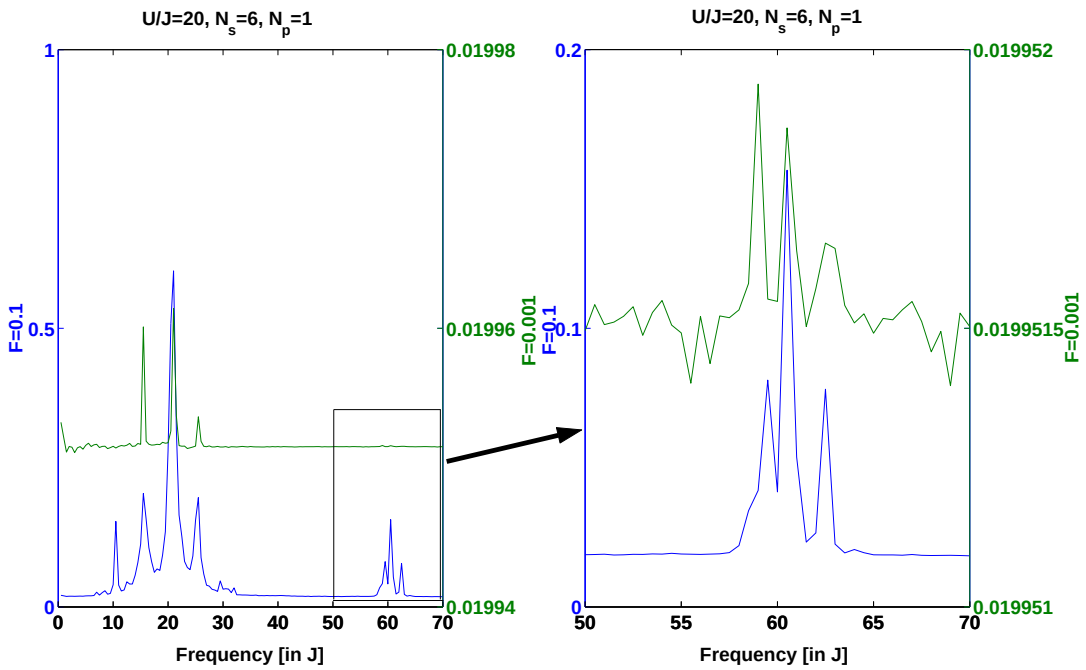

Figure 5.6: We compare the mean value of the number variance for different perturbation strengths and for $U/J = 20$, $N_s = 6$ and $N_p = 1$. Blue: $\mathcal{F} = 0.1$, green: $\mathcal{F} = 0.001$. Note that the y1-axis and the y2-axis do not have the same scaling.

simulations. The original motivation for the use of dynamic excitations was the possibility of exploring the energy spectrum of the system. Any perturbation of a system runs the risk of exciting it to such an extent that the energy spectrum suggested by the resonances bears no relation to that of the original configuration. In order to exclude this possibility, we compare our results with the original energy spectrum calculated by exact diagonalization of the static Hamiltonian.

Fig. 5.8 shows the mean value of the number variance over $\tau = 21/J$ for a system with non-integer filling (7 atoms in 6 sites). Due to the greater complexity of the eigenstates, the resonance spectrum is more varied than that for integer filling (as in Fig. 5.6). The left subplot shows the resonance spectrum together with the overlap calculated by exact diagonalization of the static Hamiltonian for perturbation of the coupling (red) and of the interaction (black). We find that, while the overlap corresponds well to peaks of the resonance spectrum, there are a number of peaks left unexplained. This is due to the fact that in case of a favourable transition between states (i.e. a non-zero matrix element), transition is possible for fractions as well as integer multiples of the original transition frequency ω. In the middle plot, we have added the matrix elements for $\omega/2$ and the right plot shows $\mathcal{M}_J$ and $\mathcal{M}_U$ for ω, $\omega/2$ and 2ω. All prominent peaks are then accounted

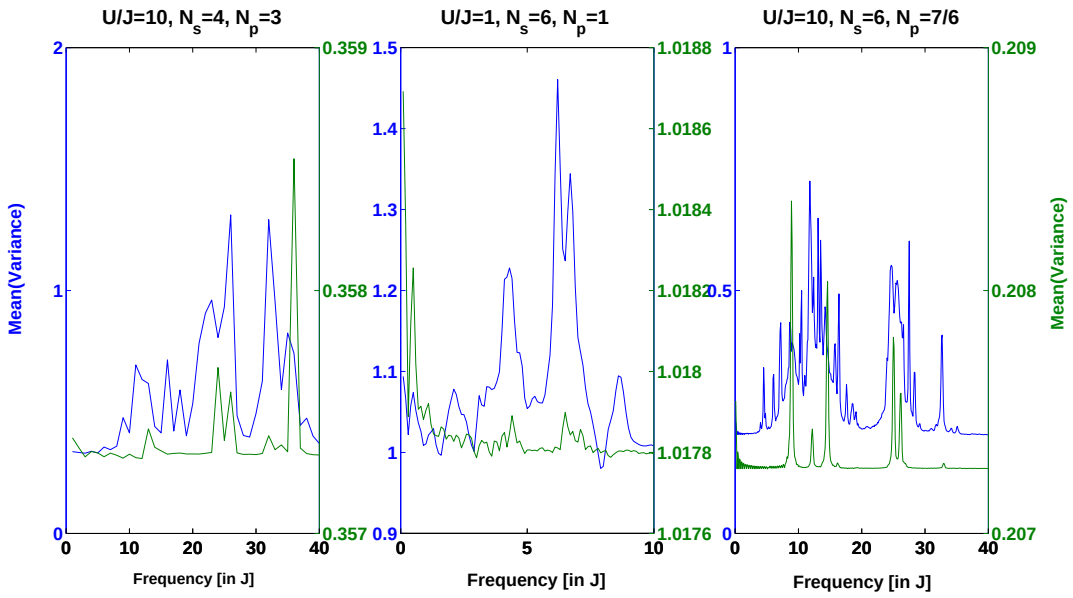

Figure 5.7: These plots show scaling for $\mathcal{F} = 0.001$ (green) and $\mathcal{F} = 0.1$ (blue) for $U/J = 10$, $N_p = 3$, $N_s = 4$ (left plot), $U/J = 1$, $N_p = 1$, $N_s = 6$ (middle plot) and $U/J = 10$, $N_p = 7/6$, $N_s = 6$.

for, which encourages us in the assumption that the resonance spectrum is a valid indication of the static energy structure. We find similar fractional and integer structures for the other possible configurations (i.e. integer filling, variation of U and J) as well (see also Fig. 5.13).

In order to understand the fractional resonances, we should remind ourselves of the interpretation of Bragg spectroscopy as a two-photon process, giving the integer resonances at (in the MI phase) $\approx U$. During these two-photon processes, one photon is absorbed und one emitted, coupling states to higher lying states of the energy spectrum. An additional possibility is a four-photon process where two photons are absorbed and two reemitted. This has been experimentally observed for Bragg scattering of atoms off a standing light wave [112]. Characteristic for a four-photon process is the simultaneous absorption of two photons with frequency ν which results in the coupling to a momentum state with energy of $4\pi\nu$.

The good correspondence of changes in the number variance with the original energy spectrum is also supported by a comparison with the added energy which we calculate by

$$E_{\text{add}} = \langle\psi(t)|H_{\text{BHM},0}|\psi(t)\rangle. \tag{5.21}$$

As with the static force in Chapter 4, changes in the number variance are closely correlated to this observable. We find that location, dynamics and relative heights

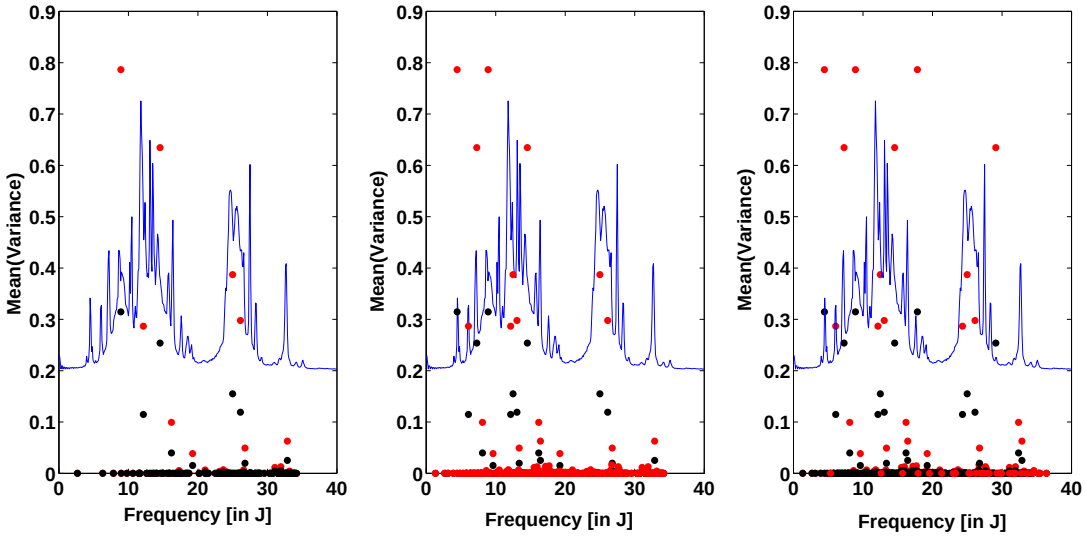

Figure 5.8: The coupling matrix elements are red dots (and scaled by 1/4 to fit), the interaction matrix elements are black dots. Left plot: $\mathcal{M}_{J,U;n,1}$, middle plot: $\mathcal{M}_{J,U;n,1} + \mathcal{M}_{J,U;n,1}/2$, right plot: $\mathcal{M}_{J,U;n,1} + \mathcal{M}_{J,U;n,1}/2 + 2\mathcal{M}_{J,U;n,1}$. All values are calculated for $U/J = 10$, $N_s = 6$ and $N_p = 7/6$.

agree very well for states in the MI phase, as Fig. 5.9 shows for $U/J = 20$. For superfluid states, however, the relative height of excitations changes drastically while the location and dynamics remain remarkably similar.

We also find that the location of changes in the interference fringe pattern corresponds both to the number variance and the added energy in the MI phase and transition phase, see e.g. Fig. 5.10. Their relative height, however, varies considerably. This is partly due to the relative simplicity of our indicator of interference pattern change - as in Chapter 4, we track the height of the central interference peak. This is related, but not identical to the FWHM as long as the peak stays roughly Gaussian and the momentum spread is only moderate. For high-momentum processes such as the four-photon process at $\omega/2$, the strength of the system perturbation could be underestimated. The fact that the resonances other than the main peak at $\omega \approx U$ show up so weakly in comparison to results for the added energy and number variance thus supports the assumption that these resonances occur for coupling to higher momentum states.

As discussed recently [76, 113], the correspondence between variance and interference pattern should break down at some point of the gradual transition, independent of all numerical considerations. This combination of agreement in the MI phase with increasing breakdown as the transition to the SF phase is approached

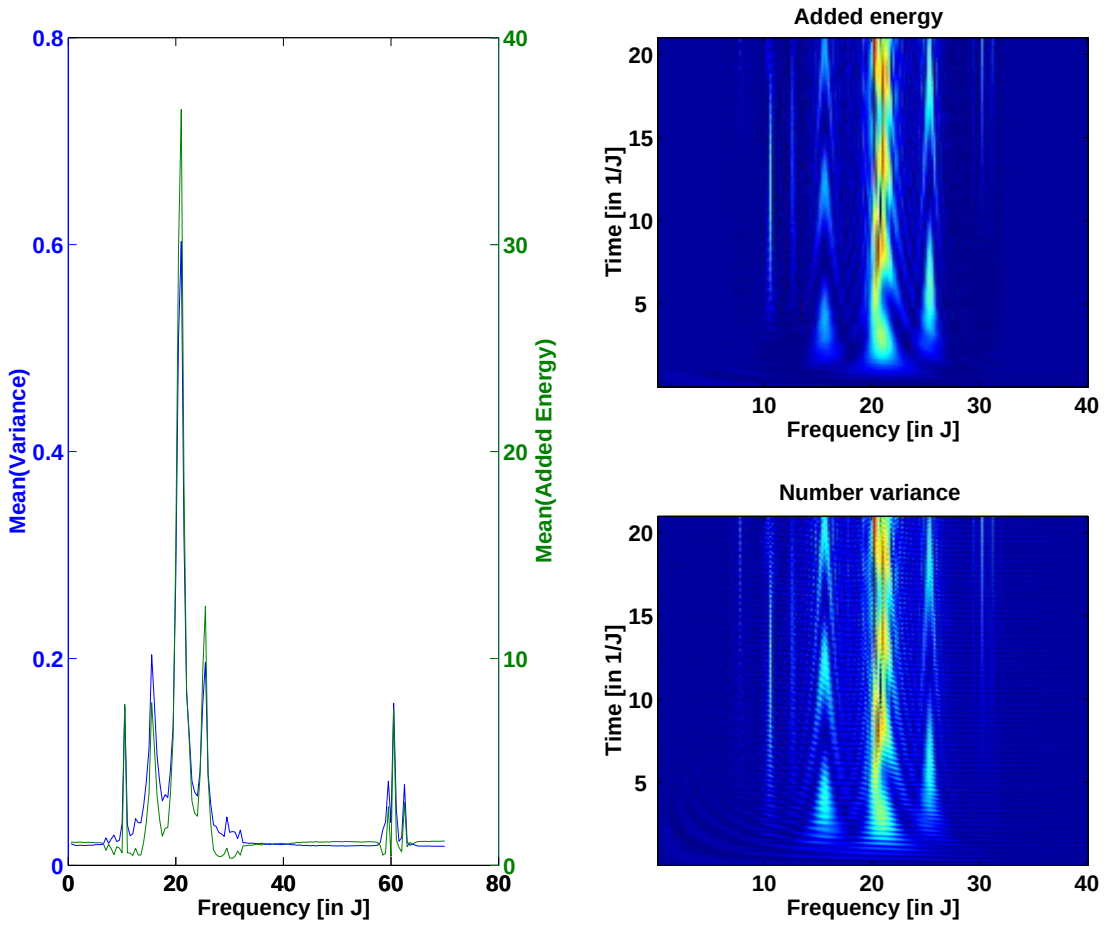

Figure 5.9: The lefthand plot shows the mean values of the added energy and number variance over time for $U/J = 20$ and $N_p = 1, N_s = 6$. Note that the y1-axis and the y2-axis do not use the same scale. The righthand plots show contour plots of the dynamics of the added energy (top) and the number variance (bottom) for the same configuration as in the left plot.

could conceivably be used as an indicator for how close the system is to the phase transition. At the very least, when the numerical dynamics and the interference pattern dynamics agree, the system is certainly not in the SF phase. We will discuss this possibility for future work further in Chapter 7.

We have seen that the location of excitations visible in the number variance (and to some degree in the related observables) mirrors the static energy spectrum closely even for superfluid systems. This is encouraging with respect to the usefulness of the number variance for tracking the phase transition. The important aspect here is not the focus on how the number variance changes with respect to the phase transition, but rather to use the location of the excitations in the number variance as a close picture of the energy spectrum. The energy spectrum, though, effectively

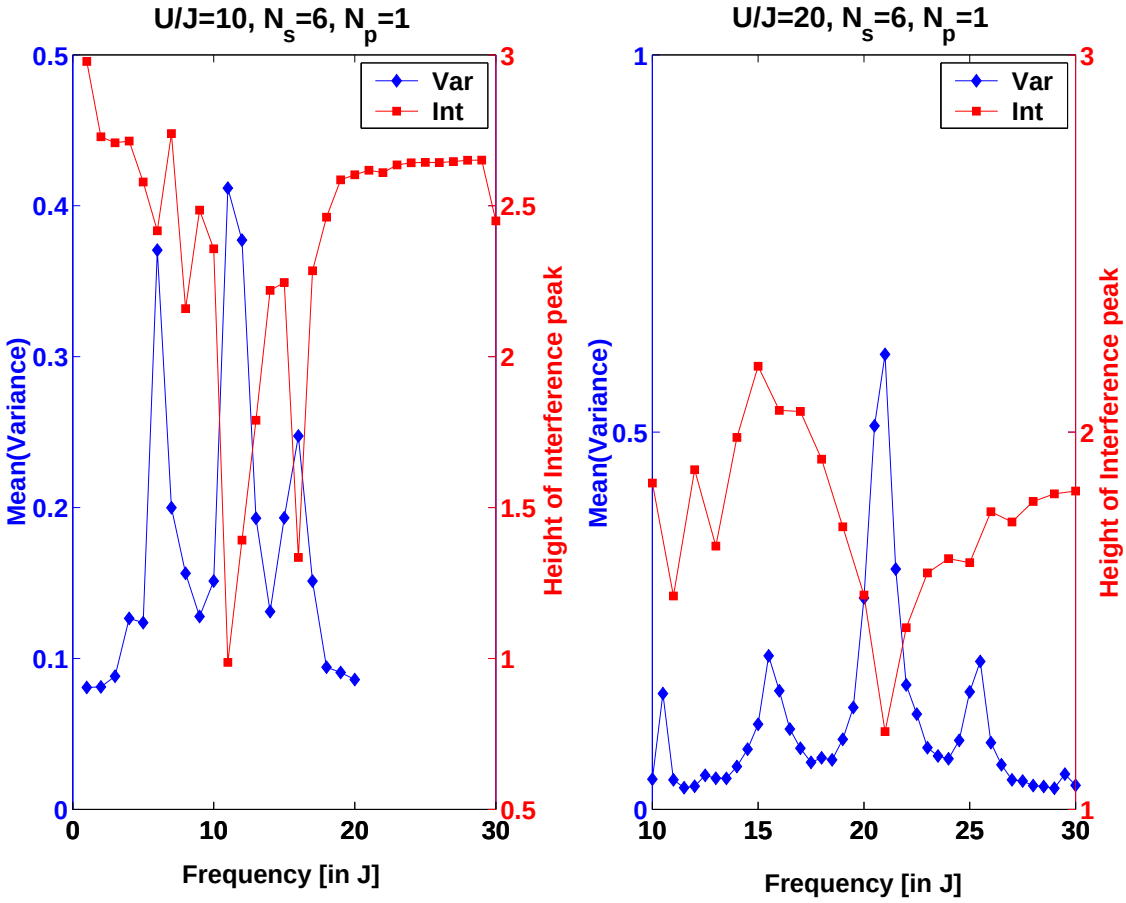

Figure 5.10: The blue diamonds are mean values of the number variance, the red squares show the height of the interference peak. The left plot shows results for $U/J = 10$, $N_s = 6$ and $N_p = 1$, the right plot shows results for $U/J = 20$, $N_s = 6$ and $N_p = 1$.

describes the eigenstates of the system and can thus be used to determine the phase of the system. This approach is really only viable for the precise resonances caused by Bragg spectroscopy. As Fig. 5.11 shows for $U/J = 0.1-10$, a resonance structure remains clearly visible even for $U < J$. This illustrates one of the advantages of Bragg spectroscopy over other methods such as the application of a static force - the resonances at small U/J are no longer obscured by Bloch oscillations and various other effects.

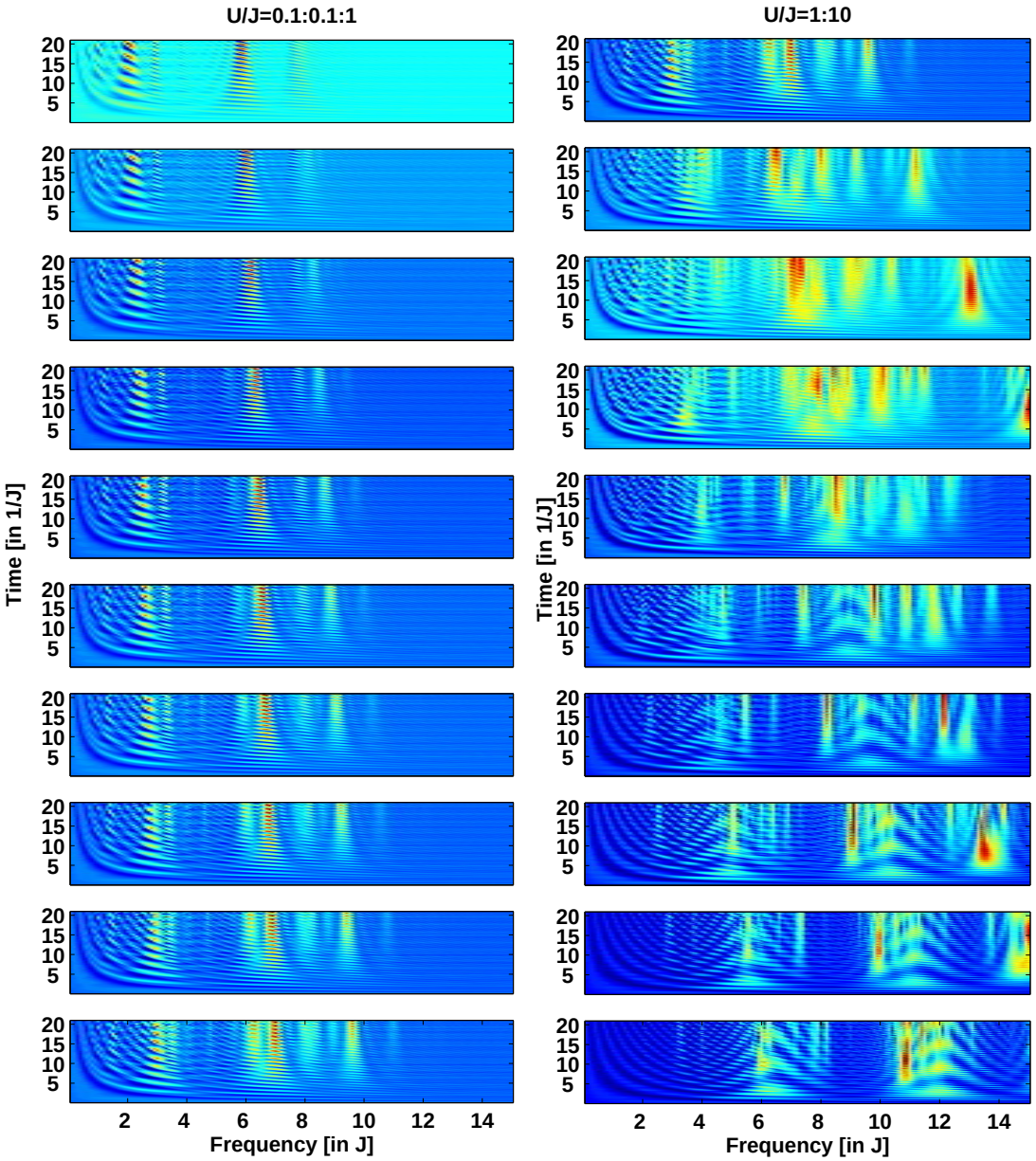

Figure 5.11: From top to bottom: the left plot shows contour plots of the number variance for U/J =0.1, 0.2, 0.3, 0.4, 0.5, 0.6, 0.7, 0.8, 0.9, and 1. The right plot shows contour plots of the number variance for $U/J = 1$, 2, 3, 4, 5, 6, 7, 8, 9, and 10, $N_s = 6$ and $N_p = 1$. The perturbation strength is $\mathcal{F} = 0.1$ in all cases. The oscillatory structure is caused by the time dependency of J and U.

Unfortunately, discerning the entire excitational spectrum and thus the underlying energy structure is far from trivial. Consequently, we will now explore which specific aspects might be useful without needing to consider the details of the entire resonance region.

One possibility is the strength of excitations in the number variance. Progress towards the MI phase appears to be reflected in the ratio of peak to the starting value of the number variance (and energy analogously). As shown in the left plot in Fig. 5.12, peaks at the resonant energy grow progressively more pronounced. This effect is even clearer when comparing it with the base level of the number variance $\mathcal{V}$ for no perturbation as in the right subplot in Fig. 5.12 by plotting

$$\delta_{\text{max,min}} = \frac{\text{Max}(\mathcal{V}) - \text{Min}(\mathcal{V})}{\text{Min}(\mathcal{V})}. \tag{5.22}$$

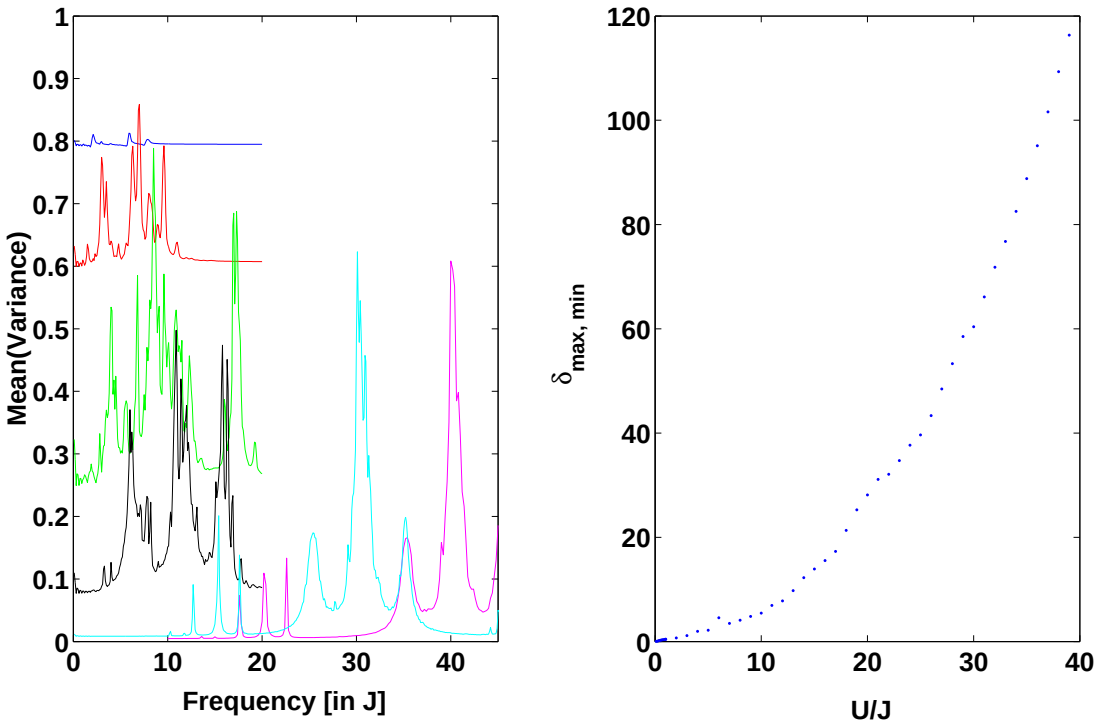

Figure 5.12: The left plot shows the mean value of the number variance for U/J=0.1 - blue, 1 - red, 5 - green, 10 - black, 30 - cyan, 40 - magenta. Noticable is also the shift in the resonance location which is due to the change of energy gaps with shifting U. The right plot shows $\delta_{\text{max,min}}$ for U/J=0.1-40. All values are for $N_s = 6$ and $N_p = 1$.

Another possibility for tracking the progress from superfluid to Mott insulator is via the distance between peaks. The more squeezed the system, the clearer is the 'mirror' of the main resonance of the first band at half the energy, see e.g. Fig.

5.13. This has the added advantage that it should be apparent independent of the exact structure within the band.

5.5 Summary

We have seen that Bragg spectroscopy offers a very precise instrument to study the energy spectrum of a system. We find that resonances in the number variance correspond very well to the static energy structure, indicating that this might be a useful experimental observable. We also find a number of additional effects that could be of use in tracking the phase of the system. Quantifying these variables will be the subject of future work and we shall discuss this further in Chapter 7.

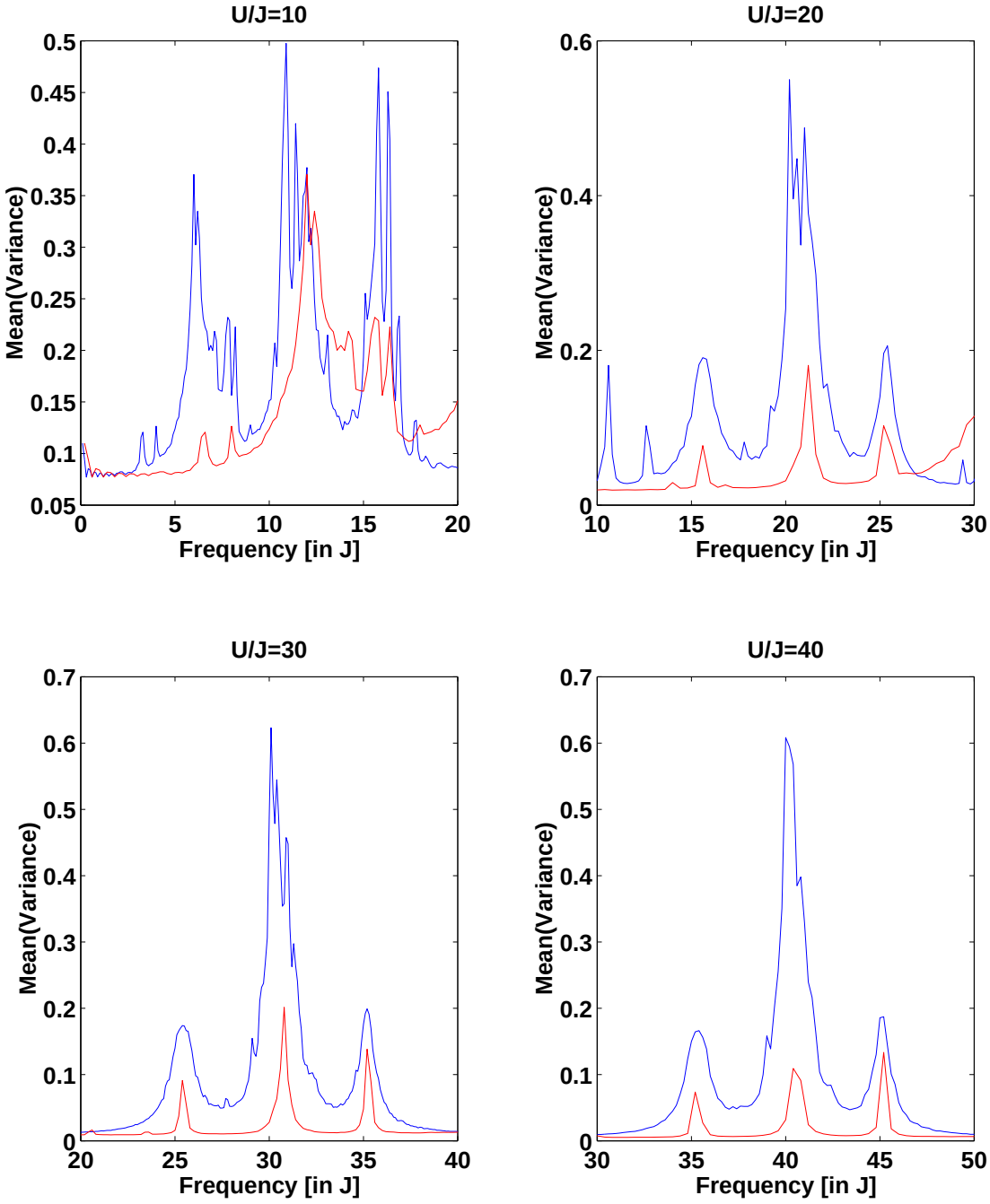

Figure 5.13: In these plots we compare the main resonance at $\omega = U$ with the fractional resonance at $\omega = U/2$. The blue line shows the mean value of the number variance. The red line represents the mean of the variance at half the frequency. Top row: $U/J = 10$ (left) and $U/J = 20$ (right), bottom row: $U/J = 30$ (left) and $U/J = 40$ (right). All values are for $N_s = 6$ and $N_p = 1$.

Chapter 6

Oscillations - Bloch, hopping and beyond

While we were interested in the use of a static field simply as a tool to study the energy gap of a Mott insulator in Chapter 4, the application of this static force can also produce interesting effects in its own right. One of these effects is a rich structure of oscillations over time both in the number variance and in the added energy.

In this chapter, we will first discuss the various theoretical causes for oscillations, then review some of the experimental work done on the subject and finally present our results.

6.1 Theory

The problem of atoms in a periodic field and a static field is closely related to a more general study of particles in a periodic lattice under the influence of a static field. This system has been extensively studied over the last decades [114, 115, 116] in the guise of the Wannier-Stark system. It was shown that these so called Bloch particles can exhibit periodic motion, i.e. Bloch oscillations, with a Bloch period of

$$T_B = 2\pi/dF \tag{6.1}$$

where d is the distance between sites (i.e. the lattice periodicity) and F is the static force in the single particle Wannier-Stark Hamiltonian

$$\widehat{H}_{\mathrm{WS}} = \frac{\hat{p}^2}{2M} + V(x) - Fx, \quad V(x+L) = V(x). \tag{6.2}$$

In experimental settings, the potential $V(x)$ usually takes the form of a periodic cosine wave, i.e. $V(x) = V_0 \cos^2(k_L x)$ where $k_L = 2\pi/d$.

This is a rather counter-intuitive result that was debated for years (see e.g. Ref. [117, 118]) - after all, the classical response to a static force such as gravity does not usually involve oscillations. In order to understand the dynamics, it is helpful to first consider the eigenstates of the system. From an arbitrary eigenstate of H_{WS}, i.e. $H_{\mathrm{WS}}\Psi_0 = E_0\Psi_0$, one can construct a whole ladder of eigenstates with eigenvalues $E_l = E_0 + ldF$ by a translation of Ψ_0 over l periods of the lattice constant d (assuming a simple single-band system). The resulting Wannier-Stark (WS) eigenstates are the resonance states of the system and are collectively know as Wannier-Stark ladders [119]. Any superposition of these WS states then shows oscillatory behaviour with a Bloch period. These oscillations are effectively caused by Bragg scattering. On average, the Bloch particles do follow the static acceleration and travel 'down' the lattice. During that motion along the lattice, they scatter back and forth off the lattice as in standard Bragg theory where we get interference for $n\lambda = 2d\sin\theta$. The calculation of the WS ladder, especially for interacting particles and in higher dimensions, has proven to be non trivial [120, 121, 122]. Part of the reason for this is that, for more than one band, the decay of the WS states has to be taken into account. Again, the exact form of this decay is system dependent, but can be estimated using the formalism of Landau-Zener tunneling [123, 116].

Bloch oscillations can also be studied from an atom optical view point [123]. This includes the assumption that we can think of the eigenstates of the static system as 'particle-like', i.e. tight-binding and non-interacting.

The Schrödinger equation for the single particle Hamiltonian of Eq. (6.2) is given by

$$i\frac{\partial\psi(p,t)}{\partial t} = \left[\frac{(p+Ft)^2}{2M} + \frac{1}{2}\right]\psi(p,t) + \sum_l \Omega_l^*\psi(p+lk_d,t) + \sum_l \Omega_l\psi(p-lk_d,t) \tag{6.3}$$

where the coupling constants Ω_l and Ω_l^* depend on the exact nature of the potential V and $k_L = 2\pi/d$ is the border of the first Brillouin zone.

The analogue to the Wannier-Stark ladder in momentum terms are the discrete states $\psi_n(t) = \psi(p_0 + nk_d, t)$ where $n\,\epsilon \pm \mathbb{N}_0$. The dynamic equation for these discrete states is

$$i\frac{\partial}{\partial t}\begin{pmatrix} \vdots \\ \psi_1 \\ \psi_0 \\ \psi_{-1} \\ \psi_{-2} \\ \vdots \end{pmatrix} = \begin{pmatrix} & \vdots & & & \vdots & \\ \dots & \epsilon_1 & \Omega_1 & \Omega_2 & \Omega_3 & \dots \\ & \Omega_1^* & \epsilon_0 & \Omega_1 & \Omega_2 & \\ & \Omega_2^* & \Omega_1^* & \epsilon_{-1} & \Omega_1 & \\ \dots & \Omega_3^* & \Omega_2^* & \Omega_1^* & \epsilon_{-2} & \dots \\ & \vdots & & & \vdots & \end{pmatrix} \begin{pmatrix} \vdots \\ \psi_1 \\ \psi_0 \\ \psi_{-1} \\ \psi_{-2} \\ \vdots \end{pmatrix} \tag{6.4}$$

where $\epsilon_n := (p_0 + nk_d + Ft)^2/(2M) + \alpha_0/(2)$. Any two ladder states ψ_n, ψ_{n+l} are then coupled by the 2×2 matrix

$$\begin{pmatrix} i\frac{\partial \psi_n}{\partial t} \\ i\frac{\partial \psi_{n+l}}{\partial t} \end{pmatrix} = \begin{pmatrix} \epsilon_n & \Omega_l \\ \Omega_l^* & \epsilon_{n+l} \end{pmatrix} \begin{pmatrix} \psi_n \\ \psi_{n+l} \end{pmatrix}. \tag{6.5}$$

Resonances between states n and $n + l$ occur at a time t_n where the difference between the diagonal elements is small, i.e. for

$$\epsilon_{n+l} - \epsilon_n = \frac{lk_0}{M}\left(\frac{1}{2}(2n + l)k_d + p_0 + Ft\right) \to 0. \tag{6.6}$$

In other words, we expect a transition when the initial momentum p_0 has changed to a multiple of $k_d/2$, i.e.

$$p_0 + Ft = -k_0(n + l/2) \tag{6.7}$$

which brings us back to the condition of Bragg scattering discussed earlier. This resonance condition is equivalent to the kinetic energy of the particle, $p^2/2M$, being equal to the spacing between the discrete ladder states. As suggested by [123], we assume that at the time $t_{n,n+l}$ for which $\epsilon_n - \epsilon_{n+l} \to 0$ all off-diagonal matrix elements other than Ω_l are suppressed.

For a Landau-Zener transition, the probability that a particle will stay in its initial state is approximately [123]

$$P_{\text{stay}}(l) = \exp\left(-\pi\frac{|\Omega_l|^2}{|lk_dF/m|}\right) \tag{6.8}$$

The probabilities for various transitions thus depend on the matrix elements Ω_l. For a sinusoidal potential and in the non-interacting approximation, we should only find the simple Bloch oscillation occurring between ψ_0 and ψ_1 with a period of $t_B = 2\pi/Fd$. For a more complex potential and/or for non-zero interactions, however, there are some $\Omega_l \neq 0$ for $l \neq 0$ so that higher order Bloch oscillations may occur.

In the specific case of optical lattices in the Mott regime, neither the Wannier-Stark picture nor the atom optical approach alone are sufficient as these are single particle models. The effect of interactions on Bloch oscillations has been studied in [124]. The author finds that there is an additional period with

$$T_{\text{add}} = 2\pi/U. \tag{6.9}$$

This result is only valid for a strong-field condition as the derivation makes the assumption that the system is sufficiently squeezed that Fock states can be used as eigenstates of the system. The exact dependency on the interaction, including weak values, is complex and not yet clearly understood [122]. One approach [94] is to study the quasi energy spectrum of the interacting Hamiltonian including the static field, analogous to the study of WS resonances. The author of that paper finds that the quasi energy states in a restricted basis, and with these the periodicity of oscillations, depend on the detuning of interaction with respect to the static force $\lambda = (U - dF)/J$. These oscillations are on a much longer time scale than the 'normal' Bloch oscillations. We will see that we find periodicities that also depend on the detuning λ of the system from resonances. As [94] does not further quantify the dependence of their results, further comparisons are difficult to make.

We interpret these detuning resonances as follows. Bloch oscillations are caused by the dynamical evolution of ground state particles along the lattice where the ground state is close to the $|111\ldots1\rangle$ Fock state. At the resonances, the system can reach a state where it is predominantly in the Fock eigenstate of the tilted system. Once a large part of the system is in the tilted ground state, however, we should find additional Bloch oscillations with a periodicity of

$$T_{\text{res}} = 2\pi/|Fd - E_{\text{resonance}}|. \tag{6.10}$$

These oscillations should give us an idea of the exact location of resonances as well as the strength of the resonances when compared to the original Bloch oscillations. For ease of distinction, we will refer to the Bloch oscillations with a detuned peri-

odicity as resonance Bloch oscillations and call the normal Bloch oscillations origin Bloch oscillations.

In the superfluid phase, i.e. for a very weak lattice, the system is more akin to one large condensate. Consequently, we expect to find either oscillations at the tunneling frequency or collective oscillations caused by exciting the system. These oscillations can take a variety of forms and are highly dependent on the exact system characteristics [106, 109, 111, 125, 126, 127].

6.2 Experiment

Bloch oscillations have been observed in a wide range of experimental conditions - their first realization was in semiconductor superlattices [128]. In optical lattices, Bloch oscillations (and the corresponding Wannier-Stark ladders) were first observed under the influence of gravity [129, 130]. Later experiments created a static force in the optical lattice configuration by using a tunable frequency difference between the two (or more) counterpropagating waves that form the standing laser wave [131].

This frequency difference is created by an upshift of the left laser wave (with wavelength λ) by $\delta\nu$ and a downshift of the right laser wave by an equal amount. The two waves are then Doppler shifted into the same frequency when regarded in a reference frame moving to the right at a velocity $v = \lambda\delta\nu$. The periodic potential is constant in this frame. A linear increase of $\delta\nu$ over time t_a from 0 to δ_{final} then produces an uniformly accelerated potential with an acceleration proportional to $\mathrm{d}(\delta\nu)/d\mathrm{t} = \text{const}$ during time t_a [132].

The reason for the large time lag between the theoretical conception of Bloch oscillations in 1928 [133] to their experimental realization in 1992 [128] lies in the dependency of the Bloch period on the force F and the lattice constant d with $T_B = 2\pi/dF$. In the solid-state electron systems for which the problem was initially formulated, forces strong enough that the Bloch time was smaller than the relaxation time caused significant scattering by impurities, electron-phonon and phonon-phonon interactions so that Bloch oscillations were no longer observable. Semiconductor superlattices that were fabricated by epitaxial growth of GaAs and GaAlAs, in contrast, had periodic potentials whose period d was two orders of magnitude larger than those of bulk semiconductors so that it was possible for the Bloch time, thus reduced by two orders of magnitude, to be smaller than the relaxation time.

Part of the attraction of using optical lattices to find Bloch oscillations was the absence of disturbances by scattering of phonons or lattice impurities, excitonic effects and more. Another advantage is the ease of tuning the acceleration to specific values. A common experimental procedure [130, 59] uses an adiabatic switch-on of the static optical lattices after the atoms have been cooled (e.g. by stimulated Raman cooling). This adiabaticity has the advantage of transfering the initial momentum spread into a spread of the lattice quasi-momentum. The optical potential is then accelerated over a time t_a. Both the acceleration and the standing optical potential are finally switched off abruptly so that a measurement of the atomic momentum distribution of the free atoms can be taken as instantaneously as possible. Comparing the atomic momentum distribution for a range of acceleration times t_a then shows the oscillating wave packets.

6.3 Numerics

As in Chapter 4, we take the eigenstates of the BHM Hamiltonian (Eq. (2.17)) (calculated by exact diagonalization of the static Hamiltonian) as our initial states and then instantly switch on the perturbation so that the dynamic Hamiltonian is

$$H_{\text{dyn.}} = -J \sum_{\langle i,j \rangle} \hat{a}_i^\dagger \hat{a}_j + \sum_i \epsilon_i \hat{a}_i^\dagger \hat{a}_i + \frac{1}{2} U \sum_i \hat{a}_i^\dagger \hat{a}_i^\dagger \hat{a}_i \hat{a}_i \tag{6.11}$$

where $\epsilon_i = (W - i)U$, i.e. $\epsilon_1 = (W-1)U$, $\epsilon_2 = (W-2)U$ and $\epsilon_W = 0U$. We then solve the Hamiltonian exactly using a fifth order Runge-Kutta approach [87]. While experimental setups usually study the change in the momentum distribution, we will focus on the number variance. We will find that it corresponds well both to the energy added to the system and to the changes in the momentum distribution (in the form of the interference pattern). In contrast to the interference pattern, it is significantly more efficient to calculate numerically due to its locality.

The wave function resulting from the dynamical approach is sampled at regular time intervals (typically with an interval length of $0.0001/J$). The number variance $\mathcal{V}$ is then calculated from this wave function ($\mathcal{V} = \langle(\hat{n}_i)^2\rangle - \langle\hat{n}_i\rangle^2$ where $\hat{n}_i$ is the number operator for site i.)

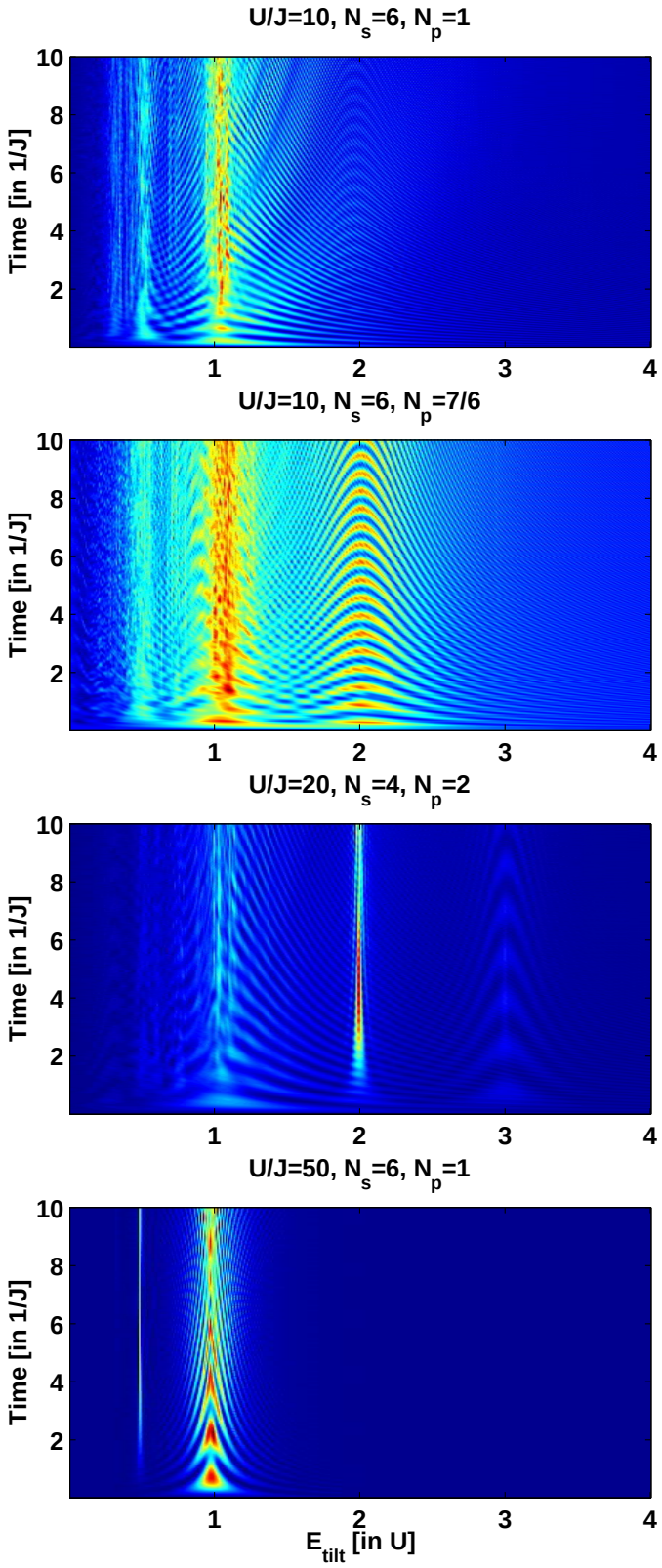

Figure 6.1: These plots show the dynamics of the number variance for a range of values for U/J, N_s and N_p. Top plot: $U/J = 10$, $N_s = 6$ and $N_p = 1$, second plot: $U/J = 10$, $N_s = 6$, $N_p = 7/6$, third plot: $U/J = 20$, $N_s = 4$, $N_p = 2$, bottom plot: $U/J = 50$, $N_s = 6$, $N_p = 1$.

The resulting dynamics of number variance, energy (and interference pattern, for comparison purposes) show clear oscillatory structures as can be seen in Fig. 6.1 for the number variance. For a comparison between number variance and added energy, see Figs. 4.9, 4.10, 6.2 and 6.3. In order to be able to interpret these oscillations, we use a fast fourier transformation - the fft routine of Matlab 6.1 - to extract the oscillation frequencies from the number variance.

6.4 Results

A plot of the dynamics of a very superfluid system with $U = 0.001$ and $J = 1$ (see Fig. 6.2) shows a very small response with the periodicity of the tunneling time, $\tau_J = 2\pi/J$. Fourier analysis for the number variance gives integer multiples of the tunneling frequency $\nu_J = 1/\tau_J$. As expected, the strength of the response depends on the strength of the perturbation and does not show any evidence of an energy gap. Instead, there is a gradual increase with increased force. The lack of Bloch oscillations is due to our choice of system parameters. As the interaction constant U depends on the lattice height, a very small value for U will imply a very shallow lattice. For a deep lattice with vanishing s-wave scattering length a_s, however, we would expect to see Bloch oscillations similar to those of Bloch electrons in crystals. In this thesis, we will focus on more strongly interacting systems.

Even a very moderate amount of squeezing, e.g. $U/J = 1$, causes a drastic change (see Fig. 6.2). Instead of the smooth oscillations for the very superfluid system with $U = 0.001, J = 1$, we now find a dependency on the force that is related to the eigenvalue spectrum (see e.g. Fig. 4.3) and clear Bloch oscillations with the Bloch period of approximately $2\pi/dF$, see Fig. 6.3.

Interestingly, we also find signs of oscillations at $2\nu_B$. This is likely due to the fact that the system is still only very moderately squeezed. The transition probability between ladder states is thus relatively high so that higher order Bloch oscillations are viable. These Bloch oscillations at $2\nu_B$ and higher frequencies are probably a sign of oscillating between sites that are not immediate neighbours, analogous to the hopping we saw in Chapter 2. It is instructive to think of non-adjacent lattice sites as lattices with a larger lattice constant. For example, we consider next nearest neighbour hopping for a lattice with lattice constant $2d$. The concomitant Bloch oscillations clearly occur at $\nu'_B = Fd'/2\pi = Fd/\pi = 2\nu_B$. The lattice site at $d'/2 = d$ can then be treated as a perturbation that has the effect of reducing the tunneling probability between sites at x and at $x + d'$.

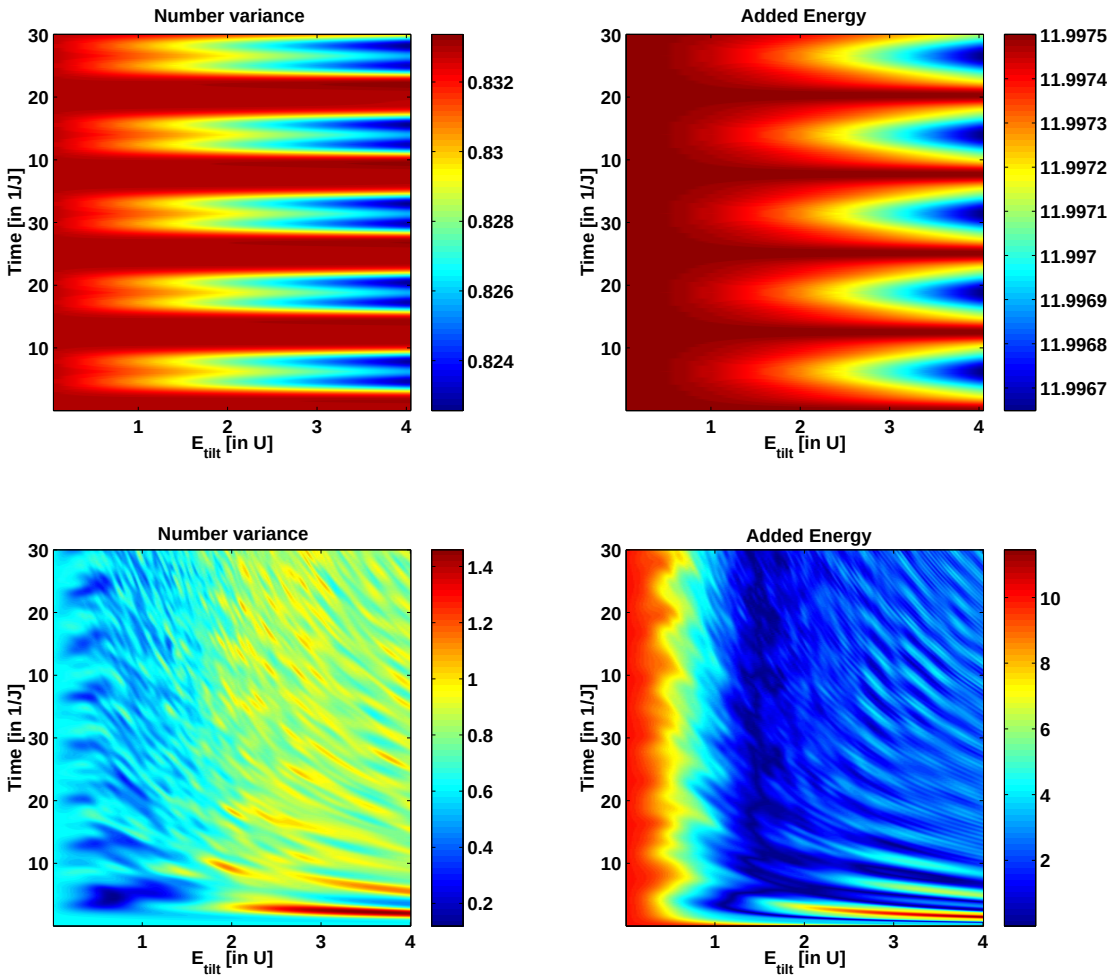

Figure 6.2: The top plots show the dynamics of the number variance and the added energy for $U/J = 0.001$. The bottom plots show number variance and added energy for $U/J = 1$. All values are calculated for $N_s = 6$ and $N_p = 1$.

The 'normal' Bloch oscillations are far stronger than the higher order ones, however. Interestingly, we also find a dependence of the strength of the Bloch oscillations on the strength of the excitations in the number variance. This can be understood by taking into account that the Bloch oscillations are really a phenomenon of a non-interacting system such as the original Bloch electrons in crystals which could successfully be described in a single-particle model. With the increase of localizing interactions, tunneling is increasingly less likely and Bloch oscillations are weak. We will see that this weakening of the oscillations is still visible when increasing the ratio U/J, see e.g. Fig. 6.5 where the Bloch oscillation has all but disappeared for $U/J = 20$. When the number variance shows excitations, however, that implies that atoms are less localized and thus more likely to Bloch oscillate.

In other words, the strength of the Bloch oscillation is also an indicator of the strength of the change in the number variance. A closer study of the frequencies

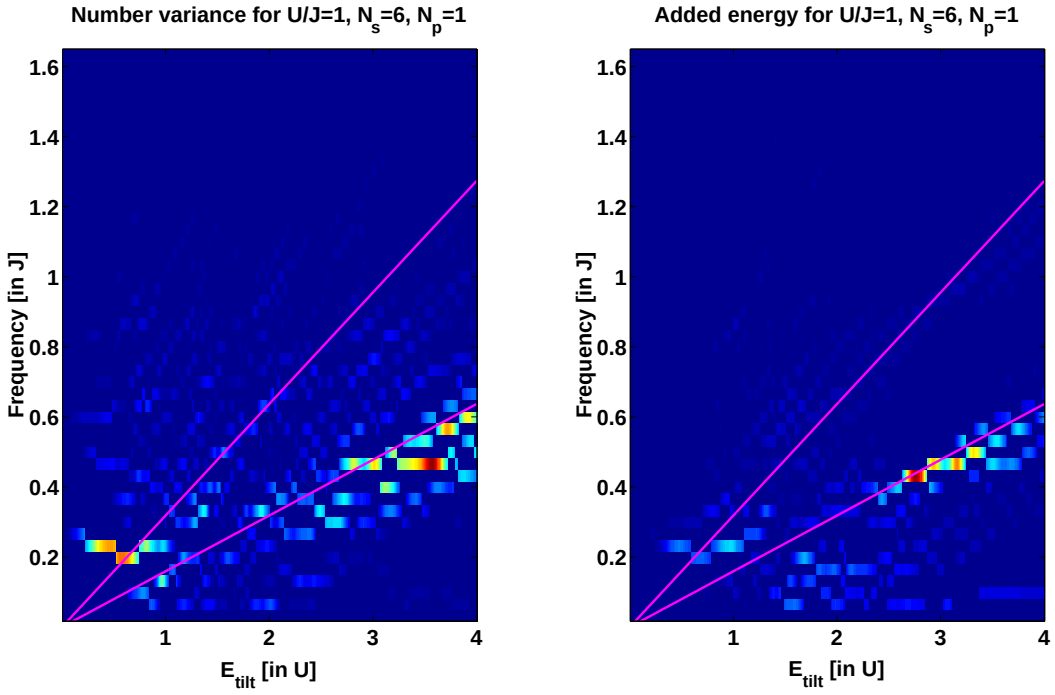

Figure 6.3: These plots show the oscillation frequencies of the number variance (left) and added energy (right) for $U/J = 1$ and $N_p = 1, N_s = 6$. The magenta lines represent Bloch oscillations at the frequencies ν_B and $2\nu_B$.

for a squeezed system (e.g. $U/J = 20$, see Fig. 6.4) shows a number of additional features to the Bloch oscillation ν_B. As we can see in the left plot of Fig. 6.4, the predicted additional frequencies $\nu_{\text{int}} = \frac{U}{2\pi}$ of [124] are indeed visible (red lines). We also find multiples of ν_{int}, i.e. $2\nu_{\text{int}}$ and $3\nu_{\text{int}}$. Of special interest here, though, are the resonance Bloch oscillation frequencies that we discussed earlier. These oscillations appear to be dependent on the detuning δ of the applied force from a resonance. For example, for the resonance at U, we find a dependency on $\delta = |(E_{\text{tilt}} - U)|$. These oscillations have the same slope as the Bloch oscillation originating from $0U$, i.e. $\nu_{\text{res}} = (Fd - U)/(2\pi)$. Both resonance and origin oscillations are traced in the right-hand plot with white lines. One possible interpretation of these resonance Bloch oscillations is to consider them in terms of origin Bloch oscillations of the tilted lattice. The symmetry of these oscillations around their point of origin is in good accordance with this possibility. In this interpretation, we assume that the resonance excitation is strong enough that the eigenstates of the tilted lattice are populated significantly.

Similar to our results for the Bloch oscillations for $U/J = 1$ (Fig. 6.3), we again see higher order oscillations at double the frequency, i.e. $\nu'_B = 2\nu_B$. This is true even for the non-origin frequencies. This can be understood by using the Bragg reflection interpretation. According to the Bragg criterion, reflection is possible precisely then when the distance between reflection points is an integer multiple of the wavelength.

It is also interesting to note that, in contrast to $U/J = 1$, the origin Bloch oscillation is no longer the strongest frequency in the system. Instead, as we predicted earlier, the resonance Bloch oscillation for $E_{\text{tilt}} = U$ grows progressively stronger in contrast to the other effects with the increase of U/J. Fig. 6.5 shows this for $U/J = 1$ and $U/J = 20$.

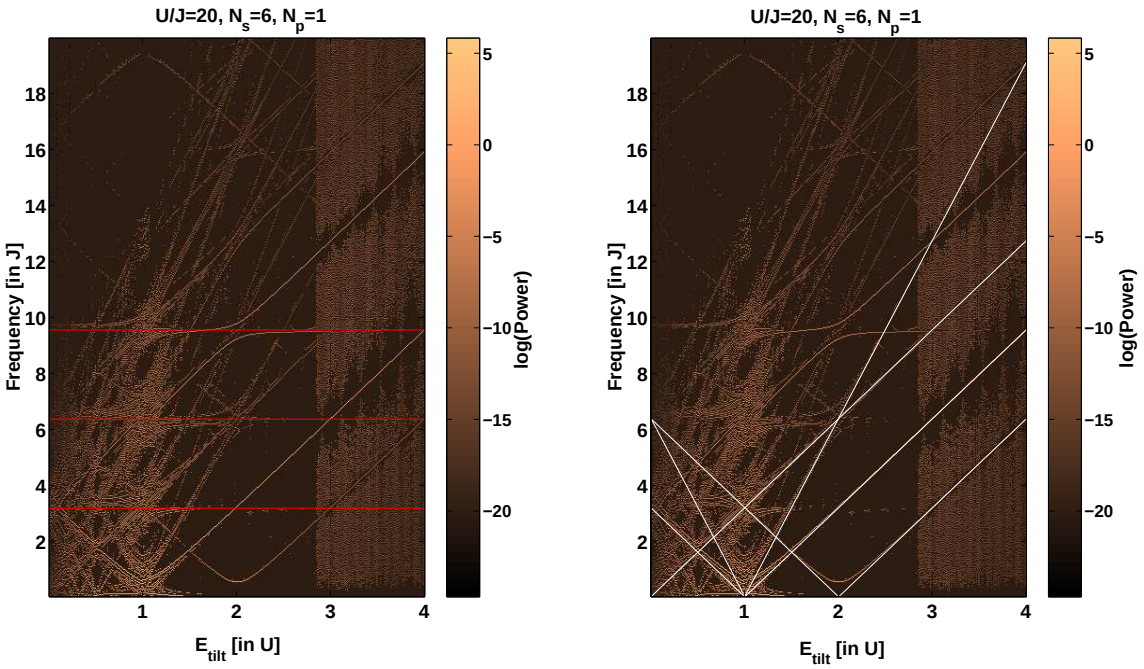

Figure 6.4: Both plots show a contour plot of the fft spectrum for the dynamics of the number variance over time for $U/J = 20$, $N_s = 6$ and $N_p = 1$. In the left plot, interaction frequencies ($\nu = U/2\pi$) are drawn in red lines. In the right plot, origin and Bloch oscillations are shown in white lines. Note that the spectrum strength is depicted on a log scale.

So far, we have discussed results for integer filling (i.e. $N_p \in \mathbb{N}$). Even though the energy eigenspectrum changes for non-integer filling, the oscillations we observe fall in the same categories as those already discussed above: there is the interaction frequency $\nu_{\text{int}} = \frac{U}{2\pi}$, the origin Bloch frequency ν_B and the resonance Bloch frequency $\nu_{B,\text{res}}$. Frequencies for non-integer filling differ in the relative importance of oscillations, though. This is a direct consequence of the results we found in

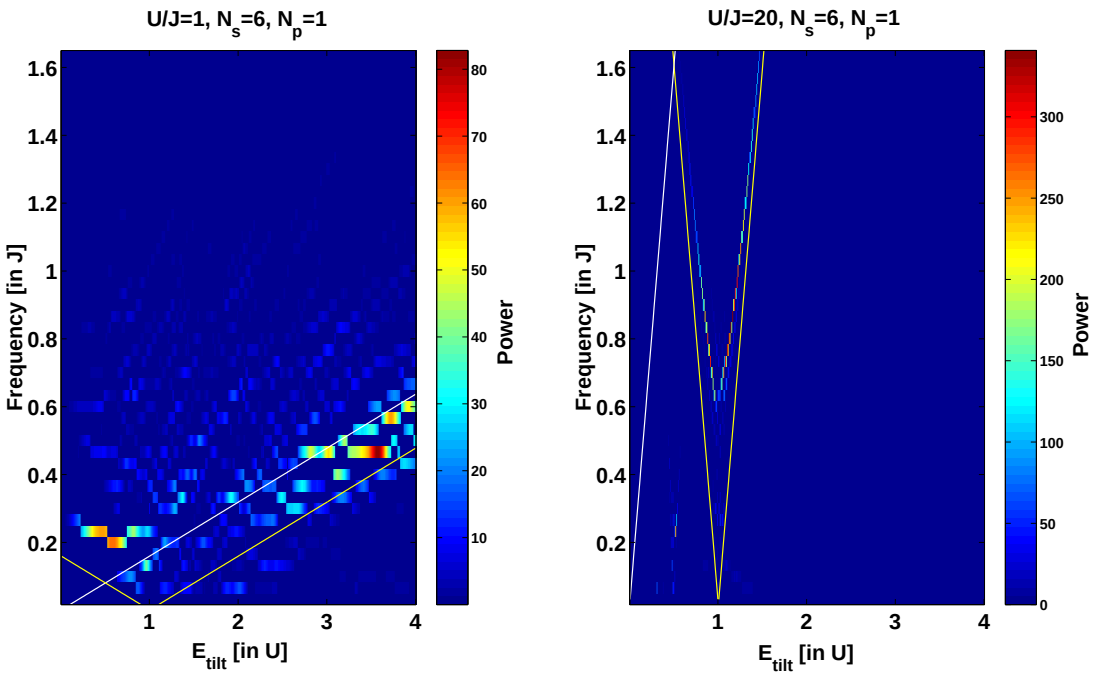

Figure 6.5: These plots show the frequency spectrum for $U/J = 1$ (left plot) and $U/J = 20$ (right plot) for $N_p = 1$ and $N_s = 6$. Origin Bloch oscillations are marked with white lines, resonance oscillations with yellow lines.

Chapter 4 (see e.g. Fig. 4.6): due to the 'extra' atoms, higher order processes, e.g. hopping at the resonance $E_{\text{tilt}} = 2U$ become much more likely. Consequently, the Bloch oscillations of those resonances play a more prominent role in the Fourier analysis spectrum.

The greater strength of resonance Bloch oscillations also allows us to distinguish between the various contributions at $E_{\text{tilt}} \approx U$ from the energy band. In an infinite lattice, the energy values for states in one band are degenerate - i.e. Bloch oscillations should occur at exactly $E_{\text{tilt}} = U$. In a finite lattice, however, the band will have a finite non-zero width. For example, for an applied energy difference between sites $E_{\text{tilt}} \approx U$, resonance excitations could involve the creation of particle-hole pairs at site 5 and 6, i.e. $|111102\ldots\rangle$ as well as particle-hole pairs at 1 and 2, 3 and 4 and 5 and 6 ($|020202\rangle$). Due to the finite lattice size which is expressed in a finite band width, these have different energies and resonances thus occur for slightly different E_{tilt}. The spread of resonant frequencies around, for example, $E_{\text{tilt}} = U$ can then be used as an indicator on the band width.

We found in Chapter 4 that non-integer filling for finite systems has somewhat different features to those predicted by the infinite lattice phase diagram as in Fig.

3.1. In an infinite lattice, the non-compressibility of the MI phase implies that a non-integer filling will lead to a superfluid ground state. Finite systems, however, are characterized by a gradual phase transition rather than a sharp switch between SF phase and MI phase. Consequently, there can be states with simultaneous off-diagonal and diagonal long range order that show MI characteristics such as evidence of an energy gap, but are no longer non-compressible and also possess SF characteristics.

These SF phase characteristics can manifest themselves in the relative strength of origin Bloch oscillations to the resonance Bloch oscillations at multiples of the interaction energy U. This can be understood by reminding oneself of the fact that the origin Bloch oscillations were originally a phenomenon of electrons in a crystal that could approximately be treated as a non-interacting system. The eigenstates of these so-called Bloch electrons are delocalized across the entire lattice. In an optical lattice, this is equivalent to the SF phase where bosons are delocalized across the lattice. The resonance Bloch oscillations at $E_{\text{tilt}} \approx nU$ are solely an MI phenomenon as they imply that there is an energy gap caused by the (repulsive) interactions of the bosons. Consequently, we should find that the ratio of the strength of origin Bloch oscillations to resonance Bloch oscillations grows larger as we approach the phase transition. For the SF phase, resonance Bloch oscillations should have vanished entirely.

Our results support this argument. We find that a comparison of the frequency spectrum for $U/J = 1$ and $U/J = 20$ (see Fig. 6.5) shows a clear change in the prominence of origin Bloch oscillations and resonance Bloch oscillations.

Fig. 6.6 also shows results that agree well with this theory. For a dependence of the ratio of resonance to origin Bloch oscillations on the phase of the system, this makes sense as adding a non-integer filling is analogous to lowering U/J save that we find the same U dependent oscillations. In other words, finding the same effect for changing U/J as for changing N_p is a strong indication that this ratio is indeed dependent on the phase of the system.

6.5 Summary

We have been able to confirm Bloch oscillations with the Bloch frequency $\nu_B = dF/(2\pi)$ as well as oscillations with frequency $\nu_{\text{int}} = U/(2\pi)$. In addition to this, we find so-called resonance Bloch oscillations with frequencies that appear to be dependent on the detuning from a resonant force. We give a possible interpretation

of this effect and note that the relative strength of original Bloch oscillations to resonance Bloch oscillations could be useful as an indicator of the phase of the system.

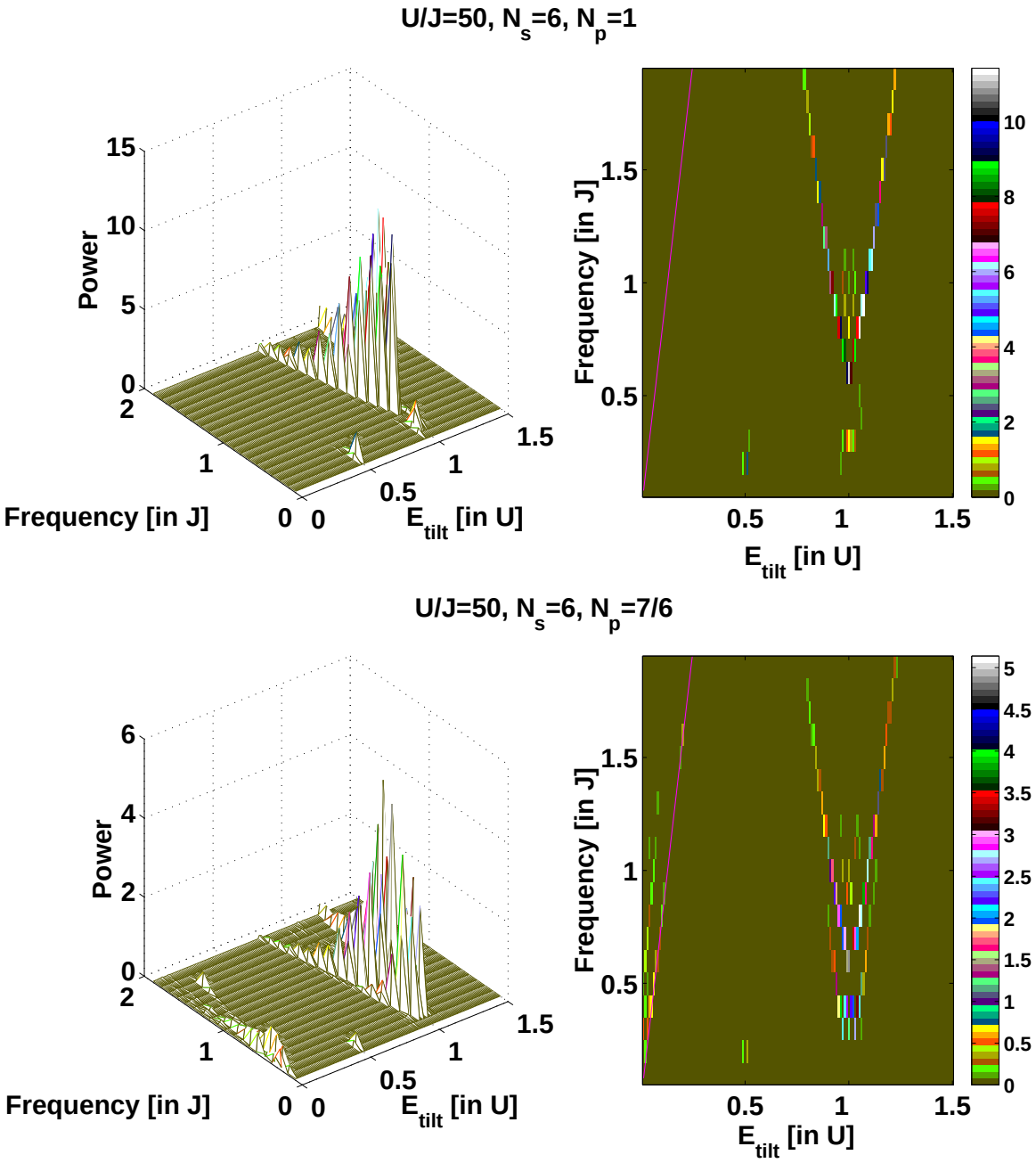

Figure 6.6: The left two plots show the frequency spectrum for $N_s = 6, N_p = 1$ and $U/J = 10$ (top) and $N_s = 6, N_p = 7/6$ and $U/J = 10$ (bottom). The right two plots show the same values in a contour plot. The magenta line indicates the origin Bloch oscillation.

Chapter 7

Possible directions for future work

In this chapter we will discuss prospects for future work and draw some final conclusions with regard to this thesis.

7.1 Comparison of local and global variables

One of the challenges in detecting the SF-MI phase transition is the appropriate choice of observable. It seems that none of the currently used experimental methods can accurately pinpoint the area of transition due to various limitations. The main characteristic of the phase transition is the change from delocalization (SF) to localization (MI). It might therefore be profitable to explore the relationship between the number variance (local variable) and the phase coherence (global variable) further. We are especially interested in the possibility of studying the phase transition by tracking the relation between both variables. In principle, agreement should be best in the transition phase where the system shows both SF and MI characteristics simultaneously. At the same time, depending on the trapping potential, it has been suggested that no global phases will form at all, but that we see domains of MI phases, SF phases and mixed phases. As the number variance is a local variable, its dynamics are dependent on the scale of the excitations. We thus feel that the dynamic excitational spectrum of the number variance could provide us with an idea of the extent of the domains.

We would like to use a variety of approaches. For one, we are interested in studying a numerical model where small clusters are linked by some defined crossing between them. This would entail adding the possibility of loss to the system conditions. One idea might be to use a mixture of mean-field and exact modelling so that any cluster 'sees' a mean-field basin into which losses take place. The dynamics inside the cluster, though, would be treated with an exact model as in this thesis.

An alternative approach might be to explore further simulation methods such as the time-dependent density-matrix renormalization-group technique [134]. This method incorporates a block-decimation technique while still retaining entanglement between blocks (dependent on the dimension) and could consequently be ideal to study the patterned lattice that we are interested in.

Thirdly, there has been some work done on the possibility of a reduction of the lattice basis to lower computational cost of exact calculations. We would like to explore whether a basis could be dynamically adopted to system parameters.

7.2 Dynamic excitations

In Chapter 5, we found that there are particular states for which resonance excitation was possible. We suggest that it might be worth taking the idea of the symmetries and anti-symmetries in the number state basis further and use this to gain a better understanding of the nature of the excitational spectrum. This is motivated by the fact that when the wave function is likely to be in the evenly distributed state $|n \dots n\rangle$ where $n = N_p$, it has a high probability of being in the MI phase. In the delocalized SF phase, in contrast, we expect to find the wave function spread out over the number state basis, i.e. the occurrence of antisymmetric coefficients in the ground state and relevant excited states rises significantly. With antisymmetric coefficients, we refer to the wave function amplitudes of states that are the same apart from permutation (such as $|20\dots\rangle$ and $|02\dots\rangle$) and thus have identical probability p, but whose values in the wave function have opposite signs, i.e. $-\sqrt{p}$ and $\sqrt{p}$. In other words, when the wave function can be written as $\psi = \sum_i \mathcal{C}_i\psi_i$, $\mathcal{C}_i$ is either equal to $\mathcal{C}_j$ or equal to $-\mathcal{C}_j$ when ψ_i and ψ_j are similar apart from permutation.

This anti-symmetry can obviously not occur for the Fock state $|n \dots n\rangle$. Consequently, as the overlap between states does depend on symmetry or anti-symmetry (as we showed for two wells in Chapter 5), the makeup of the ground state with

respect to localization or delocalization should be reflected in the excitational spectrum and we feel that the extent of this connection might be interesting.

7.3 Understanding the behaviour of resonance Bloch oscillations

We have found resonance Bloch oscillations that are dependent on the validity of a localized MI phase state. We would like to explore their sensitivity to the phase transition more extensively. This could also entail further study of their characteristics close to the resonance as we find evidence of deviation from the linear Bloch oscillation slope there.

7.4 Extensions of the Bose-Hubbard model

We are also interested in what would happen if we relaxed some of the fundamental assumptions on which the theory of MI - SF phase transitions in optical lattices is based. The Bose-Hubbard model on which we have based all of the work in this thesis incorporates a number of important approximations. One of them is the limitation of interaction to on-site, zero-range scattering. With the possibility of tuning interaction coefficients to a wide range experimentally by exploiting Feshbach resonances [135], it might be very interesting to look at a modified BHM where the interaction range is assumed to be of the order of the lattice constant. This should dramatically change some of the most characteristic properties of the BHM.

7.5 Concluding remarks - main findings of the thesis

In this thesis, we have used an exact model to study the dynamics of various observables around the SF-MI phase transition. We have found that the number variance is a very good indicator of system dynamics in the MI phase and leading up to the phase transition and suggest that it could well be of use experimentally, especially in conjunction with the observation of global observables such as the interference pattern.

We have found a number of new effects that are indicative of the system phase. In particular, we see resonances at fractions of the expected values in the particle-hole picture for both static and dynamic excitations. These fractions are of special interest, because we may be able to use them to study relative values of experimental observables, e.g. the ratio of the main resonance peak at U to a peak at $U/2$. Potentially of most significance is the observation of Bloch oscillations for the resonance energies. In consequence, they could serve as a direct indicator of the energy spectrum. This is especially interesting as they are not a local effect and can occur for delocalized states as well. That means that the onset of resonance Bloch oscillations should be a sensitive measure of the phase transition.

Appendix A

Runge-Kutta numerical approximation

The Runge-Kutta (RK) method is based on the Euler method in which small increments are added to a function corresponding to derivatives (i.e. right-hand sides of the equations) multiplied by stepsizes. When solving a differential equation by use of an RK method, one then propagates the solution by making a number of Euler-style steps and then using the information obtained to match a Taylor series expansion up to some higher order. Further details of this method can be found in [87].

For the numerical simulations carried out for the work in this thesis, we have made use of the fifth-order RK method. The fifth order corresponds to the number of Euler-style steps carried out within the routing. Thus, if the time derivative of our wavefunction ψ is given by

$$i\frac{\partial\psi(t)}{\partial t} = \widehat{H}\psi, \tag{A.1}$$

the propagation from t to $t + \delta t$ is carried out by calculating [87]

$$k1 = -idt\,\widehat{H}\psi \tag{A.2}$$

$$k2 = -idt\,\widehat{H}(\psi + 0.2k1) \tag{A.3}$$

$$k3 = -idt\,\widehat{H}(\psi + \frac{9}{40}k2 + \frac{3}{40}k1) \tag{A.4}$$

$$k4 = -idt\,\widehat{H}(\psi + \frac{6}{5}k3 - \frac{9}{10}k2 + \frac{3}{10}k1) \tag{A.5}$$

$$k5 = -idt\,\widehat{H}(\psi + \frac{35}{27}k4 - \frac{70}{27}k3 + \frac{5}{2}k2 - \frac{11}{54}k1) \quad (A.6)$$

$$k6 = -idt\,\widehat{H}(\psi + \frac{253}{4096}k5 + \frac{44275}{110592}k4 + \frac{575}{13824}k3 + \frac{175}{512}k2 + \frac{1631}{55296}k1) \quad (A.7)$$

$$\psi(t + dt\,) = \psi + \frac{37}{378}k1 + 0k2 + \frac{250}{621}k3 + \frac{125}{594}k4 + \frac{512}{1771}k6, \quad (A.8)$$

where dt is a (small) timestep. The numerical coefficients are so-called Cash-Karp parameters [87].

In order to control the numerical error, we use this fifth order RK method in conjunction with an adaptive stepsize control. This method controls the size of increments to the wave function ψ - in rough terms, that means that more rapid changes in the wave function corresponds to smaller time steps. One of the advantages of the fifth order Runge-Kutta method set out above is the fact that another combination of the six values of k gives a fourth-order Runge-Kutta formula. This is known as an *embedded* method. The comparison of the result of the embedded fourth-order formula with that of the fifth order method can then be used as an estimate of the truncation error.

This allows us to set an upper limit for the truncation error and, if that limit is breached, to lower the size of the timestep adaptively.

Bibliography

[1] F. Mandl and G. Shaw, **Quantum Field Theory** (Wiley, revised edition, 1994).

[2] A. Einstein, *Quantentheorie des einatomigen idealen Gases. Zweite Abhandlung*, Sitzungber. Preuss. Akad. Wiss. **1925**, 3 (1925).

[3] K. Huang, **Statistical Mechanics** (Wiley, 1987).

[4] N. Bogoliubov, *On the theory of superfluidity*, J. Phys. **11**, 23 (1947).

[5] A. S. Parkins and D. F. Walls, *The physics of trapped dilute-gas Bose-Einstein condensates*, Phys. Rep. **303**, 1 (1998).

[6] F. Dalfovo, S. Giorgini, L. P. Pitaevskii, and S. Stringari, *Theory of Bose-Einstein condensation in trapped gases*, Rev. Mod. Phys. **71**, 463 (1999).

[7] K. Burnett, M. Edwards, and C. W. Clark, *The theory of Bose-Einstein condensation of dilute gases*, Phys. Today **52**, 37 (1999).

[8] A. J. Leggett, *Bose-Einstein condensation in the alkali gases: Some fundamental concepts*, Rev. Mod. Phys. **73**, 307 (2001).

[9] A. Griffin, D. W. Snoke, and S. Stringari, **Bose-Einstein Condensation** (Cambridge University Press, 1995).

[10] M. Inguscio, S. Stringari, and C. Wieman, **Bose-Einstein Condensation in atomic gases** (IOS Press, Amsterdam, 1999).

[11] C. J. Pethick and H. Smith, **Bose-Einstein Condensation in Dilute Gases** (Cambridge University Press, 2002).

[12] L. Pitaevskii and S. Stringari, **Bose-Einstein Condensation** (Clarendon Press, Oxford, 2003).

[13] M. H. Anderson, J. R. Ensher, M. R. Matthews, C. E. Wieman, and E. A. Cornell, *Observation of Bose-Einstein Condensation in a Dilute Atomic Vapor*, Science **269**, 198 (1995).

[14] F. London, *The λ-phenomenon of liquid helium and the Bose-Einstein degeneracy*, Nature **141**, 643 (1938).

[15] F. London, *On the Bose-Einstein condensation*, Phys. Rev. **54**, 947 (1938).

[16] K. B. Davis, M.-O. Mewes, M. R. Andrews, N. J. van Druten, D. S. Durfee, D. M. Kurn, and W. Ketterle, *Bose-Einstein Condensation in a Gas of Sodium Atoms*, Phys. Rev. Lett. **75**, 3969 (1995).

[17] C. C. Bradley, C. A. Sackett, J. J. Tollett, and R. G. Hulet, *Evidence of Bose-Einstein condensation in an atomic gas with attractive interactions*, Phys. Rev. Lett. **75**, 1687 (1995). *ibid.* **79**, 1170 (1997).

[18] D. G. Fried, T. C. Killian, L. Willmann, D. Landhuis, S. C. Moss, D. Kleppner, and T. J. Greytak, *Bose-Einstein condensation of atomic hydrogen*, Phys. Rev. Lett. **81**, 3811 (1998).

[19] W. D. Phillips, *Laser cooling and trapping of neutral atoms*, Rev. Mod. Phys. **70**, 721 (1998).

[20] W. Ketterle, D. S. Durfee, and D. M. Stamper-Kurn, *Making, probing and understanding Bose-Einstein condensates*, in M. Inguscio, S. Stringari, and C. E. Wieman, editors, **Proceedings of the International School of Physics - Enrico Fermi**, page 67 (IOS Press, 1999).

[21] T. Weber, J. Herbig, M. Mark, H. Nägerl, and R. Grimm, *Bose-Einstein condensation of cesium*, Science **299**, 232 (2003).

[22] M. R. Matthews, B. P. Anderson, P. C. Haljan, D. S. Hall, C. E. Wieman, and E. A. Cornell, *Vortices in a Bose-Einstein condensate*, Phys. Rev. Lett. **83**, 2498 (1999).

[23] Y. Shin, M. Saba, T. A. Pasquini, W. Ketterle, D. E. Pritchard, and A. E. Leanhardt, *Atom Interferometry with Bose-Einstein Condensates in a Double-Well Potential*, Phys. Rev. Lett. **92**, 050405 (2004).

[24] M. O. Mewes, M. R. Andrews, D. M. Kurn, D. S. Durfee, C. G. Townsend, and W. Ketterle, *Output coupler for Bose-Einstein condensed atoms*, Phys. Rev. Lett. **78**, 582 (1997).

[25] M. R. Andrews, C. G. Townsend, H. J. Miesner, D. S. Durfee, D. M. Kurn, and W. Ketterle, *Observation of interference between two Bose-Einstein condensates*, Science **275**, 637 (1997).

[26] I. Bloch, T. W. Hänsch, and T. Esslinger, *Atom Laser with a cw Output Coupler*, Phys. Rev. Lett. **82**, 3008 (1999).

[27] P. J. Martin, P. L. Gould, B. G. Oldaker, A. H. Miklich, and D. E. Pritchard, *Diffraction of atoms moving through a standing light wave*, Phys. Rev. A **36**, 2495 (1987).

[28] P. Verkerk, B. Lounis, C. Salomon, C. Cohen-Tannoudji, J. Y. Courtois, and G. Grynberg, *Dynamics and spatial order of cold cesium atoms in a periodic optical potential*, Phys. Rev. Lett. **68**, 3861 (1992).

[29] P. S. Jessen, C. Gerz, P. D. Lett, W. D. Phillips, S. L. Rolston, R. J. C. Spreeuw, and C. I. Westbrook, *Observation of Quantized Motion of Rb Atoms in an Optical Field*, Phys. Rev. Lett. **69**, 49 (1992).

[30] A. Hemmerich and T. W. Hänsch, *Two-dimensional atomic crystal bound by light*, Phys. Rev. Lett. **70**, 410 (1993).

[31] G. Raithel, G. Birkl, A. Kastberg, W. D. Phillips, and S. L. Rolston, *Cooling and Localization Dynamics in Optical Lattices*, Phys. Rev. Lett. **78**, 630 (1997).

[32] C.S. Adams, M. Sigel, and J. Mlynek, *Atom optics*, Phys. Rep. **240**, 143 (1994).

[33] F. L. Moore, J. C. Robinson, C. Bharucha, P. E. Williams, and M. G. Raizen, *Observation of Dynamical Localization in Atomic Momentum Transfer: A New Testing Ground for Quantum Chaos*, Phys. Rev. Lett. **73**, 2974 (1994).

[34] S. Backhaus, S. V. Pereverzev, A. Loshak, J. C. Davis, and R. E. Packard, *Direct Measurement of the Current-Phase Relation of a Superfluid ^{3}He-B Weak Link*, Science **278**, 1435 (1997).

[35] A. Smerzi, S. Fantoni, S. Giovanazzi, and S. R. Shenoy, *Quantum Coherent Atomic Tunneling between Two Trapped Bose-Einstein Condensates*, Phys. Rev. Lett. **79**, 4950 (1997).

[36] I. Zapata, F. Sols, and A. J. Leggett, *Josephson effect between trapped Bose-Einstein condensates*, Phys. Rev. A **57**, R28 (1998).

[37] B. P. Anderson and M. A. Kasevich, *Macroscopic Quantum Interference from Atomic Tunnel Arrays*, Science **282**, 1686 (1998).

[38] I. Bloch, *Quantum gases in optical lattices*, Physics World **17**, 7 (2004).

[39] D. Jaksch, C. Bruder, J. I. Cirac, C. W. Gardiner, and P. Zoller, *Cold Bosonic Atoms in Optical Lattices*, Phys. Rev. Lett. **81**, 3108 (1998).

[40] M. Greiner, O. Mandel, T. Esslinger, T. W. Hänsch, and I. Bloch, *Quantum phase transition from a superfluid to a Mott insulator in a gas of ultracold atoms*, Nature **415**, 39 (2002).

[41] T. Stöfele, H. Moritz, C. Schori, M. Köhl, and T. Esslinger, *Transition from a Strongly Interacting 1D Superfluid to a Mott Insulator*, Phys. Rev. Lett. **92**, 130403 (2004).

[42] C. N. Cohen-Tannoudji, **Atom-Photon Interactions** (Wiley - Interscience, 1992).

[43] C. N. Cohen-Tannoudji, *Manipulating atoms with photons*, Rev. Mod. Phys. **70**, 707 (1998).

[44] R. Graham, D.F. Walls, and P. Zoller, *Emission from atoms in linear superpositions of center-of-mass packets*, Phys. Rev. A **45**, 5018 (1992).

[45] R. Loudon, **The Quantum Theory of Light** (Oxford University Press, third edition, 2000).

[46] H. Wallis, *Quantum theory of atomic motion in laser light*, Phys. Rep. **255**, 203 (1995).

[47] A. R. Kolovsky and H. J. Korsch, *Bloch oscillations of cold atoms in optical lattices* (2004), cond-mat/0403205.

[48] S. M. Barnett and P. M. Radmore, **Methods in Theoretical Quantum Optics** (Clarendon Press, Oxford, 1997).

[49] D. A. Steck. *Atomic Motion in a Standing Wave of Far-Detuned Light.* http://www.ph.utexas.edu/ quantopt/resources.html.

[50] E. T. Whittaker and G. N. Watson, **A course of modern analysis** (Cambridge University Press, fourth edition, 1927).

[51] J. C. Slater, *A Soluble Problem in Energy Bands*, Phys. Rev. **87**, 807 (1952).

[52] M. L. Chiofalo, M. Polini, and M. P. Tosi, *Collective excitations of a periodic Bose condensate in the Wannier representation*, Eur. Phys. J. D **11**, 371 (2000).

[53] M. P. A. Fisher, B. P. Weichman, G. Grinstein, and D. S. Fisher, *Boson localization and the superfluid-insulator transition*, Phys. Rev. B **40**, 546 (1989).

[54] S. Sachdev, **Quantum Phase Transitions** (Cambridge University Press, 1999).

[55] P. B. Blakie and C. W. Clark, *Wannier states and Bose-Hubbard parameters for 2D optical lattices*, J. Phys. B: At. Mol. Opt. Phys. **37**, 1391 (2004).

[56] W. Nolting, **Grundkurs theoretische Physik: Viel-Teilchen-Theorie** (Springer, fifth edition, 2002).

[57] K. Burnett, *Ultracold interactions and mean-field theory of Bose-Einstein condensates*, in M. Inguscio, S. Stringari, and C. E. Wieman, editors, **Proceedings of the International School of Physics - Enrico Fermi**, page 265 (IOS Press, 1999).

[58] J. Dalibard, *Collisional dynamics of ultra-cold atomic gases*, in M. Inguscio, S. Stringari, and C. E. Wieman, editors, **Proceedings of the International School of Physics - Enrico Fermi**, page 321 (IOS Press, 1999).

[59] O. Morsch, J. H. Müller, M. Cristiani, D. Ciampini, and E. Arimondo, *Bloch oscillations and mean-field effects of Bose-Einstein condensates in 1D optical lattices*, Phys. Rev. Lett. **87**, 140402 (2001).

[60] S. R. Wilkinson, C. F. Bharucha, M. C. Fischer, K. W. Madison, P. R. Morrow, Q. Niu, and M. G. Raizen, *Experimental evidence for non-exponential decay in quantum tunneling*, Nature **387**, 575 (1997).

[61] C. Zener, *Non-adiabatic crossing of energy levels*, Proc. Roy. Soc. London **A 137**, 696 (1932).

[62] Q. Niu and M.G. Raizen, *How Landau-Zener Tunneling Takes Time*, Phys. Rev. Lett. **80**, 3491 (1998).

[63] N. Elstner and H. Monien, *Dynamics and thermodynamics of the Bose-Hubbard model*, Phys. Rev. B **59**, 184 (1999).

[64] W. Zwerger, *Mott-Hubbard transition of cold atoms in optical lattices*, Journal of Optics B **5**, S9 (2003).

[65] G. G. Batrouni and R. T. Scalettar, *World-line quantum Monte Carlo algorithm for a one-dimensional Bose model*, Phys. Rev. B **46**, 9051 (1992).

[66] K. G. Singh and D. S. Rokhsar, *Real-space renormalization study of disordered interacting bosons*, Phys. Rev. B **46**, 3002 (1992).

[67] T. D. Kühner and H. Monien, *Phases of the one-dimensional Bose-Hubbard model*, Phys. Rev. B **58**, R14741 (1998).

[68] S. Rapsch, U. Schollwöck, and W. Zwerger, *Density matrix renormalization group for disordered bosons in one dimension*, Europhys. Lett. **46**, 559 (1999).

[69] K. Sheshadri, H. R. Krishnamurthy, R. Pandit, and R. V. Ramakrishnan, *Superfluid and insulating phases in an interacting-boson model: Mean-field theory and the RPA*, Europhys. Lett. **22**, 257–263 (1993).

[70] J. K. Freericks and H. Monien, *Strong-coupling expansions for the pure and disordered Bose-Hubbard model*, Phys. Rev. B **53**, 2691 (1996).

[71] D. van Oosten, P. van der Straten, and H. T. C. Stoof, *Quantum phases in an optical lattice*, Phys. Rev. A **63**, 053601 (2001).

[72] G. G. Batrouni, V. Rousseau, R. T. Scalettar, M. Rigol, A. Muramatsu, P. J. H. Denteneer, and M. Troyer, *Mott Domains of Bosons Confined on Optical Lattices*, Phys. Rev. Lett. **89**, 117203 (2002).

[73] V. A. Kashurnikov, N. V. Prokof'ev, and B. V. Svistunov, *Revealing the superfluid-Mott-insulator transition in an optical lattice*, Phys. Rev. A **66**, 031601(R) (2002).

[74] E. L. Pollock and D. M. Ceperley, *Path-integral computation of superfluid densities*, Phys. Rev. B **36**, 8343 (1987).

[75] N. V. Prokof'ev and B. V. Svistunov, *Two definitions of superfluid density*, Phys. Rev. B **61**, 11282 (2000).

[76] R. Roth and K. Burnett, *Superfluidity and interference pattern of ultracold bosons in optical lattices*, Phys. Rev. A **67**, 031602(R) (2003).

[77] A. J. Leggett, *Superfluidity*, Rev. Mod. Phys. **71**, S318 (1999).

[78] B. Damski, *Atomic Bose and Anderson Glasses in Optical Lattices*, Phys. Rev. Lett. **91**, 080403 (2003).

[79] E. Altman, E. Demler, and M. D. Lukin, *Probing many-body states of ultracold atoms via noise correlations*, Phys. Rev. A **70**, 013603 (2004).

[80] J. Javanainen and S. M. Yoo, *Quantum phase of a Bose-Einstein condensate with an arbitrary number of atoms*, Phys. Rev. Lett. **76**, 161 (1996).

[81] O. M. Maragó, S. A. Hopkins, J. Arlt, E. Hodby, G. Heckenblaikner, and C. J. Foot, *Observation of the scissors mode and evidence for superfluidity of a trapped Bose-Einstein condensed gas*, Phys. Rev. Lett. **84**, 2056 (2000).

[82] K. Damle, T. Senthil, S. N. Majumdar, and S. Sachdev, *Phase transition of a Bose gas in a harmonic potential*, Europhys. Lett. **36**, 7 (1996).

[83] K. Braun-Munzinger, J. A. Dunningham, and K. Burnett, *Excitations of Bose-Einstein condensates in optical lattices*, Phys. Rev. A **69**, 053613 (2004).

[84] J. A. Dunningham, K. Burnett, and S. M. Barnett, *Interferometry below the standard quantum limit with Bose-Einstein condensates*, Phys. Rev. Lett. **89**, 150401 (2002).

[85] C. Orzel, A. K. Tuchman, M. L. Fenselau, M. Yasuda, and M. A. Kasevich, *Squeezed states in a Bose-Einstein condensate*, Science **291**, 2386 (2001).

[86] M. Greiner, O. Mandel, T. W. Hänsch, and I. Bloch, *Collapse and revival of the matter wave field of a Bose-Einstein condensate*, Nature **419**, 51 (2002).

[87] W. Press, S. Teukolsky, W. Vetterling, and B. Flannery. **Numerical Recipes in C++, The Art of Scientific Computing**, chapter 16. Cambridge University Press, 2002.

[88] J. A. Dunningham, M. J. Collett, and D. F. Walls, *Quantum state of a trapped Bose-Einstein condensate*, Phys. Lett. A **245**, 49–54 (1998).

[89] E. M. Wright, D. F. Walls, and J. C. Garrison, *Collapses and revivals of Bose-Einstein condensates formed in small atomic samples*, Phys. Rev. Lett. **77**, 2158 (1996).

[90] E. M. Wright, T. Wong, M. J. Collett, S. M. Tan, and D. F. Walls, *Collapses and revivals in the interference between two Bose-Einstein condensates formed in small atomic samples*, Phys. Rev. A **56**, 591 (1997).

[91] A. Imamoḡlu, M. Lewenstein, and L. You, *Inhibition of Coherence in Trapped Bose-Einstein Condensates*, Phys. Rev. Lett. **78**, 2511 (1997).

[92] Y. Castin and J. Dalibard, *Relative phase of two Bose-Einstein condensates*, Phys. Rev. A **55**, 4330 (1997).

[93] M. W. Jack and M. Yamashita, *Signatures of the quantum fluctuations of cold atoms in an optical lattice in the three-body loss rate*, Phys. Rev. A **67**, 033605 (2003).

[94] A. R. Kolovsky, *Bloch oscillations in the Mott-insulator regime*, Phys. Rev. A **70**, 015604 (2003), cond-mat/0312024.

[95] D. C. Roberts and K. Burnett, *Probing States in the Mott Insulator Regime in the Case of Coherent Bosons Trapped in an Optical Lattice*, Phys. Rev. Lett. **90**, 150401 (2003).

[96] W. H. Bragg, *The reflection of X-rays by crystals*, Proc. Cambridge PHil. Soc. **17**, 43 (1912).

[97] E. Fermi and L. Marshall, *Interference Phenomena of Slow Neutrons*, Phys. Rev. **71**, 666 (1947).

[98] H. Rauch, W. Treimer, and U. Bonse, *Test of a Single Crystal Neutron Interferometer*, Phys. Lett. **47A**, 369 (1974).

[99] P. Martin, B. G. Oldaker, A. H. Miklisch, and D. E. Pritchard, *Bragg scattering of atoms from a standing light wave*, Phys. Rev. Lett. **60**, 515 (1988).

[100] D. M. Giltner, R. W. McGowan, and S. A. Lee, *Atom Interferometer Based on Bragg Scattering from Standing Light Waves*, Phys. Rev. Lett. **75**, 2638 (1995).

[101] M. Kozuma, L. Deng, E. W. Hagley, J. Wen, R. Lutwak, K. Helmerson, S. L. Rolston, and W. D. Phillips, *Coherent splitting of Bose-Einstein condensed atoms with optically induced Bragg diffraction*, Phys. Rev. Lett. **82**, 871 (1999).

[102] P. R. Berman and B. Bian, *Pump-probe spectroscopy approach to Bragg scattering*, Phys. Rev. A **55**, 4382 (1997).

[103] J. Stenger, S. Inouye, A. P. Chikkatur, D. M. Stamper-Kurn, D. E. Pritchard, and W. Ketterle, *Bragg Spectroscopy of a Bose-Einstein Condensate*, Phys. Rev. Lett. **82**, 4569 (1999).

[104] G. Baym and C. J. Pethick, *Ground-State Properties of Magnetically Trapped Bose-Condensed Rubidium Gas*, Phys. Rev. Lett. **76**, 6 (1996).

[105] F. Kh. Abdullaev, B. B. Baizakov, S. A. Darmanyan, V. V. Konotop, and M. Salerno, *Nonlinear excitations in arrays of Bose-Einstein condensates*, Phys. Rev. A. **64**, 043606 (2001).

[106] M. Krämer, L. Pitaevskii, and S. Stringari, *Macroscopic dynamics of a trapped Bose-Einstein condensate in the presence of 1D and 2D optical lattices*, Phys. Rev. Lett. **88**, 180404 (2002).

[107] M. Machholm, C. J. Pethick, and H. Smith, *Band structure, elementary excitations, and stability of a Bose-Einstein condensate in a periodic potential*, Phys. Rev. A **67**, 053613 (2003).

[108] P. Massignan and M. Modugno, *One-dimensional model for the dynamics and expansion of elongated Bose-Einstein condensates*, Phys. Rev. A **67**, 023614 (2003).

[109] J. P. Martikainen and H. T. C. Stoof, *Excitations fo a Bose-Einstein condensate in a one-dimensional optical lattice*, Phys. Rev. A **68**, 013610 (2003).

[110] A. Smerzi and A. Trombettoni, *Discrete nonlinear dynamics of weakly coupled Bose-Einstein condensates*, Chaos **13**, 766 (2003).

[111] J. Plata, *Loading of a Bose-Einstein condensate into an optical lattice: The excitation of collective modes*, Phys. Rev. A **69**, 033604 (2004).

[112] S. Kunze, S. Dürr, and G. Rempe, *Bragg scattering of slow atoms from a standing light wave*, Europhys. Lett. **34**, 343 (1996).

[113] J. J. García-Ripoll, J. I. Cirac, P. Zoller, C. Kollath, U. Schollwöck, and J. von Delft, *Variational ansatz for the superfluid Mott-insulator transition in optical lattices*, Optics Express **12**, 42 (2004).

[114] C. F. Hart and D. Emin, *Time evolution of a Bloch electron in a constant electric field*, Phys. Rev. B **37**, 6100 (1988).

[115] A. M. Bouchard and M. Luban, *Bloch oscillations and other dynamical phenomena of electrons in semiconductor superlattices*, Phys. Rev. B **52**, 5105 (1995).

[116] M. Glück, A. R. Kolovsky, and H.J. Korsch, *Wannier-Stark resonances in optical and semiconductor superlattices*, Phys. Rep. **366**, 103–182 (2002).

[117] J. B. Krieger and G. J. Iagrate, *Time evolution of Bloch electrons in a homogenous electric field*, Phys. Rev. B **33**, 5494 (1986).

[118] G. Nenciu, *Dynamics of band electrons in electric and magnetic fields: rigorous justification of the effective Hamiltonians*, Rev. Mod. Phys. **63**, 91 (1991).

[119] G. H. Wannier, *Wave Functions and Effective Hamiltonian for Bloch Electrons in an Electric Field*, Phys. Rev. **117**, 432 (1960).

[120] Q. Niu, X. G. Zhao, G. A. Georgakis, and M. G. Raizen, *Atomic Landau-Zener Tunneling and Wannier-Stark Ladders in Optical Potentials*, Phys. Rev. Lett **76**, 4504 (1996).

[121] M. Glück, F. Keck, A. R. Kolovsky, and H. J. Korsch, *Wannier-Stark States of a Quantum Particle in 2D Lattices*, Phys. Rev. Lett. **86**, 3116 (2001).

[122] A. Buchleitner and A. R. Kolovsky, *Interaction-Induced Decoherence of Atomic Bloch Oscillations*, Phys. Rev. Lett. **91**, 253002 (2003).

[123] K. P. Marzlin and J. Audretsch, *Atom optical interpretation of Bloch oscillations*, Europhys. Lett. **36**, 43 (1996).

[124] A. R. Kolovsky, *New Bloch Period for Interacting Cold Atoms in 1D Optical Lattices*, Phys. Rev. Lett. **90**, 213002 (2003).

[125] E. Altman and A. Auerbach, *Oscillating Superfluidity of Bosons in Optical Lattices*, Phys. Rev. Lett. **89**, 250404 (2002).

[126] A. Polkovnikov, S. Sachdev, and S.M. Girvin, *Nonequilibrium Gross-Pitaevskii dynamics of boson lattice models*, Phys. Rev. A **66**, 053607 (2002).

[127] C. Fort, F. S. Cataliotti, L. Fallani, F. Ferlaino, P. Maddaloni, and M. Inguscio, *Collective Excitations of a Trapped Bose-Einstein Condensate in the Presence of a 1D Optical Lattice*, Phys. Rev. Lett. **90**, 140405 (2003).

[128] J. Feldmann, K. Leo, J. Shah, D. A. B. Miller, and J. E. Cunningham, *Optical investigation of Bloch oscillations in a semiconductor superlattice*, Phys. Rev. B **46**, 7252 (1992).

[129] S. R. Wilkinson, C. F. Bharucha, and K. W. Madison, *Observation of Atomic Wannier-Stark Ladders in an Accelerating Optical Potential*, Phys. Rev. Lett. **76**, 4512 (1996).

[130] M. B. Dahan, E. Peik, J. Reichel, Y. Castin, and C. Salomon, *Bloch Oscillations of Atoms in an Optical Potential*, Phys. Rev. Lett **76**, 4508 (1996).

[131] K. W. Madison, M. C. Fischer, and M. G. Raizen, *Observation of the Wannier-Stark fan and the fractional ladder in an accelerating optical lattice*, Phys. Rev. A **60**, R1767 (1999).

[132] M. Raizen, C. Salomon, and Q. Niu, *New Light on Quantum Transport*, Phys. Today **50**, 30 (1997).

[133] F. Bloch, *Über die Quantenmechanik der Electronen in Kristallgittern*, Z. Phys. **52**, 555 (1928).

[134] A. J. Daley, C. Kollath, U. Schollwöck, and G. Vidal, *Time-dependent density-matrix renormalization-group using adaptive effective Hilbert spaces*, J. Stat. Mech.: Theor. Exp page P04005 (2004).

[135] C. A. Regal and D. S. Jin, *Measurement of Positive and Negative Scattering Lengths in a Fermi Gas of Atoms*, Phys. Rev. Lett. **90**, 230404 (2003).